GREEN SYNTHESIS AND CHARACTERIZATION OF COPPER OXIDE (CuO) NANOPARTICLES USING BARKS OF SOURSOP (*Annona muricata*)

By

YURIKO LIM JING EN

A project report submitted to the Department of Chemical Science

Faculty of Science

Universiti Tunku Abdul Rahman

In partial fulfillment of the requirements for the degree of

Bachelor of Science (Honours) Chemistry

SEPTEMBER 2025

ABSTRACT

GREEN SYNTHESIS AND CHARACTERIZATION OF COPPER OXIDE (CuO) NANOPARTICLES USING BARKS OF SOURSOP (*Annona muricata*)

YURIKO LIM JING EN

This study presents the green synthesis of copper oxide nanoparticles (CuO NPs) utilizing the bark extract of *Annona muricata* as a natural reducing and stabilizing agent, with copper(II) nitrate trihydrate serving as precursor salt and varying calcination temperatures (300, 400, and 500°C). The effect of different calcination temperatures on the structural, morphological, and optical properties of the CuO NPs (CuO-300, CuO-400, and CuO-500 NPs) was characterized using Ultraviolet-Visible Spectroscopy (UV-Vis), Fourier Transform-Infrared Spectroscopy (FT-IR), Field Emission Scanning Electron Microscopy (FESEM), Energy Dispersive X-ray Spectroscopy (EDX), and X-ray Diffraction (XRD). This project successfully synthesized CuO NPs through a green synthesis method by varying calcination temperatures. The UV-Vis spectra showed a maximum absorption peak at 368 nm for CuO-300 and CuO-500 NPs and 370

nm for CuO-400 NPs, corresponding to a band gap energy of 3.37 eV for CuO-300 and CuO-500 NPs, and 3.35 eV for CuO-400 NPs. The FT-IR spectra revealed prominent absorption bands at 552, 568, and 545 cm^{-1} for CuO-300, CuO-400, and CuO-500 NPs, respectively. In addition, the synthesized CuO-300, CuO-400, and CuO-500 NPs exhibited spherical morphology with differences in particle sizes ranging from 28.1 - 36.4 nm for CuO-300 NPs, 27.7 - 33.5 nm for CuO-400 NPs, and 27.3 - 34.5 nm for CuO-500 NPs. The EDX analysis showed only copper and oxygen elements present in the synthesized CuO NPs without any other impurity peaks. Lastly, all the synthesized CuO NPs exhibited a monoclinic structure, and the average crystallite size for CuO-300, CuO-400, and CuO-500 NPs was found to be 27.09, 25.22, and 25.14 nm, respectively.

ABSTRAK

SINTESIS HIJAU DAN PENCIRIAN NANOPARTIKEL KUPRUM OKSIDA (CuO) MENGGUNAKAN BATANG DURIAN BELANDA (*Annona muricata*)

Kajian ini membentangkan penyintesisan hijau nanopartikel kuprum oksida (CuO NPs) dengan menggunakan ekstrak batang *A. muricata* sebagai agen pengurangan dan penstabil semula jadi, dengan kuprum(II) nitrat trihidrat sebagai garam precursor dan suhu kalsinasi yang berbeza (300, 400, and 500°C). Kesan suhu kalsinasi yang berbeza terhadap sifat struktur, morfologi, dan optic CuO NPs (CuO-300, CuO-400, CuO-500 NPs) dikarakterisasi menggunakan Spektroskopi Ultralembayung-nampak (UV-Vis), Spektroskopi Inframerah Transformasi Fourier (FT-IR), Mikroskop Imbasan Elektron Emisi Medan (FESEM), Spektroskopi Tenaga Dispersif X-Ray (EDX) dan Belauan Sinar-X (XRD). Projek ini berjaya menghasilkan CuO NPs melalui kaedah sintesis hijau dengan pelbagai suhu kalsinasi. Spektrum UV-Vis menunjukkan puncak penyerap maksimum pada 368 nm untuk CuO-300 dan CuO-500 NPs, dan 370 nm untuk CuO-400 NPs, yang bersamaan dengan tenaga jurang jalur 3.37 eV bagi CuO-300 dan CuO-500 NPs, serta 3.35 eV bagi CuO-400 NPs. Spektrum FT-IR pula memperlihatkan jalur penyerapan ketara pada 552, 568, dan 545 cm^{-1} bagi CuO-300, CuO-400, dan CuO-500 NPs masing-masing. Selain itu, nanopartikel CuO-300, CuO-400, dan CuO-500 yang disintesis menunjukkan

morfologi sfera dengan saiz zarah berbeza, iaitu dari 28.1 - 36.4 nm bagi CuO-300 NPs, 27.7 - 33.5 nm bagi CuO-400 NPs, dan 27.3 - 34.5 nm bagi CuO-500 NPs. Analisis EDX menunjukkan kehadiran unsur kuprum dan oksigen sahaja dalam CuO NPs yang disintesis tanpa sebarang puncak cemar lain. Akhir sekali, semua CuO NPs yang disintesis menunjukkan struktur monokilinik dengan saiz kristalit purata masing-masing sebanyak 27.09, 25.22, dan 25.14 nm untuk CuO-300, CuO-400, dan CuO-500 NPs.

ACKNOWLEDGEMENTS

First and foremost, I would like to extend my deepest gratitude to my project supervisor, Dr. Yip Foo Win, for his unwavering support, expert guidance, and invaluable advice throughout the entire duration of my final year project. His insightful feedback and encouragement have been instrumental in shaping the direction of this research and ensuring its successful completion.

I am sincerely thankful to Universiti Tunku Abdul Rahman (UTAR) for providing access to excellent laboratory facilities and reliable instruments, which were essential components for conducting the experiments and analyses involved in this project. My deepest appreciation is also reserved for all lecturers at the Faculty of Science, whose knowledge and motivation have enriched my learning experience and equipped me with the skills necessary to undertake this project. Their dedication and support have played a significant role in my academic development. Sincere thanks are extended to the laboratory staff, especially Mr Seou Chi Kien, for their patient assistance and expert advice in handling the sophisticated equipment used during this work.

Lastly, I am profoundly grateful to my family and friends for their endless encouragement, understanding, and moral support throughout my academic journey. Their love and belief in me were constant sources of strength and motivation, enabling me to overcome challenges and achieve my goals.

DECLARATION

I hereby declare that this final year project report is based on my original work except for quotations and citations, which have been duly acknowledged. I also declare that it has not been previously or concurrently submitted for any other degree at UTAR or other institutions.

YURIKO LIM JING EN

APPROVAL SHEET

This final year project report entitled **"GREEN SYNTHESIS AND CHARACTERIZATION OF COPPER OXIDE (CuO) NANOPARTICLES USING BARKS OF SOURSOP (*Annona muricata*)"** was prepared by YURIKO LIM JING EN and submitted as partial fulfillment of the requirements for the degree of Bachelor of Science (Hons) Chemistry at Universiti Tunku Abdul Rahman.

Approved by:

____YIP FOO WIN_____

(Asst. Prof. Dr. Yip Foo Win) Date: 23/9/2025

Supervisor

Department of Chemical Science

Faculty of Science

Universiti Tunku Abdul Rahman

FACULTY OF SCIENCE

UNIVERSITI TUNKU ABDUL RAHMAN

Date: 23 SEPTEMBER 2025

PERMISSION SHEET

It is hereby certified that YURIKO LIM JING EN (ID No: 21ADB05970) has completed this final year project thesis entitled "GREEN SYNTHESIS AND CHARACTERIZATION OF COPPER OXIDE (CuO) NANOPARTICLES USING BARKS OF SOURSOP (*Annona muricata*)" under the supervision of ASST. PROF. DR. YIP FOO WIN from the Department of Chemical Science, Faculty of Science.

I hereby give permission to the University to upload the softcopy of my final year project thesis in PDF format into the UTAR Institutional Repository, which may be made accessible to the UTAR community and public.

Yours truly,

YURIKO LIM JING EN

TABLE OF CONTENTS

LIST OF TABLES

LIST OF FIGURES

LIST OF ABBREVIATIONS

A. muricata	*Annona muricata*
A. sativum	*Allium sativum*
Ag	Silver
Al_2O_3	Alumina
AR	Analytical research
Au	Gold
c	Speed of light (3.00×10^8 ms^{-1})
C=O	Carbonyl group
C_{60}	60 carbon atoms
CAS	Chemical Abstracts Service
CBNPs	Carbon black nanoparticles
cm	Centimeter
cm^{-1}	Reciprocal centimeter
CO_2	Carbon dioxide
CQDs	Carbon quantum dots
Cu	Copper
$Cu(NO_3)_2{\cdot}3H_2O$	Copper(II) nitrate trihydrate
$Cu(NO_3)_2$	Copper(II) nitrate
$Cu(NO_3)_2{\cdot}6H_2O$	Copper(II) nitrate hexahydrate
$CuCl_2$	Copper(II) chloride
$Cu(CH_3COO)_2$	Copper(II) acetate
CuO	Copper oxide
D	Crystallite size in diameter

EDX	Energy Dispersive X-ray
E_g	Band gap energy
eV	Electron volt
Fe	Iron
Fe_2O_3	Iron(III) oxide
Fe_3O_4	Magnetite
FESEM	Field Emission Scanning Electron
FT-IR	Fourier Transform Infrared
FWHM	Full width half maximum of the diffraction peak in radian 2θ
g	Gram
h	Planck's constant
H_2O	Water molecule
ICDD	International Centre of Diffraction Standard
J	Joule
k	Scherrer's constant (0.9)
KBr	Potassium bromide
kg	Kilogram
M. calabura	*Muntingia calabura*
mg	Milligram
MH	Magnetic hyperthermia
mL	Millilitre
mm^2	Square millimeter
MRI	Magnetic resonance imaging

n	Non-bonding orbital
nm	Nanometer
NPs	Nanoparticles
O	Oxygen atom
O_2	Oxygen molecule
-OH	Hydroxyl group
P. pyrifolia	*Pyrus pyrifolia*
Rpm	Revolutions per minute
SiO_2	Silica
STM	Scanning tunnelling microscope
TEM	Transmission Electron Microscopy
TiO_2	Titanium oxide
UV-Vis	Ultraviolet-Visible
XRD	X-ray Diffraction
ZnO	Zinc oxide
ZrO_2	Zirconium dioxide
λ_{max}	Maximum absorption wavelength
μ	Micro
π	Pi
%	Percent
°	Degree
°C	Degree Celsius

CHAPTER 1

INTRODUCTION

1.1 Background of study

Nanotechnology is an interdisciplinary field dedicated to the study, manipulation, engineering of materials and devices at the nanoscale, which ranges from 1 - 100 nanometers (Tongi, 2023). At this nanoscale, materials display distinctive and significantly enhanced properties compared to those of their bulk forms. These distinctive characteristics result from an increased total surface area-to-volume ratio and quantum mechanical effects that predominate at the nanoscale, enabling diverse applications in medicine, electronics, energy, and environmental science (Piyush, 2023).

The origins of this technology can be dated back to 1959 when Richard Feynman, an American physicist often recognized as the pioneer of modern nanotechnology, delivered his visionary lecture titled "*There's Plenty of Room at the Bottom*" (Bayda et al., 2019). In this presentation, he proposed the concept of manipulating matter at the scale of individual atoms and molecules (Bayda et al., 2019). It was introduced later in 1974 by a Japanese scientist, Norio Taniguchi, to describe the process of precision machining at the atomic scale (Bayda et al., 2019).

During the 1980s and 1990s, the field of nanotechnology experienced notable growth, particularly after the invention of the scanning tunnelling microscope (STM) by Gerd Binnig and Heinrich Rohrer in 1981 (Bayda et al., 2019). This groundbreaking tool made it possible to observe and manipulate atomic-scale surfaces, a contribution that earned them a Nobel Prize in Physics in 1986 (Bayda et al., 2019).

Today, nanotechnology continues to evolve rapidly, impacting consumer products, healthcare, electronics, and environmental technologies. Its interdisciplinary nature combines physics, chemistry, biology, and engineering to harness the unique phenomena at the nanoscale.

1.2 Nanoparticles (NPs)

Nanoparticles (NPs) are tiny particles with sizes typically ranging from 1 - 100 nanometers (nm), representing the fundamental building blocks of nanotechnology. These particles can be spherical, cubic, rod-like, or exhibit other morphologies, with their size and shape strongly influenced by synthesis conditions. NPs can occur naturally or be synthesized artificially and are characterized by their small size and high surface energy. Their applications range from drug delivery and medical imaging to catalysis and environmental remediation (Joudeh and Linke, 2022). The versatility of NPs arises from their diverse compositions, shapes, and sizes, which can be tailored to meet specific purposes.

NPs are broadly classified into three main categories, as illustrated in Figure 1.1, and the details for each type of NPs according to their composition and origin are shown in Table 1.1.

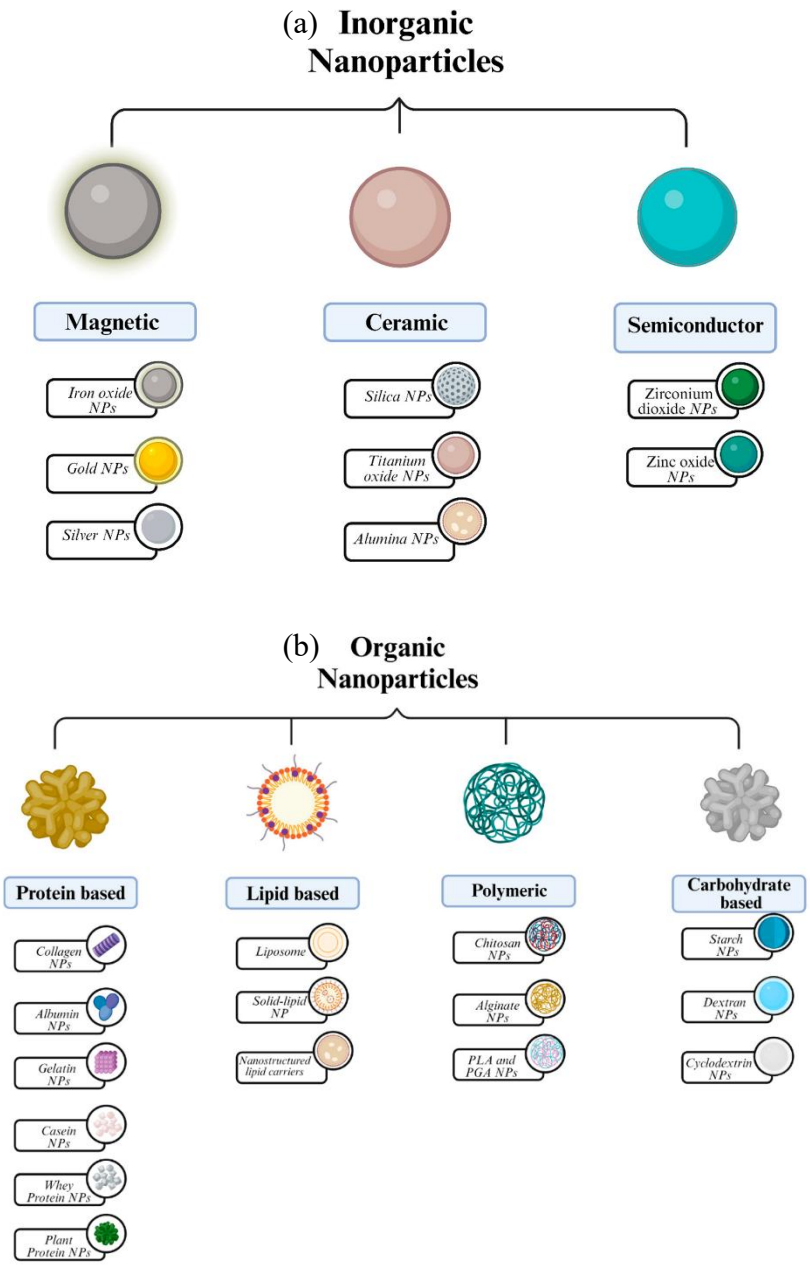

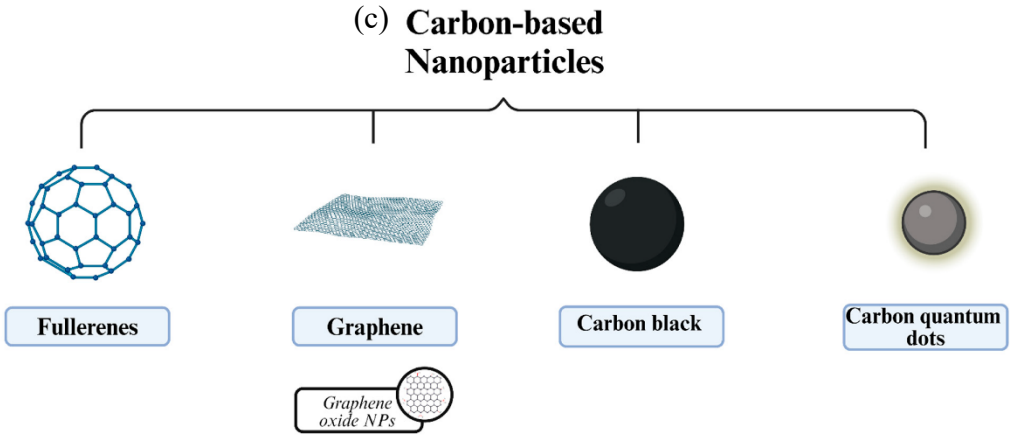

Figure 1.1: Categories of NPs, which are (a) inorganic, (b) organic, and (c) carbon-based NPs (Eker et al., 2024).

Table 1.1: Classification and applications of NPs based on their composition and origin (Teleanu et al., 2018; Kumari and Sarkar, 2021; Eker et al., 2024).

Types of NPs	Description
Organic	Composition: • Lipids, proteins, polymers, and carbohydrate-based. Key properties: • Biodegradable, biocompatible, non-toxic, and sensitive to thermal and electromagnetic radiation. Examples: • Liposomes, dendrimers, micelles, and ferritin. Applications:

	• Drug delivery system, gene therapy, cosmetics, food packaging, and biomedical imaging.
Inorganic	• Divided into three types, which are magnetic, ceramic, and semiconductor NPs. 1. <u>Magnetic</u> Composition: • Metal oxides with magnetic behavior. Key properties: • Superparamagnetic, ferromagnetic, and magnetic responsiveness. Examples: • Iron oxide (Fe_2O_3, Fe_3O_4) Applications: • Magnetic resonance imaging (MRI), drug delivery system, magnetic hyperthermia (MH) treatment, gene delivery, and tissue engineering (Ashish Avasthi et al., 2020; Eker et al., 2024). 2. <u>Ceramic</u> Composition: • Inorganic non-metallic and metallic solids. Key properties:

	• Hardness, chemical inertness, electrical insulators, and high thermal stability. Examples: • Silica (SiO_2), titanium oxide (TiO_2), zirconium dioxide (ZrO_2), and alumina (Al_2O_3). Applications: • Endodontic filling materials, biomedicine in controlled drug release, and bone tissue engineering (Singh et al., 2014).
Inorganic	3. <u>Semiconductor</u> Composition: • Solid materials possess a crystalline structure. Key properties: • High chemical stability, photostability, conductivity, mechanical stability, and high binding energy. Examples: • Zirconium dioxide (ZrO_2) and zinc oxide (ZnO) Applications: • Catalysis, sensors, optical coatings, solar cells, and dentistry.

Carbon-based	• Can be divided into five classes, which are graphene, fullerenes, carbon quantum dots (CQDs), and carbon black nanoparticles (CBNPs). 1. <u>Graphene</u> Composition: • Two-dimensional carbon atoms. Key properties: • High thermal conductivity, hydrophobicity, and high oxygen-containing functional groups. Examples: • Graphene oxide Applications: • Photothermal therapy (Yang et al., 2013). 2. <u>Fullerenes</u> Composition: • Hollow clusters of sp_2-hybridized carbon atoms linked together through covalent bonds. Key properties: • Consists of unique chemical reactivity, electron affinity, and UV-based damage protection. Examples:

Carbon-based	• Fullerene with 60 carbon atoms (C_{60}) Applications: • Nanosensors, antioxidants, solar cells, dermatological applications, and therapeutics in nanomedicine. 3. Carbon quantum dots (CQDs) Composition: • Zero-dimensional, quasi-spherical NPs with size smaller than 10 nm. Key properties: • Environmentally friendly, low-toxicity, cost-effective, consist of antibacterial activity and strong photoluminescence. Examples: • Functional groups such as amine, carboxyl, carbonyl, and hydroxyl. Applications: • Fluorescence imaging, bioimaging, and biosensors. 4. Carbon black NPs (CBNPs) Composition: • Amorphous carbon. Key properties:

	• High surface area-to-volume ratio, unique electrochemical properties, and mechanical reinforcement. Examples: • Palladium NPs
Carbon-based	Applications: • Electrochemical sensors, lithium and sodium batteries, reinforcing fillers in the rubber industry, pigments in the plastic industry, and an immune sensor for cancer cells.

1.2.1 Methods to synthesis nanoparticles (NPs)

NPs synthesis methods are broadly divided into two main groups, which are top-down and bottom-up approaches (Kumari and Sarkar, 2021). The schematic representation of the two approaches is illustrated in Figure 1.2. Each approach can be further divided into different methods as illustrated in Figure 1.3, offering various techniques for controlling particle size, shape, and properties. Each offering distinct advantages and suited for different materials and applications.

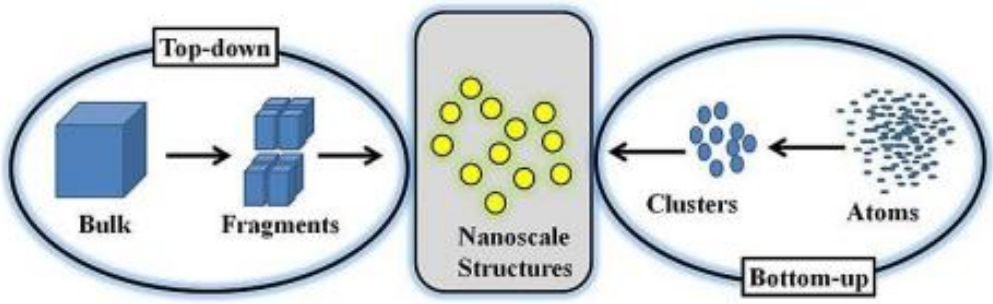

Figure 1.2: Schematic representation of the Top-down and the Bottom-up approach (Kumari and Sarkar, 2021).

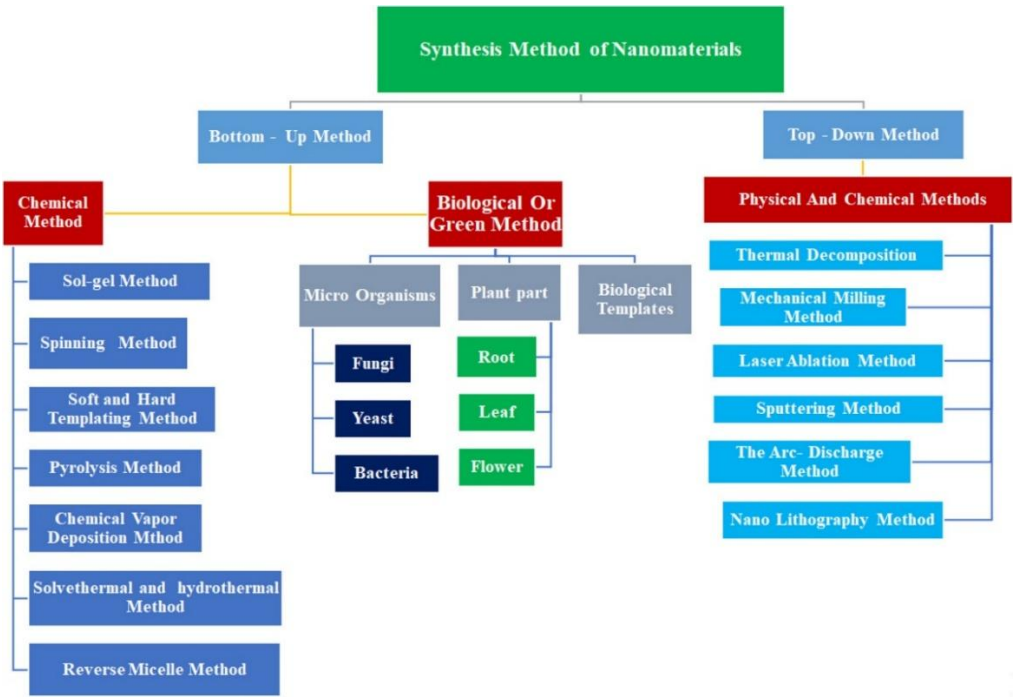

Figure 1.3: Different NPs synthesis methods (Mekuye and Abera, 2023).

The top-down approach, also known as the destructive method, entails breaking down bulk materials into nanoscale particles (Adil et al., 2024). This approach includes three main methods. First, mechanical methods such as ball-milling and

homogenization physically grind bulk materials into NPs; second, lithographic techniques like electron beam lithography, which use patterning methods to create nanoscale features; third, physical methods such as laser ablation and spark discharge vaporize materials, which then condense into NPs (Mekuye and Abera, 2023). These top-down methods are generally used to produce a large number of NPs but may introduce defects or irregularities in particle size and shape (Merkel et al., 2010).

In contrast, the bottom-up approach, also known as the constructive method, builds NPs atom-by-atom or molecule-by-molecule, allowing precise control over particle size, composition, and morphology (Adil et al., 2024). This approach also consists of three key methods. The first is chemical synthesis, which includes techniques such as the sol-gel process, chemical reduction, and co-precipitation, where chemical reactions in solution lead to NPs formation; second is biological synthesis, which employs microorganisms, plant extracts, or enzymes as natural reducing and stabilizing agents, offering an eco-friendly and biocompatible alternative; third is vapor phase synthesis, including spray pyrolysis and chemical vapor deposition (CVD), where gaseous precursors react or decompose to form NPs (Mekuye and Abera, 2023). Bottom-up methods typically produce NPs with better uniformity and fewer defects but may require more complex processing conditions.

The physical method, which is considered a top-down approach, and chemical and biological methods, which are considered bottom-up approaches, are indeed

the most commonly employed techniques for NPs synthesis due to their versatility and ability to produce NPs with desirable properties for various applications (Altammar, 2023). The details of the advantages and disadvantages of these three common synthesis methods are depicted in Table 1.2.

Table 1.2: Advantages and disadvantages of NPs synthesis methods (Altammar, 2023; Namakka et al., 2023).

Method	Description
Physical	Advantages: • Fast and simple Disadvantages: • Poor size control • High energy consumption • High capital costs
Chemical	Advantages: • Scalable and reproducible • Precise control over size and shape • Produce high-purity NPs Disadvantages: • Use toxic chemicals • Purification process requires
Biological	Advantages: • Eco-friendly and sustainable • Cost-effective

	• Less energy-intensive Disadvantage: • Slower synthesis

1.2.2 Application of nanoparticles (NPs)

NPs have a wide range of applications across many industries due to their unique physical, chemical, and biological properties that differ significantly from their bulk counterparts. Table 1.3 below illustrates the outline of these applications.

Table 1.3: Applications of NPs (Khan, Saeed, and Khan, 2017; Altammar, 2023).

Application area	Description
Medicine and Healthcare	Key benefits: • NPs enable highly targeted drug delivery systems, reducing side effects, medical imaging and diagnostics, and improving treatment efficacy. Examples: • Lipid NPs are used in COVID-19 vaccines (Seed, 2022). • Gold (Au) and silver (Ag) NPs are used in cancer therapy and antimicrobial applications.

	• Iron oxide (Fe_3O_4) NPs are used as magnetic resonance imaging (MRI) contrast agents. • Copper oxide (CuO) NPs are used in the production of facemasks.
	Key benefits: • NPs enhance food safety by detecting pathogens, fortifying food with essential nutrients, and improving packaging materials to extend shelf life.
Food industry	Examples: • Iron oxide (Fe_2O_3) and copper (Cu) NPs are used to fortify food products. • Inorganic and metal NPs are widely used as alternatives to petroleum-based food packaging plastics (Kumari and Sarkar, 2021).
	Key benefits: • NPs enhance water purification via catalytic degradation of pollutants and provide antibacterial coatings to prevent biofouling and contamination.
Environmental protection	Examples: • Silver (Ag) and titanium dioxide (TiO_2) NPs are used as antibacterial disinfectants in water purification (Bhardwaj et al., 2021).

	• Gold (Au) NPs are used as sensors for the detection of mercury in water (Kiran, 2014).
Agriculture industry	Key benefits: • NPs enhanced crop productivity, improving soil health, and enabling sustainable farming practices. Examples: • Zinc oxide (ZnO), silicon dioxide (SiO_2), and iron (Fe) NPs will improve fertilizer efficiency by enhancing nutrient uptake by plants and improving crop yield (Neme et al., 2021). • Nanobiosensors are used to monitor soil quality, nutrient levels, and pathogen presence (Neme et al., 2021).
Consumer products	Key benefits: • NPs benefit from their antimicrobial, ultraviolet (UV) protective, durability, and functionality. Examples: • Silica (SiO_2) NPs are used in lipstick (Fytianos, Rahdar, and Kyzas, 2020). • Titanium dioxide (TiO_2) and zinc oxide (ZnO) NPs are used in sunscreens (Lu et al., 2015).

1.3 Copper oxide nanoparticles (CuO NPs)

Copper oxide nanoparticles (CuO NPs) are transition metal oxide nanomaterials that typically crystallize in monoclinic structure, as illustrated in Figure 1.4 (Tran and Nguyen, 2014). Copper ions (Cu^{2+}) in CuO exhibit a valence state of +2 with an electronic configuration of $3d^9$, coordinating with oxygen ions (O^{2-}) in a distorted square planar geometry due to a coordination number of 4 (Tran and Nguyen, 2014). This coordination leads to the formation of CuO crystals characterized by their monoclinic lattice, which imparts unique electronic and magnetic properties to the material.

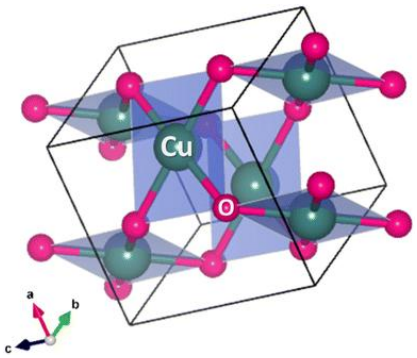

Figure 1.4: Crystal structure of monoclinic CuO NPs (Mobarak et al., 2025).

CuO NPs have gained widespread popularity due to their unique combination of physicochemical and biological properties that make them versatile across various fields. CuO NPs display a variety of morphologies depending on synthesis conditions. The morphology and sizes strongly influence their surface area, reactivity, and functional properties. CuO is a *p*-type semiconductor with a narrow bandgap (~1.2 eV), which arises from the presence of holes created by

copper vacancies and the mixed valence states of copper ions (Tran and Nguyen, 2014). This semiconducting behavior, combined with good chemical and thermal stability, makes CuO NPs attractive for applications in catalysis, sensors, antimicrobial agents, and energy devices.

CuO NPs also exhibit potent antimicrobial activity against a broad spectrum of bacteria, fungi, and viruses by the ability to generate reactive oxygen species that damage microbial cells, making them valuable in medical, food preservation, and agricultural applications (Amin et al., 2021). Additionally, CuO NPs possess anticancer properties, capable of inducing apoptosis in cancer cells, which has sparked significant interest in nanomedicine and targeted therapies (ScienceDirect, 2018). Compared to other metal NPs like silver and gold, CuO NPs are cost-effective and relatively easy to synthesize, which further drives their popularity for large-scale applications (Amin et al., 2021). These make CuO NPs a highly attractive subject of research and application.

1.4 Green Chemistry

Green chemistry is a scientific approach that aims to design products and processes in a way that reduces or eliminates the use and generation of hazardous substances throughout the entire life cycle, including design, manufacturing, usage, and disposal (Whiteker, 2019). Its primary goal is to minimize the negative impact of chemistry on human health and the environment by

promoting sustainability and safety. This approach is guided by the 12 Principles of Green Chemistry, which are shown in Figure 1.5.

Green method promotes environmentally friendly and sustainable methods for synthesizing NPs, often referred to as green synthesis. This approach utilizes natural biological resources such as plants, microorganisms, including bacteria, fungi, and algae, and their extracts as reducing and stabilizing agents to convert metal salts into NPs, eliminating the need for toxic chemicals and harsh physical conditions (Huston et al., 2021). The general process involves extracting bioactive molecules from plant parts like leaves, roots, fruits, and flowers, which then reduce metal ions in solution to form NPs under controlled temperature (Huston et al., 2021). These bioactive molecules will also cap and stabilize the NPs, enhancing their stability and functionality. This method is cost-effective, energy-efficient, and produces biocompatible NPs with controlled size and morphology.

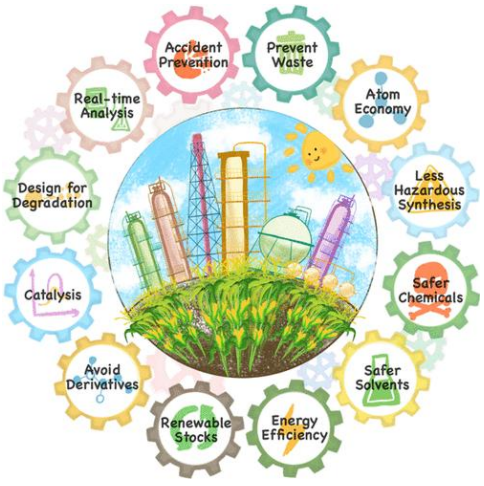

Figure 1.5: Principles of green chemistry (Whiteker, 2019).

1.5 *Annona muricata* (Soursop)

Annona muricata, also known as soursop, produces the largest fruit in the Annonaceae family (ScienceDirect, 2019). The generic name *Annona* is derived from Latin, which consists of the meaning “annual harvest” or “yearly produce” (Carlos De Queiroz Pinto, 2025).

A. muricata is an evergreen tree that typically grows to a height of 4 - 8 meters (Carlos De Queiroz Pinto, 2025). It features evergreen leaves measuring between 6.25 - 20.00 cm in length and produces distinctive flowers with six yellow-green petals (National Parks Board, 2025). Its fruit is easily recognizable by its yellow-green color when ripe, has a lopsided heart shape, and a spiny outer skin (Hafeezul, 2025). Inside, the fruit contains a pulpy interior filled with numerous seeds and can weigh up to 10 kg (ScienceDirect, 2019). This unique combination of botanical characteristics and substantial fruit size makes *A. muricata* a notable species both horticulturally and nutritionally.

In Malaysia, *A. muricata*, also known as “Durian Belanda”, is widely cultivated and highly valued, thriving in the country’s tropical climate (ScienceDirect, 2019). It is commonly grown in family orchards and commercial plantations across tropical regions in Malaysia, thriving best in sandy, well-drained soil with adequate watering and protection from strong winds (Hafeezul, 2025). The tree grows rapidly and typically starts fruiting within three to five years after planting

(Hafeezul, 2025). The different plant parts of *A. muricata* are depicted in Figure 1.6.

(a) Leaves

(b) Flowers

(c) Seeds

(d) Fruits

(e) Barks and stems

Figure 1.6: Various plant parts of *A. muricata*, (a) leaves, (b) flowers, (c) seeds, (d) fruits, (e) barks and stems.

1.5.1 Various traditional and modern uses of *A. muricata* (Soursop) parts.

Beyond its distinctive botanical characteristics and widespread cultivation, *A. muricata* is highly valued for its diverse uses across different parts of the plant. Various uses of each plant part of *A. muricata* were outlined in Table 1.4.

Table 1.4: Usages of each plant part of *A. muricata* (Gavamukulya, Wamunyokoli, and El-Shemy, 2017; Solanki, Mandaliya, and Georrge John. J, 2020; Sachdev, 2022; Zubaidi et al., 2023).

Plant parts of *A. muricata*	**Traditional and modern uses**
Leaves	• Used in traditional medicine - Treats fever, hypertension, ulcers, and insomnia due to their diverse therapeutic properties. - Possess anticancer effects which has the potential to induce apoptosis in cancer cells. • Make soursop leaf tea
Flowers	• Used in traditional medicine - Primarily for their anti-inflammatory and anthelmintic effects.
Seeds	• Used as a natural pesticide - Due to the presence of toxic compounds.
Fruits	• Make desserts, smoothies, and juices - Due to its sweet and tangy flavor. • Used to alleviate symptoms of fever, diarrhea, and arthritic pain. - Valued for its antioxidant and anti-inflammatory effects.

1.6 Objectives

This project aimed to synthesize copper oxide nanoparticles (CuO NPs) from plant extract at various calcination temperatures and characterized them. The detailed objectives of this study are as follows:

1. To synthesize CuO NPs from the aqueous extract of the barks of *A. muricata* through a green synthetic pathway using copper(II) nitrate trihydrate, $Cu(NO_3)_2 \cdot 3H_2O$ as precursor salt.

2. To characterize the synthesized CuO NPs using Ultraviolet-Visible Spectroscopy (UV-Vis), Fourier Transform-Infrared Spectroscopy (FT-IR), Field Emission Scanning Electron Microscopy (FESEM), Energy Dispersive X-ray Spectroscopy (EDX), and X-ray Diffraction (XRD).

3. To determine the effect of calcination temperature on the CuO NPs synthesized via the green synthesis method.

CHAPTER 2

LITERATURE REVIEW

2.1 Green synthesis of copper oxide nanoparticles (CuO NPs)

Recently, there has been a lot of interest in the green synthesis of CuO NPs over conventional physical and chemical synthesis methods. This approach utilizes plant sources as natural reducing, stabilizing, and capping agents to produce NPs in an environmentally friendly and sustainable manner (Madeshwaran and Venkatachalam, 2024). Various plant parts, such as leaves, flowers, barks, fruits, stems, and seeds, are rich in bioactive phytochemicals, which are employed to reduce Cu^{2+} ions to copper atoms and further decompose into CuO NPs during the calcination process.

The green synthesis of CuO NPs can occur through two primary mechanisms, which are chelation-based complex formation and bioreduction, which work synergistically. First, the chelation-based complex formation mechanism in the green synthesis of CuO NPs involves the formation of complexes between Cu^{2+} and bioactive compounds present in the plant extract. These bioactive molecules contain functional groups like hydroxyl (-OH), carbonyl (C=O), and amine (-NH) groups that coordinate with Cu^{2+} ions, forming stable Cu-phytochemical complexes (Mobarak et al., 2025). These Cu-phytochemical complexes then undergo thermal decomposition during the calcination process, leading to the release of reduced copper species that nucleate to form CuO NPs (Mobarak et al., 2025). Thus, chelation serves as a crucial precursor step that controls the

nucleation and growth of NPs, ensuring uniform size and shape. Furthermore, the phytochemicals adsorb onto the surface of the forming NPs, acting as capping agents that prevent aggregation by providing steric hindrance and electrostatic stabilization (Mobarak et al., 2025). This capping enhances the stability and dispersity of the NPs in solution. The chelation-based complex formation mechanism of CuO NPs was depicted in Figure 2.1. In parallel, the bioreduction mechanism occurs by stabilizing the copper(II) ions and facilitating their controlled reduction to copper atoms, followed by further oxidation to form CuO NPs (Mobarak et al., 2025). During this process, the phytochemicals themselves are oxidized, acting as reducing agents by donating electrons to Cu^{2+} ions.

Figure 2.1: Chelation-based complex formation mechanism of CuO NPs (Mobarak et al., 2025).

2.2 Phytochemical compositions in *A. muricata*

Phytochemical compositions present in *A. muricata* extracts are diverse and include several bioactive groups. These phytochemicals contribute to the plant's antioxidant, antimicrobial, anticancer, anti-inflammatory, and other

pharmacological properties (Anarado et al., 2020). They also play a crucial role in the green synthesis of CuO NPs by acting as reducing, stabilizing, and capping agents (Madeshwaran and Venkatachalam, 2024). Table 2.1 indicates the major phytochemical compositions present in the aqueous extract of the barks of *A. muricata* along with the types of tests used and observations (Kazaure et al., 2025).

Table 2.1: Summary of phytochemical screening of aqueous extract of the barks of *A. muricata* along with the types of tests used and observations (Anarado et al., 2020; Sudhashini et al., 2023; Kazaure et al., 2025).

Phytochemical compound	Test used	Observation	Result
Alkoloids	Mayer's test	A cream color precipitate was observed.	(+)
	Wagner's test	A reddish-brown precipitate was observed.	(+)
	Dragendorff's test	An orange-red precipitate was observed.	(+)
Flavonoids	Ammonium test	A yellow-colored solution was observed.	(+)
	Aluminium chloride test	A yellow-colored solution was observed.	(+)
Tannins	Ferric chloride test	A greenish-black precipitate was observed.	(+)

	Lead(II) acetate test	A cream precipitate was observed.	(+)
Saponins	Froth test	Froth was observed at first. After the addition of olive oil, an emulsion appeared.	(+)
Terpenoids	Salkowski's test	A reddish-brown precipitate was observed.	(+)
Cardiac glycosides	Keller Killiani test	A brown ring (above) and a violet ring (below) were observed.	(+)

(+): Positive results (Present)

(-): Negative results (Absent)

2.3 Green synthesis of CuO NPs using plant extract

2.3.1 Green synthesis and characterization of CuO nanorods using *Muntingia calabura* leaves extract

In the study conducted by Selvanathan et al. (2021), *Muntingia calabura* leaves extract was utilized to synthesis of CuO nanorods. It is commonly known worldwide as "Jamaican cherry", as depicted in Figure 2.2, and is often grown as roadside trees in Malaysia (Selvanathan et al., 2021). Traditionally, the leaves of *M. calabura* have been used in various cultures as a tranquilizer, headache remedy, and tonic (Selvanathan et al., 2021). The distinctive blend of phytochemicals present in the *M. calabura* leaf extract makes it an excellent natural medium for synthesizing CuO NPs with unique morphology features (Selvanathan et al., 2021). In this study, $Cu(NO_3)_2{\cdot}3H_2O$ was utilized as precursor salt, and the paste was calcinated at 400°C for two hours. The detailed experimental procedure is shown in Figure 2.3(a), while Figure 2.3(b) illustrates the reaction mechanism for CuO NPs synthesis.

Figure 2.2: Appearance of *M. calabura* (Ecosostenibile, 2024).

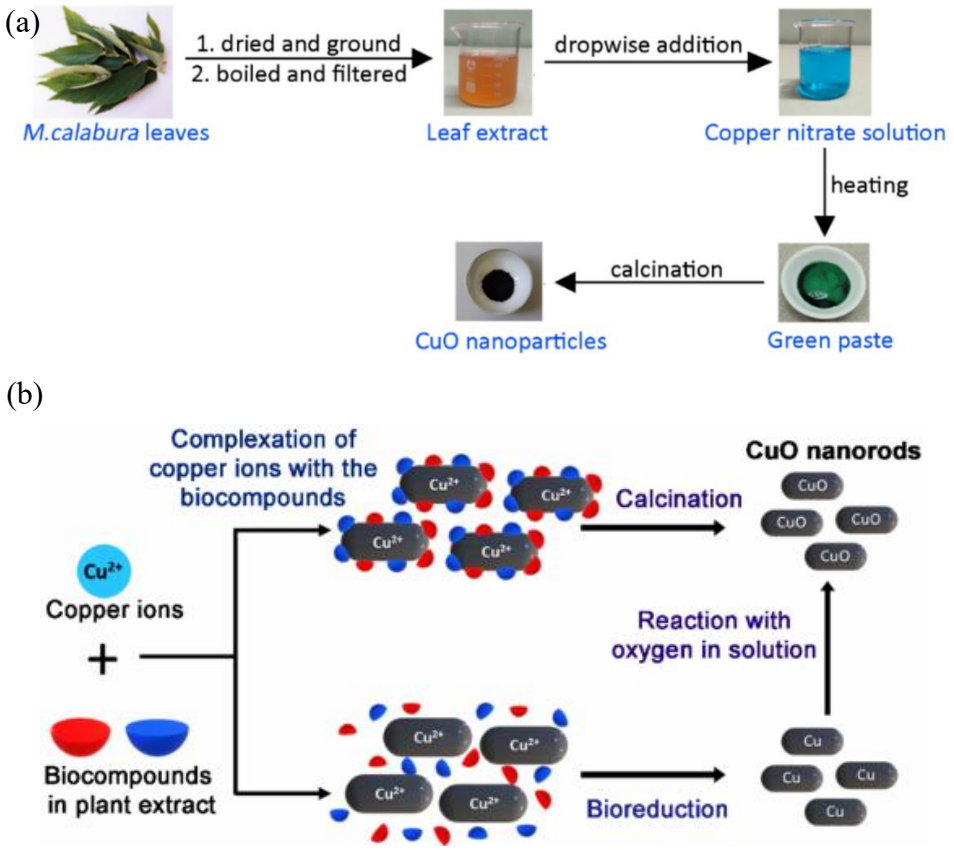

Figure 2.3: (a) Experimental procedure and (b) reaction mechanism for CuO NPs synthesis using *M. calabura* leaves extract (Selvanathan et al., 2021).

The XRD analysis shows that the synthesized CuO NPs exhibited a monoclinic crystalline structure, which matched with the International Centre for Diffraction Data (ICDD) Card No. 00-045-0937. In Figure 2.4, the diffraction peaks at 2θ were found at 32.51°, 36.32°, 39.20°, 49.42°, 58.87°, 62.26°, 66.90°. 68.70°, 73.05°, and 75.68°, which matched the planes of (0 3 1), (0 0 2), (1 1 1), (2 0 -2), (2 0 2), (1 1 -3), (3 1 -1), (1 1 3), (3 1 1), and (0 0 4), respectively. Based on the prominent XRD peaks, the synthesized CuO NPs show an average crystalline size ranging from 12 - 20 nm (Selvanathan et al., 2021).

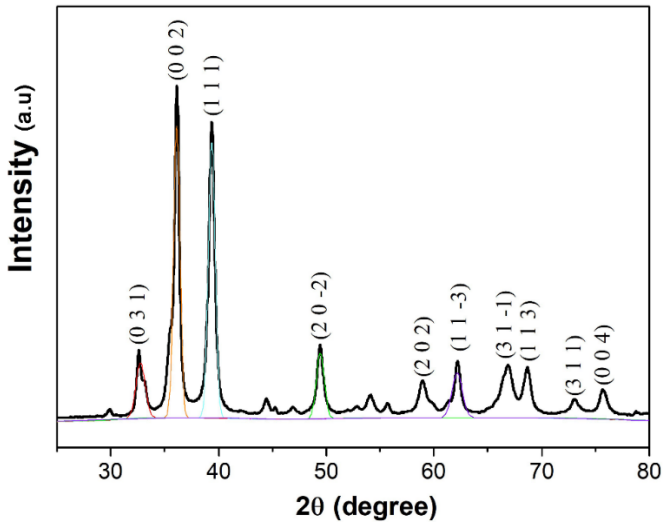

Figure 2.4: XRD pattern of synthesized CuO NPs from *M. calabura* leaves extract (Selvanathan et al., 2021).

From Figure 2.5, the synthesized CuO NPs consist of a maximum absorption peak at 387 nm, and the band gap energy (E_g) determined using the Tauc plot was found to be 3.65 eV.

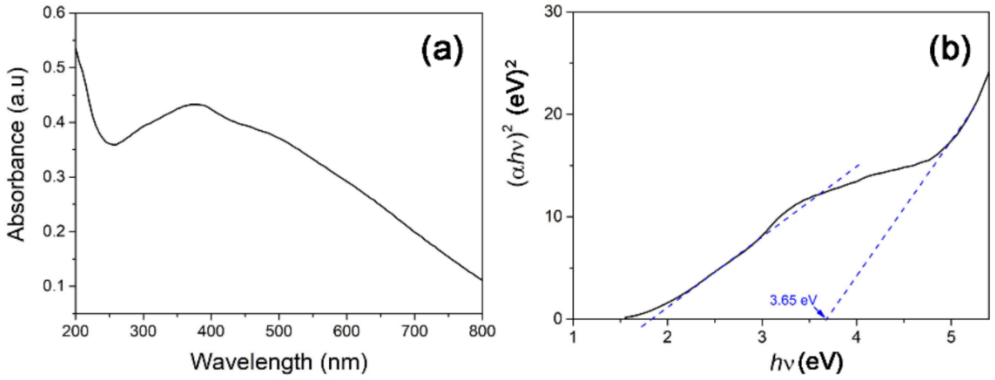

Figure 2.5: (a) UV-Vis absorption spectrum, and (b) Tauc plot of synthesized CuO NPs from *M. calabura* leaves extract (Selvanathan et al., 2021).

According to Figure 2.6(a), the structural properties of synthesized CuO NPs, which were characterized by using FESEM analysis, displayed a rod-shaped morphology with uniform size and exhibited less agglomeration. The elemental compositions of synthesized CuO NPs using EDX analysis are shown in Figure 2.6(b) and indicate the absence of contamination.

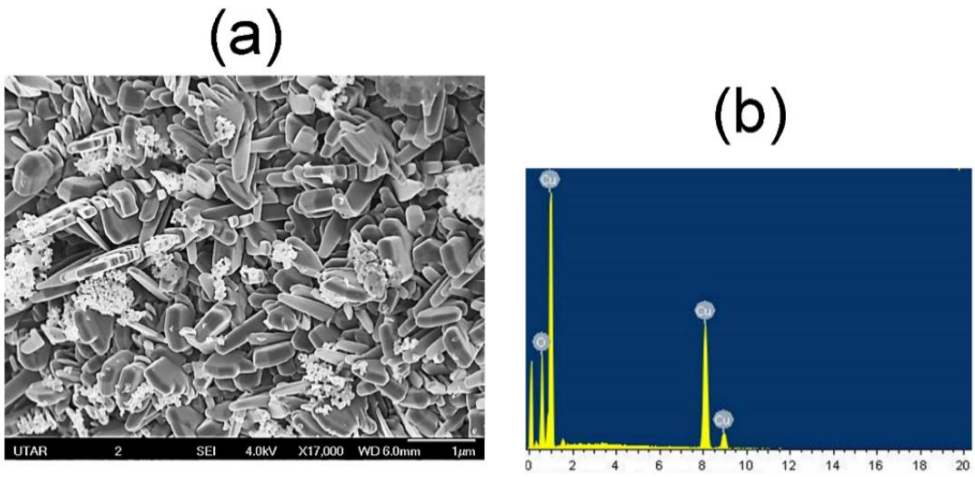

Figure 2.6: (a) FESEM image, and (b) EDX spectrum of synthesized CuO NPs from *M. calabura* leaves extract (Selvanathan et al., 2021).

The Transmission Electron Microscopy (TEM) images (Figure 2.7) clearly show that the synthesized CuO NPs consist of a rod shape with a thickness of around 23 nm and a length ranging from 79 - 90 nm, which is larger than the crystalline size determined from XRD analysis.

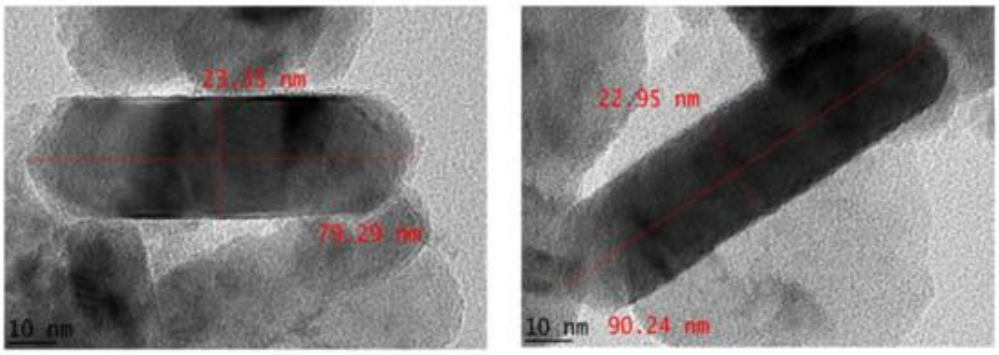

Figure 2.7: TEM images of synthesized CuO NPs from *M. calabura* leaves extract (Selvanathan et al., 2021).

Based on the FT-IR spectrum depicted in Figure 2.8(a), the O-H and C=O stretching bonds can be observed at 3413 and 1630 cm^{-1}, corresponding to polyphenols and flavonoids, respectively. Absorption bands at 1414 and 1034 cm^{-1} are from carboxylic acid (-COO) and amine stretch (C-N), respectively. Furthermore, bands between 1100 - 1000 cm^{-1} indicate the presence of carbohydrate components in the *M. calabura* leaf extract. Based on the spectrum in Figure 2.8(b), the strong absorption bands at 3428 and 1640 cm^{-1} correspond to the phenolic group and flavonoids, respectively, served as stabilizing and capping agents during the synthesis of CuO NPs. Lastly, the intense band at 452 cm^{-1} is a significant absorption band that indicates the presence of CuO NPs.

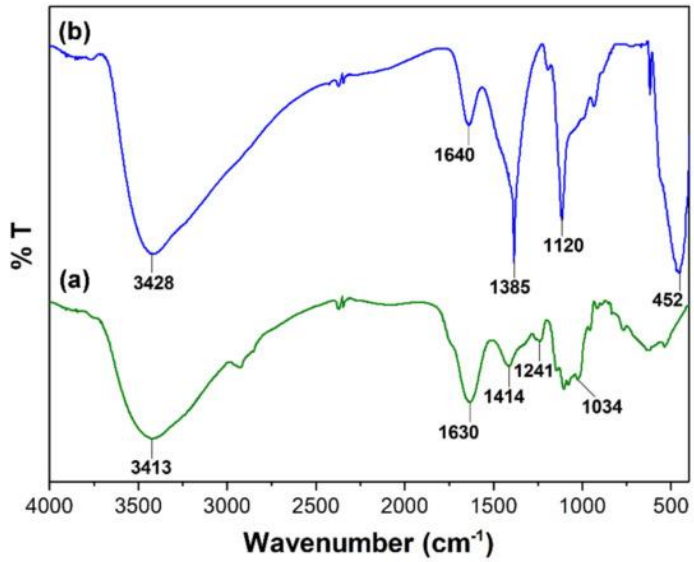

Figure 2.8: FT-IR spectra of (a) *M. calabura* leaves extract, and (b) synthesized CuO NPs (Selvanathan et al., 2021).

2.3.2 Green synthesis and characterization of CuO NPs using *Pyrus pyrifolia* leaves extract

In this study, Sundaramurthy and Parthiban (2015) utilized the leaves of *Pyrus pyrifolia* in the synthesis of CuO NPs. *P. pyrifolia*, as depicted in Figure 2.9, commonly known as "Asian pear", belongs to the Rosaceae family and is valued for its large, round to slightly pyriform fruits that typically measure 3 - 4 inches in diameter (NC State Extension, 2025). In this study, $Cu(NO_3)_2{\cdot}6H_2O$ was utilized as the precursor salt, and the calcination process was carried out at 400°C for three hours.

Figure 2.9: Appearance of *P. pyrifolia* (NC State Extension, 2025).

The XRD diffractogram (Figure 2.1) showed sharp and narrow diffraction peaks, indicating that the synthesized CuO NPs have a monoclinic phase and a highly crystalline structure, which matched the ICDD Card No. 45-0937. The diffraction peaks at 2θ were found at 32.49°, 35.47°, 38.70°, 48.75°, 53.59°, 58.23°, 61.57°, 66.01°, 68.01°, 72.45° and 74.92°, which matched to the planes of (1 1 0), (0 0 2), (1 1 1), (2 0 2), (0 2 0), (2 0 2), (1 1 3), (3 1 1), (2 2 0), (3 1 1) and (0 0 4) respectively. The average size was found to be 22 nm (Sundaramurthy and Parthiban, 2015).

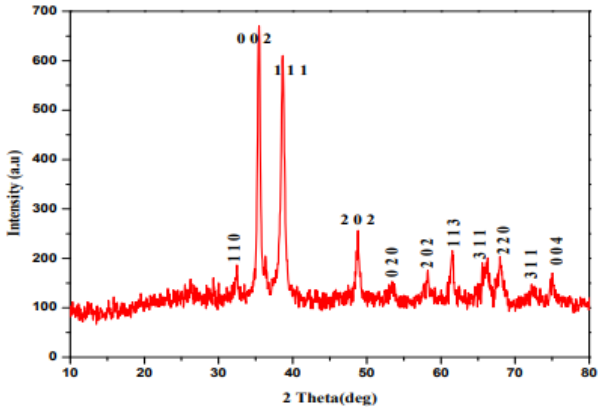

Figure 2.10: XRD pattern of synthesized CuO NPs from *P. pyrifolia* leaves extract (Sundaramurthy and Parthiban, 2015).

Based on FESEM analysis illustrated in Figure 2.11(a), the synthesized CuO NPs are small, uniform in size, and mostly spherical in shape, which are free from agglomeration. The particle size ranged from 17 - 30 nm, and the average particle size detected was 24 nm, which is nearly identical to XRD analysis. The atomic determination of synthesized CuO NPs, as illustrated in Figure 2.11(b), showed that only Cu and O elements are present.

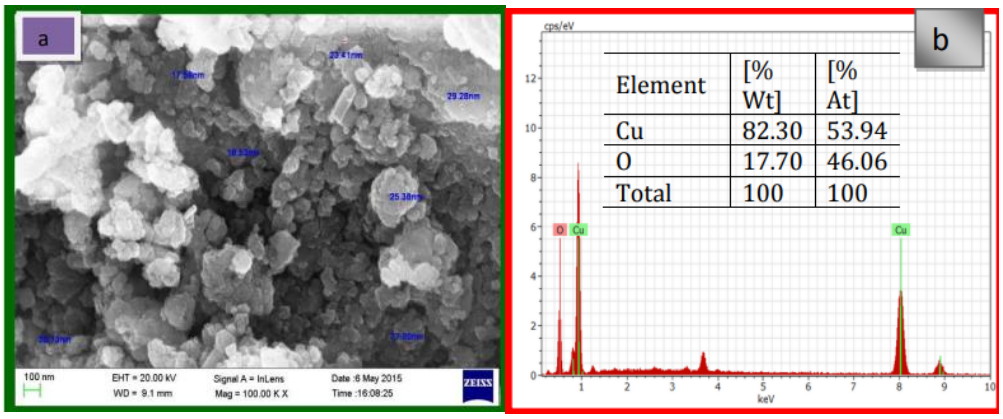

Figure 2.11: (a) FESEM image, and (b) EDX spectrum of synthesized CuO NPs from *P. pyrifolia* leaves extract (Sundaramurthy and Parthiban, 2015).

Based on the FT-IR spectrum revealed in Figure 2.12(b), the strong absorption band at 3435 cm^{-1} corresponds to O-H stretching due to the presence of hydroxyl groups. The absorption bands at 2362 and 1637 cm^{-1} indicate the C-H stretching of alkanes and C=O stretching, respectively. Lastly, the intense band observed at 528 cm^{-1} indicates the presence of CuO NPs.

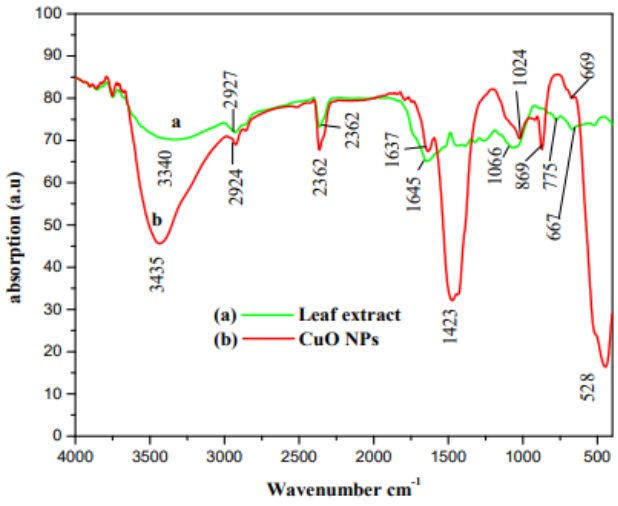

Figure 2.12: FT-IR spectra of (a) *P. pyrifolia* leaves extract, and (b) synthesized CuO NPs (Sundaramurthy and Parthiban, 2015).

2.3.3 Green synthesis and characterization of CuO NPs using *Carica papaya L.* peel extract

This study, which was conducted by Phang et al. (2021), utilized the peels from *Carica papaya L.* for the synthesis of CuO NPs. *Carica papaya L.*, as shown in Figure 2.13, commonly known as papaya, is a member of the Caricaceae family, which grows in many tropical and subtropical regions around the world. This *Carica papaya L.* fruit is valued for its rich content of vitamins such as β-carotene, vitamin C, and vitamin E, as well as essential minerals like sodium, calcium, and iron, along with dietary fiber (Phang et al., 2021). The juice has also been traditionally employed in the treatment of diseases such as constipation, diabetes, high blood pressure, and others (Phang et al., 2021). In this study, the precursor salt utilized in the synthesis of CuO NPs is $Cu(NO_3)_2{\cdot}3H_2O$, and calcinated at 450°C for two hours. The detailed experimental procedure is shown in Figure 2.14.

Figure 2.13: Appearance of *Carica papaya L.* (Phang et al., 2021).

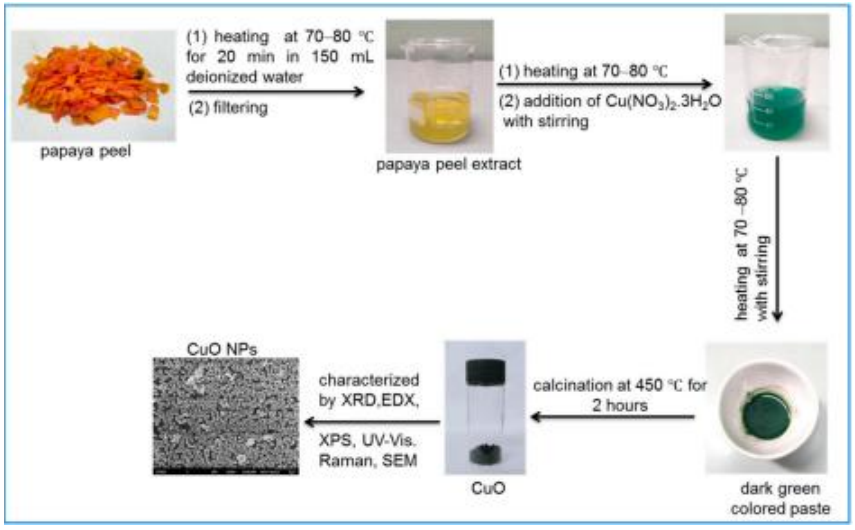

Figure 2.14: Experimental procedure for CuO NPs synthesis using *Carica papaya L.* peel extract (Phang et al., 2021).

The XRD analysis depicted in Figure 2.15(a) revealed that the synthesized CuO NPs exhibited a monoclinic structure, which is in agreement with the peaks in the ICDD Card No. 00-045-0937. The diffraction peaks at 2θ were found at 32.51°, 35.53°, 38.75°, 46.26°, 48.78°, 53.50°, 58.34°, 61.57°, 66.28°, 68.04°, 72.46°, and 75.0°, which matched to the planes of (-1 1 0), (0 0 2), (1 1 1), (-1 1

2), (-2 0 2), (0 2 0), (2 0 2), (-1 1 3), (0 2 2), (-2 2 0), (3 1 1) and (0 0 4) respectively. Lastly, the crystalline size was found to be 28.06 nm (Phang et al., 2021). The atomic determination of synthesized CuO NPs, as shown in Figure 2.15(b), indicates that only Cu and O elements are present. According to Figure 2.16, the synthesized CuO NPs exhibited an agglomerated spherical shape with the particle sizes ranging from 85 – 140 nm.

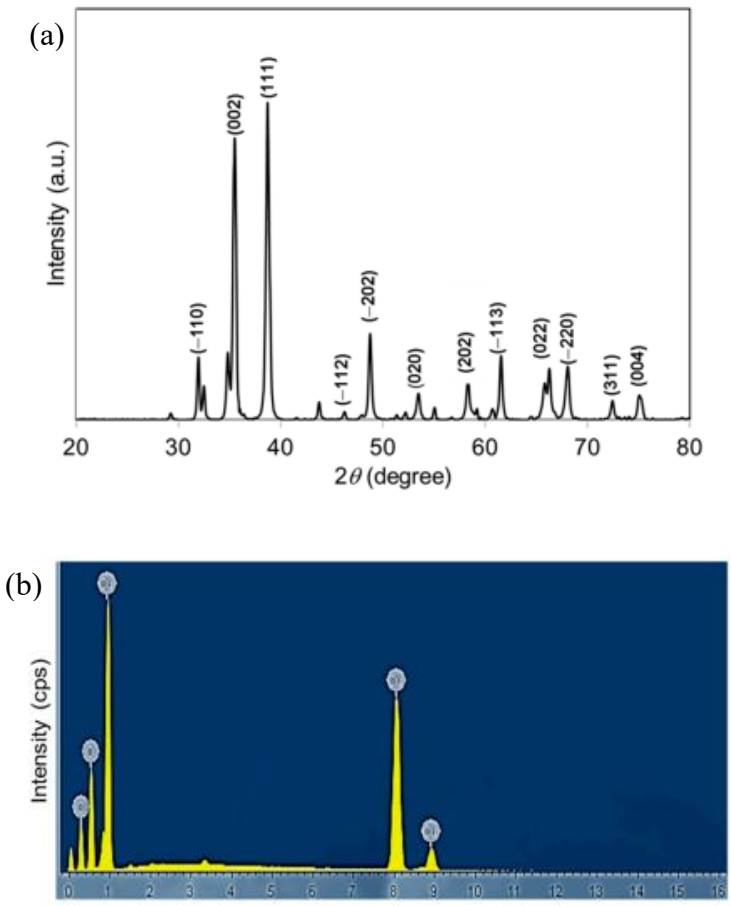

Figure 2.15: (a) X-ray diffractogram and (b) EDX spectrum of synthesized CuO NPs from *Carica papaya L.* peel extract (Phang et al., 2021).

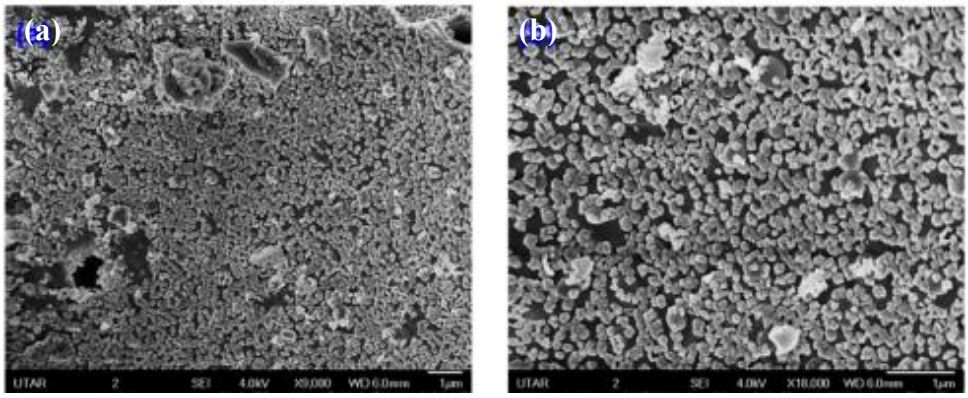

Figure 2.16: SEM images of synthesized CuO NPs from *Carica papaya L.* peel extract with magnification of (a) 9000x and (b) 18000x (Phang et al., 2021).

According to the FT-IR spectrum illustrated in Figure 2.17(b), the absorption bands at 3368 and 1647 cm^{-1} correspond to the stretching vibrations of hydroxyl groups and primary amide groups, respectively. The absorption band at 1120 cm^{-1} is attributed to C-O stretching. The key intense band observed at 532 cm^{-1} corresponds to the stretching vibration of the Cu-O bond in the monoclinic synthesized CuO NPs.

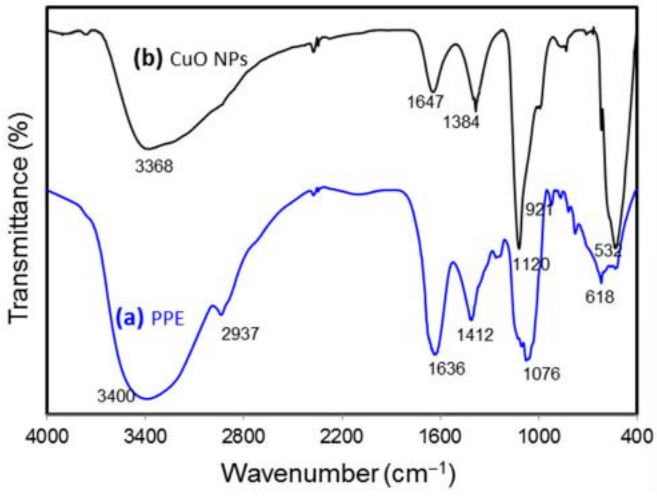

Figure 2.17: FT-IR spectra of (a) *Carica papaya L.* peel extract and (b) synthesized CuO NPs (Phang et al., 2021).

2.3.4 Green synthesis and characterization of CuO NPs using *Allium sativum* extract

Velsankar et al. (2020) explored the synthesis of CuO NPs by utilizing the *Allium sativum* extract. *A. sativum*, as shown in Figure 2.18, commonly known as garlic, is a bulbous flowering plant belonging to the member of Amaryllidaceae family (Velsankar et al., 2020). It is widely valued not only for its distinctive pungent taste and aroma that enhances culinary dishes worldwide but also for its diverse medicinal benefits, including antioxidant, anticancer, and anti-inflammatory effects (Velsankar et al., 2020). In this study, copper(II) nitrate was utilized as the precursor salt in the synthesis of CuO NPs, and calcinated at 400°C in the furnace for three to four hours.

Figure 2.18: Appearance of *A. sativum* (Chauhan, 2025).

From Figure 2.19(a), the diffraction peaks at 2θ from XRD analysis were found at 32.22°, 35.42°, 38.64°, 48.60°, 53.20°, 56.67°, 58.02°, 61.32°, 66.10°, 68.05°, 71.96°, and 74.80°, which are coordinated with the crystalline planes of (1 1 0), (0 0 2), (1 1 1), ($\bar{2}$ 0 2), (0 2 0), (0 2 1), (2 0 2), ($\bar{1}$ 1 3), ($\bar{3}$ 1 1), (2 2 0), ($\bar{3}$ 1 2), and (0 0 4), respectively. This showed that the synthesized CuO NPs consist of a crystalline nature with a monoclinic structure, which matched the ICDD Card No. 80-1917. The mean crystalline size was found in the range from 25 - 30 nm by using Scherrer's equation (Velsankar et al., 2020).

Based on Figure 2.19(b), the absorption bands at 3465 cm^{-1} correspond to O-H bond of hydroxyl groups. The bands at 2921 and 2851 cm^{-1} are linked to the stretching vibrations of C-H and -CH_2 from primary alkanes, respectively. The band at 1689 cm^{-1} corresponds to amide bond. Furthermore, bands observed at 1466 and 1385 cm^{-1} are related to the stretching vibrations of aliphatic and aromatic C-N amine, respectively. The bands at 1110 and 1043 cm^{-1} were linked to carboxylic and phenolic groups, respectively. Lastly, sharp and intense bands at 584 and 531 cm^{-1} indicate Cu-O bond in synthesized CuO NPs.

The synthesized CuO NPs consist of a maximum absorption peak at 398 nm, and the band gap energy (E_g) determined using the Tauc plot was found to be 3.20 eV, as illustrated in Figure 2.19(c) and (d).

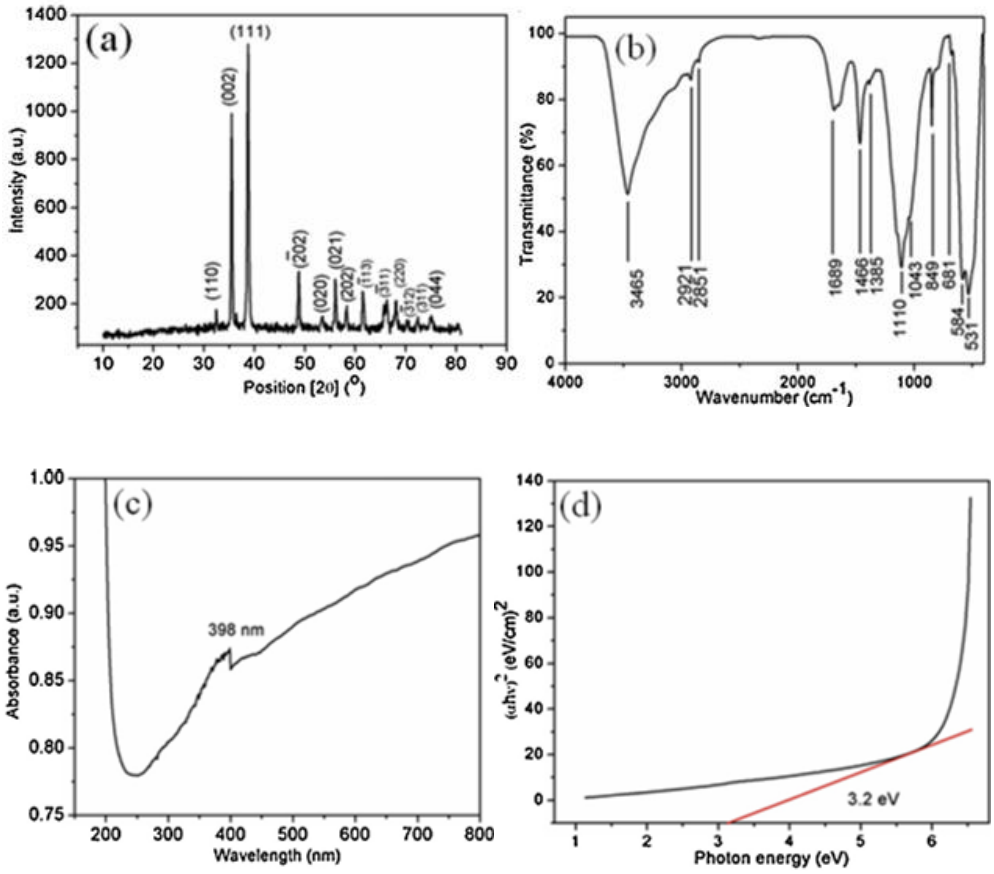

Figure 2.19: (a) X-ray diffractogram, (b) FT-IR spectrum, (c) UV-Vis absorption spectrum, and (d) Tauc plot of synthesized CuO NPs from *A. sativum* extract (Velsankar et al., 2020).

Based on the SEM study (Figure 2.20), the synthesized CuO NPs mostly exhibit a spherical, circular, and oval shape and particle size ranging from 20 - 40 nm.

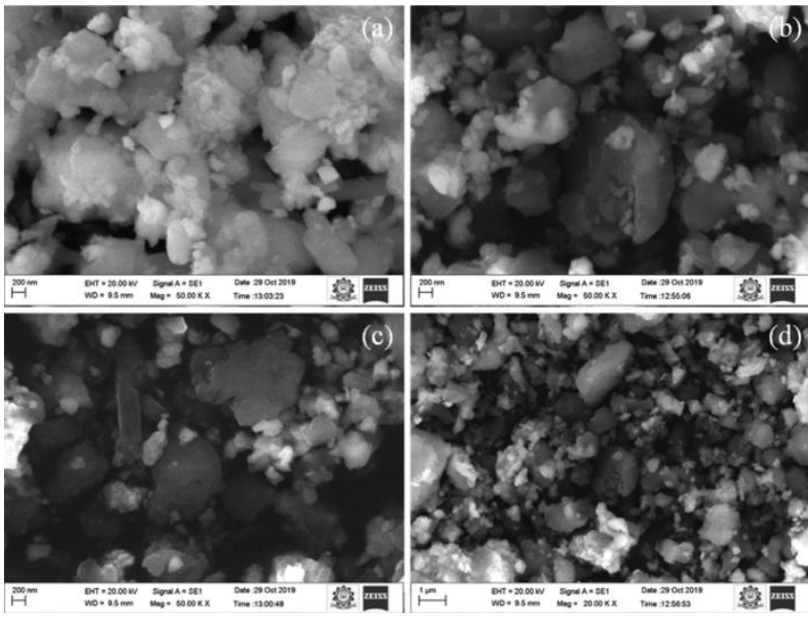

Figure 2.20: SEM images of synthesized CuO NPs from *A. sativum* extract at (a-c) 200 nm, and (d) at 1 μm scale range (Velsankar et al., 2020).

The atomic composition of the synthesized CuO NPs, as determined by using EDX analysis, as in Figure 2.21, indicated that only Cu and O elements were present with no contamination. The weight percentages of Cu and O elements are shown in Table 2.2.

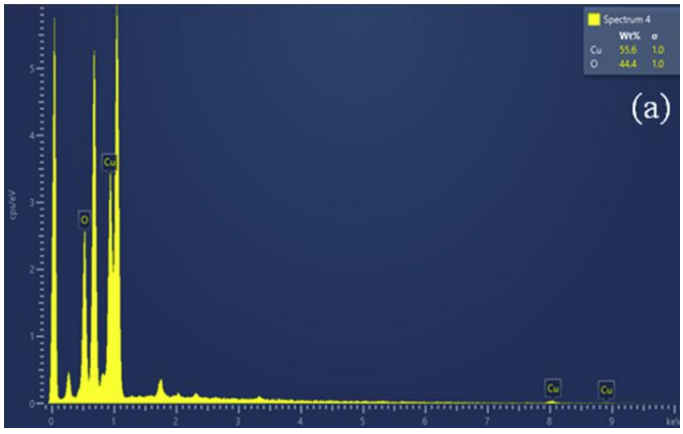

Figure 2.21: EDX spectrum of synthesized CuO NPs (Velsankar et al., 2020).

Table 2.2: Weight and atomic percentages of O and Cu of CuO NPs from EDX analysis (Velsankar et al., 2020).

Element	Weight %	Atomic %
O	44.40	76.03
Cu	55.60	23.97
Total	100.00	100.00

2.4 Experimental parameters that influence the synthesis of CuO NPs

The green synthesis of CuO NPs utilizing plant extracts is greatly affected by several factors. The study conducted by Chan et al. (2022) in the synthesis of CuO NPs focuses on investigating the effect of the calcination temperature. *Garcinia mangostana L.* leaves extract and $Cu(NO_3)_2{\cdot}3H_2O$ are used as stabilizing agents and precursor salts, respectively. The detailed experimental procedure is shown in Figure 2.22.

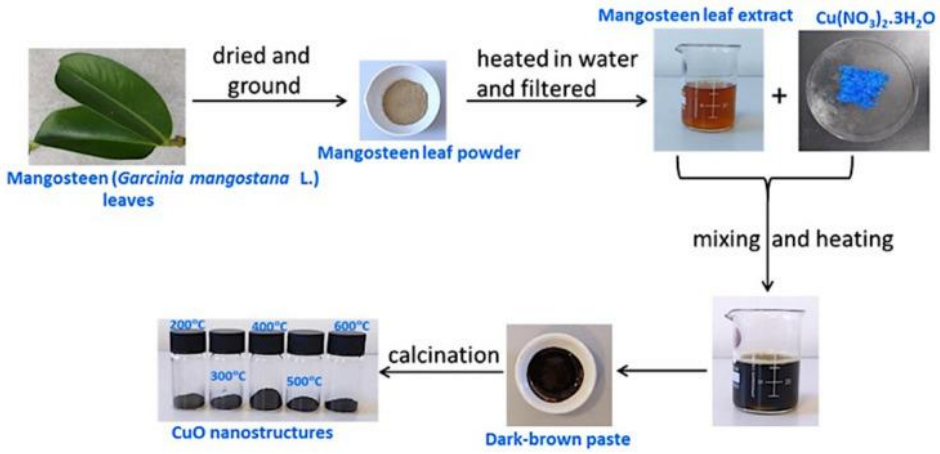

Figure 2.22: Summary of experimental procedure for green synthesis of CuO NPs (Chan et al., 2022).

The crystal structure of CuO NPs, which were synthesized using 30 mL of the *Garcinia mangostana* L. leaves extract and calcined at various temperatures of 200, 300, 400, 500, and 600°C, was determined by XRD analysis, and the results are illustrated in Figure 2.23. It indicates that the synthesized CuO NPs have a monoclinic phase, which matches the ICDD Card No. 00-045-0937, and the intensity and sharpness of the diffraction peaks increase with increasing calcination temperature. The mean crystalline size for the synthesized CuO NPs at variations of calcination temperature, as shown in Table 2.3, was found in the range from 12.78 - 28.17 nm by using Scherrer's equation. The optical bandgap energy of the synthesized CuO NPs decreases when the calcination temperature is elevated, as illustrated in Table 2.3, indicating an increase in particle size alongside a decrease in lattice strain.

Table 2.3: Energy band gap and mean crystalline size of the synthesized CuO NPs at different calcination temperatures (Chan et al., 2022).

Calcination temperature (°C)	Energy bandgap (eV)	Mean crystalline size (nm)
200	3.41	12.78
300	3.28	14.04
400	3.24	18.32

500	3.19	19.88
600	3.19	28.17

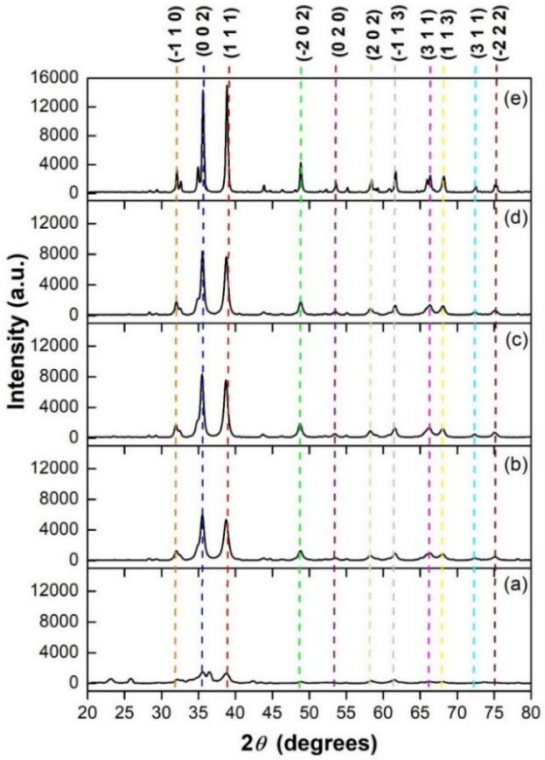

Figure 2.23: X-ray diffractogram of synthesized CuO NPs at calcination temperatures of (a) 200, (b) 300, (c) 400, (d) 500, and (e) 600°C (Chan et al., 2022).

Atomic composition of the synthesized CuO NPs, as determined by using EDX analysis, is depicted in Figure 2.24. It indicated that at low calcination temperatures of 200, 300, and 400°C, a weak carbon signal was detected, indicating the presence of impurities. As calcination temperature increases to 500 and 600°C, the carbon signal diminishes and eventually disappears, showing

that the organic components are completely removed, typically converted to carbon dioxide and water, and only Cu and O elements are present.

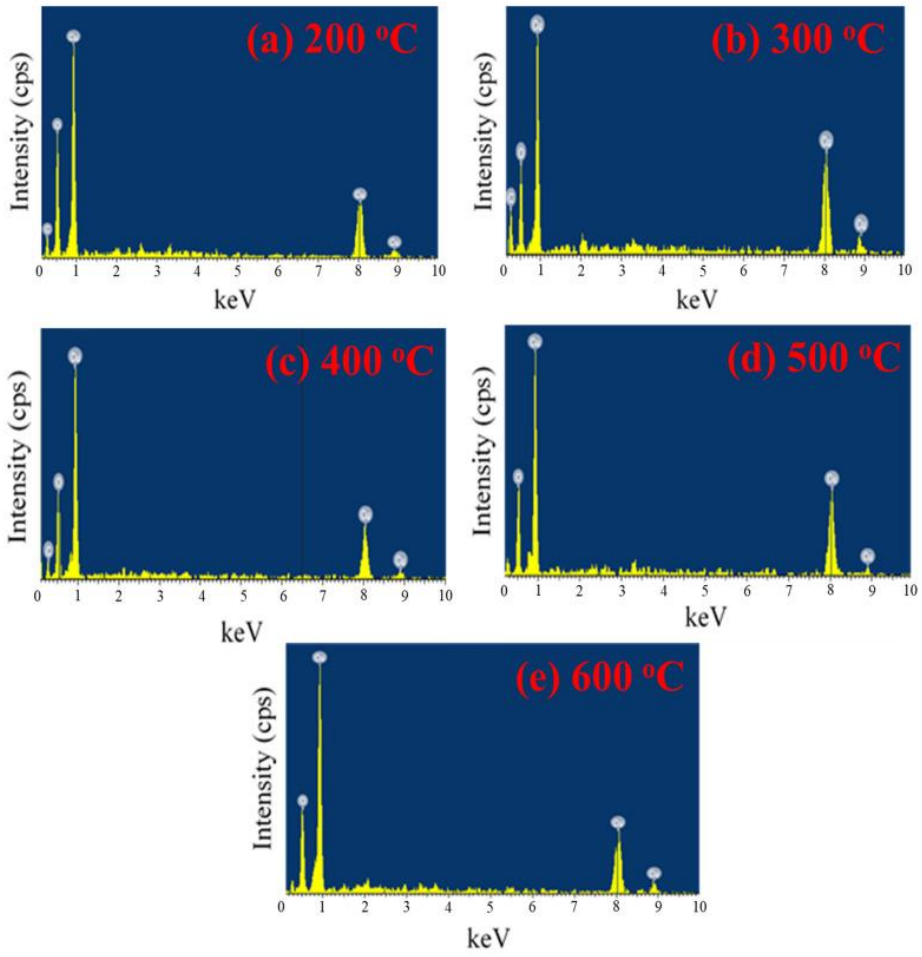

Figure 2.24: EDX spectrum of synthesized CuO NPs at calcination temperatures of (a) 200, (b) 300, (c) 400, (d) 500, and (e) 600°C (Chan et al., 2022).

Figure 2.25 shows the FESEM analysis for the synthesized CuO NPs at various calcination temperatures. It was observed that particle size increased with rising calcination temperature, with the reported average size of synthesized CuO NPs ranging from 50.0 - 458.3 nm.

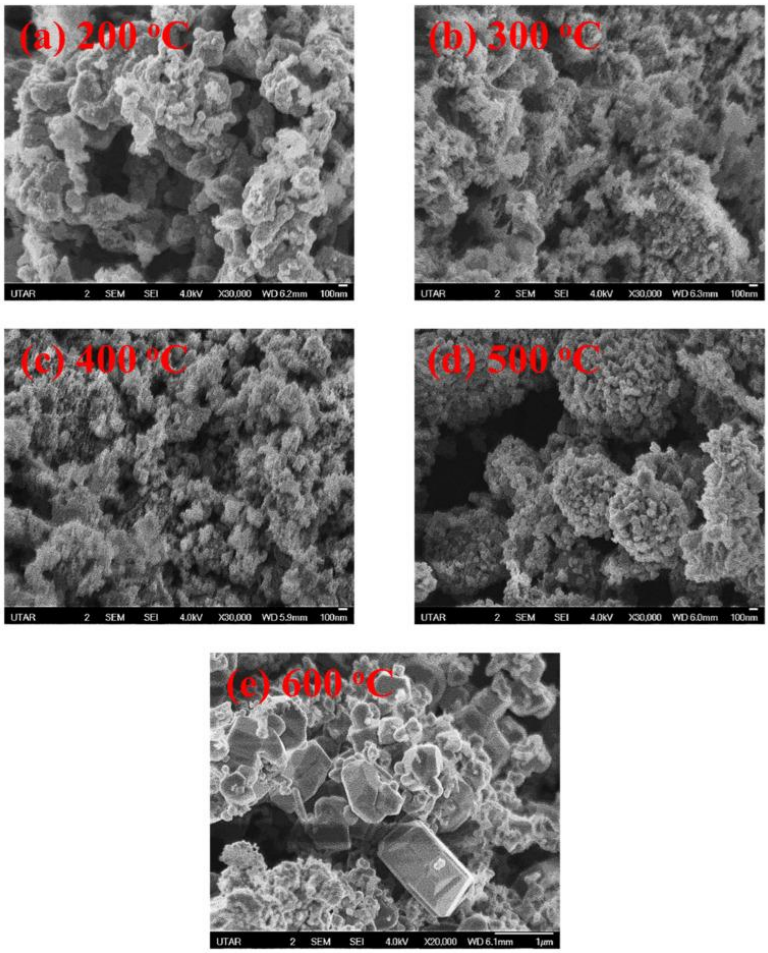

Figure 2.25: FESEM images of synthesized CuO NPs at calcination temperatures of (a) 200, (b) 300, (c) 400, (d) 500, and (e) 600°C (Chan et al., 2022).

2.5 Concluding remarks

From these studies, it has been proven that plants can be utilized in the synthesis of CuO NPs. This is because plant extracts contain various bioactive phytochemicals such as polyphenols, flavonoids, alkaloids, terpenoids, tannins, and others. They will act as natural reducing, stabilizing, and capping agents in

the synthesis process. In this study, effect of calcination temperature on the crystalline size of synthesized CuO NPs was studied due to the limited number of studies available. Furthermore, the utilization of the barks of the plants in the synthesis of CuO NPs has been less likely studied. Thus, the barks of *A. muricata* was used to synthesize the CuO NPs, and their characterizations were studied. Table 2.4 depicts the summary of the utilization of different types of plants and precursor salts in the synthesis of CuO NPs with their characterizations from the first four literatures.

Table 2.4: Summary of the utilization of different types of plants and precursor salts in the synthesis of CuO NPs and their characterizations.

Type of plant	Plant part	Precursor salt	Absorption peak (nm)	Band gap energy (eV)	Morphology	Particle size (nm)	Crystal system	References
Muntingia calabura	Leaves	Copper(II) nitrate trihydrate	387	3.65	Rod shape	Length: 79-90 Thickness: 23	Monoclinic	(Selvanathan et al., 2021)
Pyrus pyrifolia	Leaves	Copper(II) nitrate hexahydrate	395	-	Spherical shape	17-30	Monoclinic	(Sundaramurthy and Parthiban, 2015)

Carica papaya L.	Peel	Copper(II) nitrate trihydrate	270	3.33	Agglomerated spherical shape	85-140	Monoclinic	(Phang et al., 2021)
Allium sativum	Bulb	Copper(II) nitrate	398	3.20	Spherical and oval-shaped	20-40	Monoclinic	(Velsankar et al., 2020)

CHAPTER 3

MATERIALS AND METHODOLOGY

3.1 Materials

The barks of *A. muricata* were collected from Ipoh, Perak, Malaysia. The precursor salt utilized in the synthesis of CuO NPs was $Cu(NO_3)_2 \cdot 3H_2O$ (Purity = 99%) with a molecular weight of 241.60 g/mol (CAS number = 10031-43-3). It was an analytical research (AR) grade and was stored in the drying cabinet due to its highly moisture-sensitive and hygroscopic properties. In addition, deionized water acted as a green solvent in this research and was used to clean the barks of *A. muricata* to remove the impurities present and act as the reaction medium for the synthesis process. In addition, Table 3.1 shows the details of the chemical reagents for the qualitative phytochemical test.

Table 3.1: List of reagents for phytochemical test.

Reagents	Molecular weight (g/mol)	CAS number	Brand	Grade
Aluminium chloride hexahydrate	241.45	7784-13-6	GENE Chemical	AR grade
Chloroform	119.38	67-66-3	Merck	AR grade

98% concentrated ammonia solution	17.03	1336-21-6	Merck	AR grade
Dragendorff's reagent	-	-	-	-
Glacial acetic acid	60.05	64-19-7	RCI Labscan	AR grade
Iron(III) chloride hexahydrate	270.33	10025-77-1	Merck	AR grade
Lead(II) acetate trihydrate	379.34	6080-56-4	QRëC	AR grade
Olive oil	-	-	-	-
Wagner's reagent	-	-	-	-
98% concentrated sulphuric acid	98.08	7664-93-9	Chemiz	AR grade

3.2 Equipment

Table 3.2 shows the details of the equipment used throughout this research.

Table 3.2: List of equipment and their functions.

Equipment	Function

Aluminium foil	Used to cover the reaction vessels to prevent contamination and minimize solvent evaporation during the plant extraction process.
Analytical balance	Provides precise measurement of precursor salt and barks of *A. muricata* powder to ensure accurate reactant quantities.
Beakers	Serve as reaction vessels for the plant extraction process and the mixing of *A. muricata* extract with copper precursor during synthesis.
Centrifuge	To separate the solid plant materials from the supernatant during the preparation of the plant extract.
Centrifuge tube	To collect the supernatant of *A. muricata* extract after the centrifugation process.
Ceramic crucible	Act as a stable container to hold the resulting paste for the calcination process.
Desiccator	Maintains a moisture-free environment to store the synthesized CuO NPs for further characterization.
Dropper	To allow precise controlled addition of small volumes of reagents in phytochemical tests and precursor solution into the plant extract during the synthesis process.
Freeze dryer	To remove the water from *A. muricata* extract by sublimation.

Furnace	Provides controlled heating for the calcination process of the resulting paste into CuO NPs.
Grinder	To reduce the dried barks of *A. muricata* into fine powder.
Magnetic stirrer	Ensures uniform mixing of the mixture during the synthesis of CuO NPs.
Magnetic stirring hot plate	Combining stirring and controlled heating to maintain reaction temperature and homogeneity.
Measuring cylinder	To measure precise volumes of liquids such as deionized water and *A. muricata* extract.
Micro sample tubes	To store the synthesized CuO NPs for further characterization.
Mortar and pestle	To grind the synthesized CuO NPs, precursor salts, and freeze-dried solid *A. muricata* extract with KBr salts evenly for characterization.
Oven	To dry the barks of *A. muricata* to remove moisture.
Retort stand and clamp	To support the thermometer in a fixed position to monitor temperature changes.
Ultrasonic bath sonicator	Promoting the dispersion of synthesized CuO NPs in the deionized water for characterization.
Spatula	To transfer the barks of *A. muricata* powder and precursor salts during weighing and sample preparation.
Test tubes	Serve as reaction vessels for phytochemical tests.

Thermometer	To monitor temperature during the plant extraction and synthesis process.
Volumetric flasks	To prepare solutions of precise and accurate concentrations by accurately measuring and diluting liquids to a fixed volume.

3.3 Instrumentation

Table 3.3 indicates the details of the instruments used in this research.

Table 3.3: List of instruments and their functions.

Instrument	Brand / Model	Function
Ultraviolet-Visible Spectrophotometer (UV-Vis)	Thermo Fisher Scientific GENESYS 50 series	To identify the maximum absorption wavelength and band gap energy of the synthesized CuO NPs.
Fourier Transform-Infrared Spectrophotometer (FT-IR)	PerkinElmer Spectrum FX1	To identify the functional groups, present in the *A. muricata* extract, synthesized CuO NPs, and the precursor salt.
Field Emission Scanning Electron Microscope (FESEM)	JEOL JSM-6701F	To analyze the surface morphology, shape, and size

		distribution of the synthesized CuO NPs.
Energy Dispersive X-ray Spectrometer (EDX)	Oxford Instruments X-max 50 mm^2	To analyze the elemental composition and purity of the synthesized CuO NPs.
X-ray Diffractometer (XRD)	Shimadzu XRD 6000	To determine the crystalline structure and average crystallite size of the synthesized CuO NPs.

3.4 Overview of research methodology

The methodology in this research is divided into five parts, which are shown in Figure 3.1.

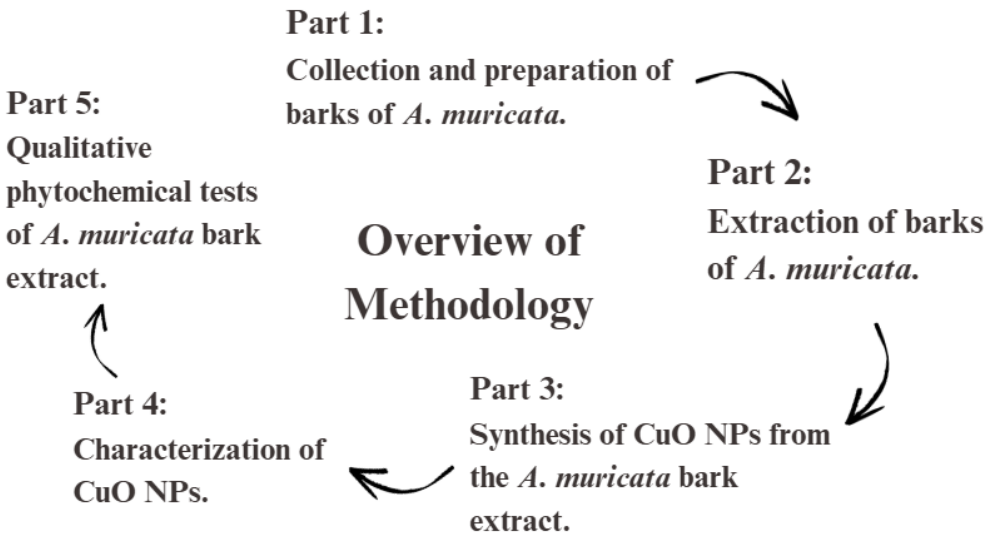

Figure 3.1: Overview of methodology.

3.5 Experimental procedure

3.5.1 Collection and preparation of barks of *A. muricata*

The barks of *A. muricata* were collected from Ipoh, Perak, Malaysia. After removing the leaves, the barks were washed with deionized water until all the contaminants, dirt, and soil were removed. Next, barks were cut into smaller sizes and dried in an oven at 40°C until the moisture was completely removed. The dried barks were ground into fine powder using a grinder and stored in a glass reagent bottle, and sealed with parafilm. This glass reagent bottle was then stored in a desiccator to prevent absorption of moisture. The flowchart is depicted in Figure 3.2.

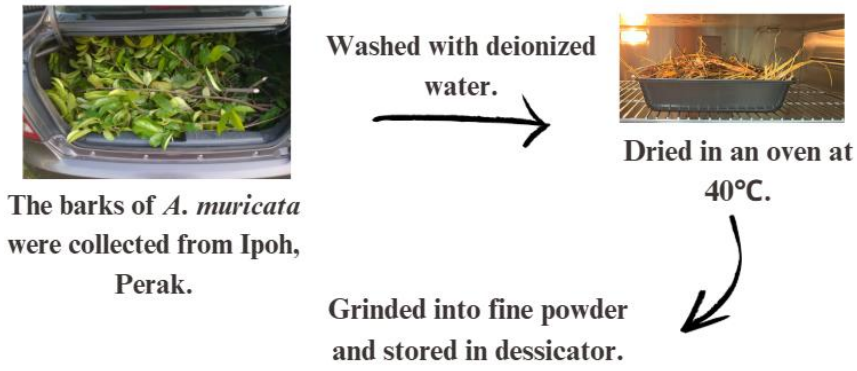

Figure 3.2: Flowchart of the collection and preparation of the barks of *A. muricata*.

3.5.2 Extraction of barks of *A. muricata*

In the preparation of *A. muricata* bark extract, a clean beaker was first placed on the analytical balance and tared to zero. Then, a spatula was used to carefully transfer the *A. muricata* powder into the beaker until 3 g was achieved. 100 mL of deionized water, which was measured using a measuring cylinder, was added to the beaker that contained weighed *A. muricata* powder. Next, the mixture was stirred continuously and heated at 80 - 90°C for 30 minutes on a magnetic stirring hot plate. After 30 minutes, the *A. muricata* extract was cooled to room temperature and centrifuged at a speed of 5000 rpm for 10 minutes to obtain the supernatant. The supernatant was then transferred into clean centrifuge tubes for future synthesis. Figure 3.3 illustrates the flow of this extraction process.

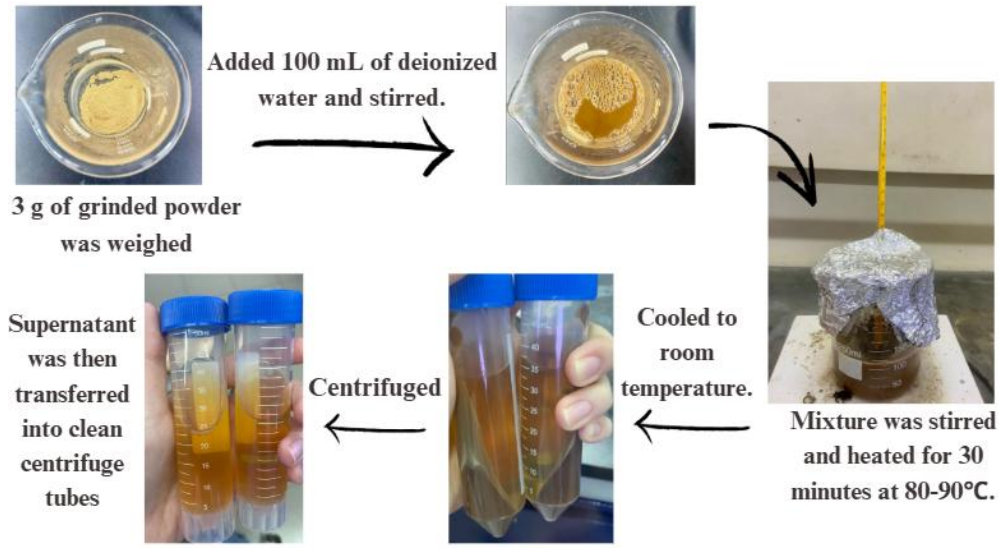

Figure 3.3: Flowchart of the extraction of the barks of *A. muricata*.

3.5.3 Green synthesis of CuO NPs

20 mL of *A. muricata* extract, which was measured using a measuring cylinder, was transferred to a clean beaker and heated to 80 - 90°C with constant stirring. Next, copper(II) nitrate solution was prepared by dissolving 2 g of $Cu(NO_3)_2 \cdot 3H_2O$ in 20 mL of deionized water. The copper(II) nitrate solution was then added dropwise to the preheated 20 mL of *A. muricata* extract under stirring. The mixture was continued to be heated with constant stirring until a paste was formed. The resultant paste was then transferred to a clean ceramic crucible and calcinated at 300°C for two hours in a furnace. The formation of black CuO powder was transferred to a micro-sample tube and stored in the desiccator for further characterization. The whole synthesis process was repeated with calcination temperatures of 400 and 500°C. The flow of synthesizing CuO NPs is depicted in Figure 3.4.

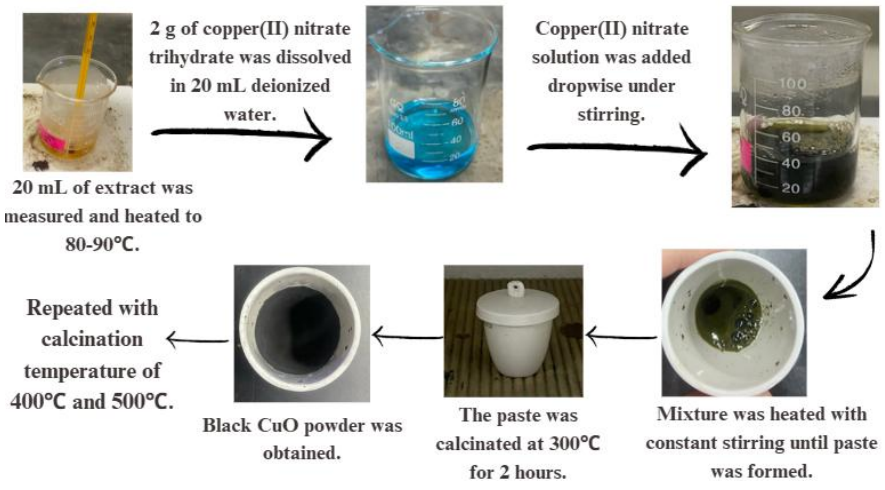

Figure 3.4: Flowchart of the CuO NPs synthesis.

3.5.4 Qualitative phytochemical test of *A. muricata* bark extract

The qualitative phytochemical screening of *A. muricata* bark extract was performed to identify the presence of various bioactive secondary metabolites. The details for each phytochemical test are listed below:

Test for the presence of alkaloids

The presence of alkaloids in the A. muricata bark extract was confirmed using Wagner's and Dragendorff's reagent tests. For each test, 1 mL of the extract was mixed with 1 mL of the respective reagent in a test tube and thoroughly mixed. The formation of a reddish-brown precipitate upon the addition of Wagner's reagent and the appearance of a reddish-orange precipitate upon the addition of Dragendorff's reagent serve as a positive indication.

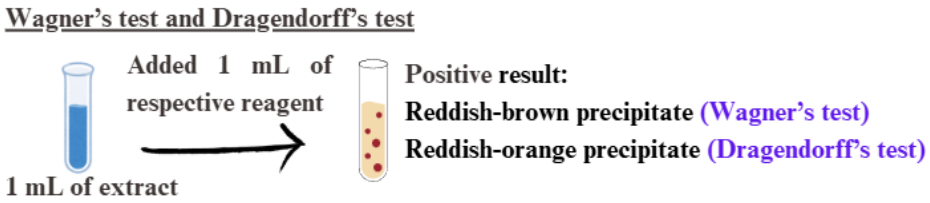

Figure 3.5: Methodology of the test for the presence of alkaloids.

Test for the presence of flavonoids

The presence of flavonoids in the *A. muricata* bark extract was qualitatively confirmed using two standard chemical tests: the ammonium test and the aluminium chloride test. For each test, 4 mL of the extract was mixed with 1 mL

of the respective reagent and shaken thoroughly. The formation of a yellow color in both tests is a positive indication of flavonoids.

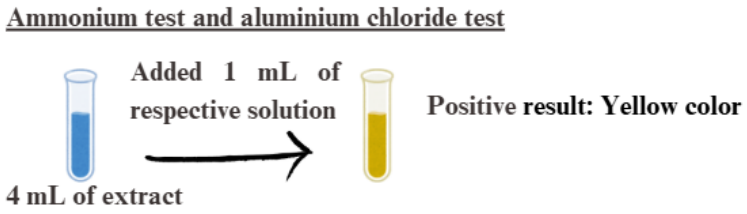

Figure 3.6: Methodology of the test for the presence of flavonoids.

Test for the presence of terpenoids

The presence of terpenoids in the *A. muricata* bark extract was assessed using Salkowski's test. First, 5 mL of extract was mixed with 2 mL of chloroform, followed by the addition of a few drops of concentrated sulphuric acid along the side of the test tube. The formation of reddish-brown precipitate at the interface served as a positive indication for the presence of terpenoids in the extract.

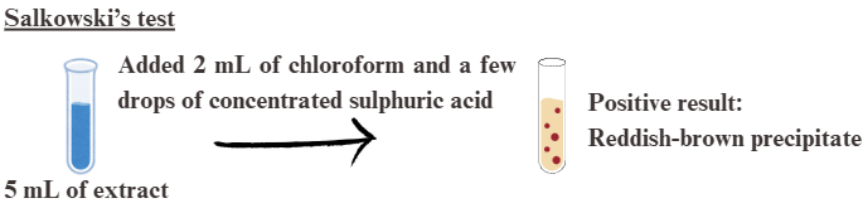

Figure 3.7: Methodology of the test for the presence of terpenoids.

Test for the presence of saponins

Saponins were detected by mixing 10 mL of the extract with 5 mL of distilled water, followed by vigorous shaking. The formation of a persistent froth indicated the presence of saponins. To further confirm this, 3 drops of olive oil were added to the froth, and the mixture was shaken vigorously again. The formation of an emulsion upon shaking confirmed the presence of saponins.

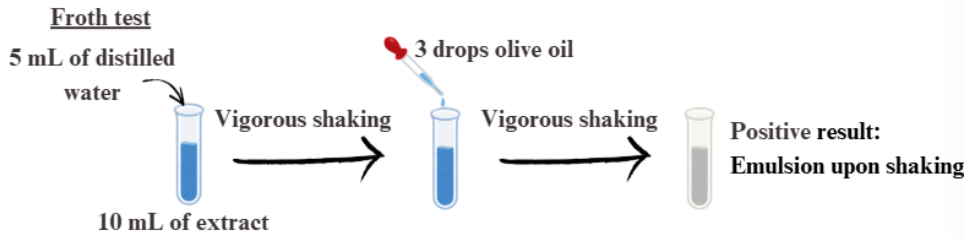

Figure 3.8: Methodology of the test for the presence of saponins.

Test for the presence of tannins

The presence of tannins was assessed using two complementary tests, which are the iron(III) chloride test and the lead(II) acetate test. In each test, 3 mL of extract was treated with a few drops of the respective solutions. The development of a greenish-black precipitate upon the addition of iron(III) chloride solution and the appearance of a cream-colored precipitate upon the addition of lead(II) acetate solution indicated the presence of tannins.

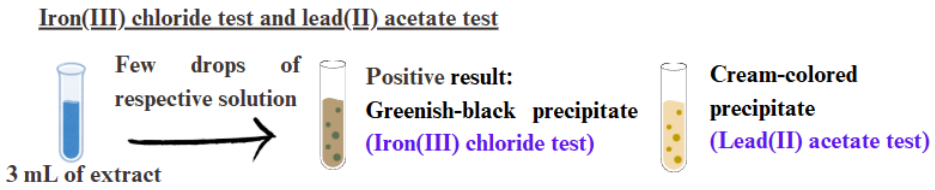

Figure 3.9: Methodology of the test for the presence of tannins.

Test for the presence of cardiac glycosides

The presence of cardiac glycosides in the *A. muricata* bark extract was detected using the Keller-Killiani test. First, 5 mL of extract was mixed with 2 mL of glacial acetic acid containing one drop of iron(III) chloride solution. The mixture was carefully underlayered with 1 mL of concentrated sulphuric acid by allowing the acid to flow gently along the side of the test tube to form two layers. The formation of a brown ring at the interface between the two layers shows a positive indication of cardiac glycosides. Additionally, a violet ring may appear just below the brown ring.

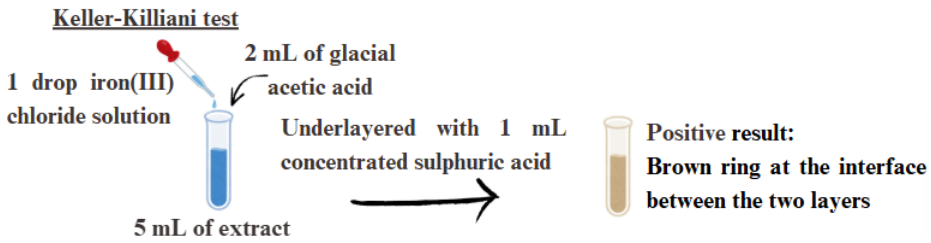

Figure 3.10: Methodology of the test for the presence of cardiac glycosides.

3.6 Characterization of synthesized CuO NPs

The synthesized CuO NPs were characterized using Ultraviolet-Visible Spectroscopy (UV-Vis), Fourier Transform-Infrared Spectroscopy (FT-IR), Field

Emission Scanning Electron Microscopy (FESEM), Energy Dispersive X-ray Spectroscopy (EDX), and X-ray Diffraction (XRD).

3.6.1 Ultraviolet-Visible Spectroscopy (UV-Vis)

A Thermo Fisher Scientific GENESYS 50 series of Ultraviolet-Visible Spectrophotometer (UV-Vis), which was illustrated in Figure 3.11, was used to confirm the formation of CuO NPs by detecting their characteristic absorption peak (λ_{max}), which arises from electronic transitions related to the CuO NPs band gap (E_g). Around 2 mg of the synthesized CuO NPs were weighed and added to a beaker that contained 10 mL of deionized water. The resulting sample solution was then sonicated for 15 minutes to promote dispersion of synthesized CuO NPs in the deionized water. The solution was then scanned over the wavelength range from 200 – 1000 nm.

Figure 3.11: Thermo Fischer Scientific GENESYS 50 series of UV-Vis spectrophotometer.

After the maximum absorption peaks were obtained, they were used to calculate the band gap energy of the synthesized CuO NPs by using Equation 3.2. The calculated values were then converted to electron volts (eV) by multiplying with $1.60218\times10^{-19,}$ as 1 eV equals $1.60218\text{x}10^{-19}$ J.

$$\text{Band gap energy, } E_g = \frac{hc}{\lambda} \text{ ---------- Equation 3.2}$$

Where,

h = Planck's constant (6.626×10^{-34} Js)

c = Speed of light (3.00×10^{8} ms^{-1})

λ = Maximum absorption wavelength (nm)

3.6.2 Fourier Transform-Infrared Spectroscopy (FT-IR)

The Fourier Transform-Infrared Spectrophotometer (FT-IR) with the model of PerkinElmer Spectrum FX1, as depicted in Figure 3.12, was utilized to identify the functional groups present in the *A. muricata* bark extract, precursor salt, and synthesized CuO NPs. The freeze-drying technique was used to obtain the solid *A. muricata* extract by removing the moisture through sublimation. Next, each solid sample was mixed evenly with dry KBr powder in a ratio of 1:10 (solid sample: KBr), respectively, using a mortar and pestle, and the solid sample was then scanned from 4000 – 400 cm^{-1}.

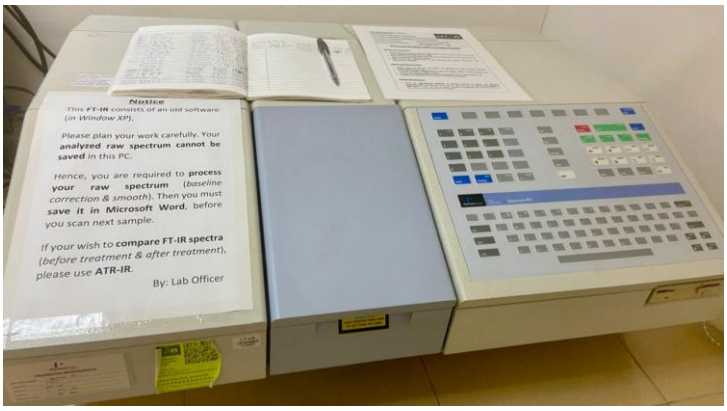

Figure 3.12: PerkinElmer Spectrum FX1 model of FT-IR spectrophotometer.

3.6.3 Field Emission Scanning Electron Microscopy (FESEM) and Energy Dispersive X-ray Spectroscopy (EDX)

The surface morphology, shape, and size distribution of synthesized CuO NPs were examined using a JEOL JSM-6701F model of Field Emission Scanning Electron Microscope (FESEM). In addition, an Energy Dispersive X-ray (EDX) spectrometer with the model of Oxford Instruments X-Max 50 mm^2, which is coupled with the FESEM, was used to analyze the elemental composition of the synthesized CuO NPs. Both FESEM and EDX instruments are shown in Figure 3.13.

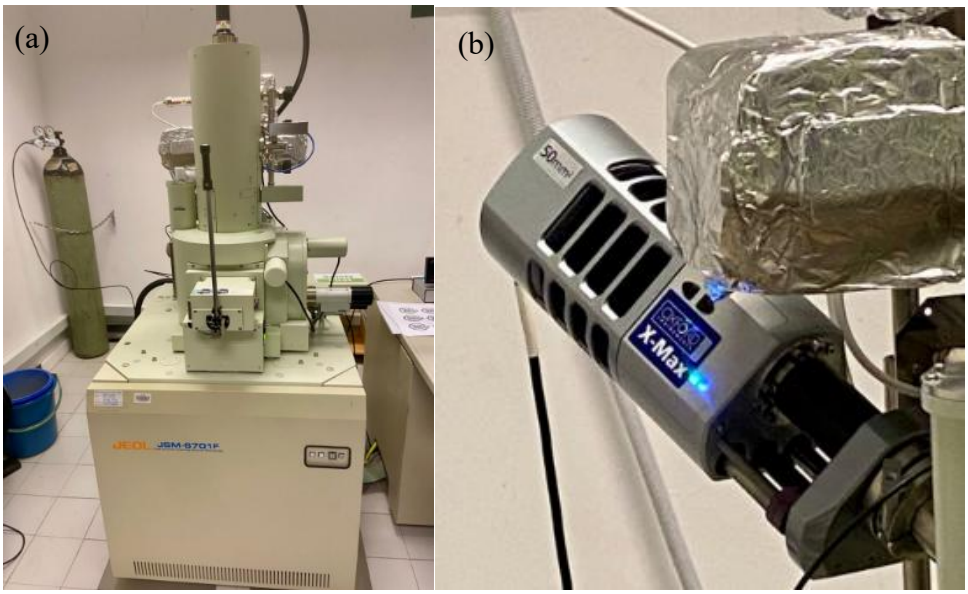

Figure 3.13: (a) JEOL JSM-6701F model of FESEM, and (b) Oxford Instruments X-Max 50 mm^2 model of EDX instruments.

3.6.4 X-ray Diffraction (XRD)

An X-ray Diffractometer, with the model of Shimadzu XRD 6000, as depicted in Figure 3.14, was used to determine the crystalline structure and average crystallite size of synthesized CuO NPs. In addition, the crystallite size of synthesized CuO NPs was determined through the Debye-Scherrer equation, as shown in Equation 3.3.

$$D = \frac{K\lambda}{\beta \cos\theta} \quad \text{--------- Equation 3.3}$$

Where,

D = Average crystalline size

K = Scherrer constant, 0.9

λ = Wavelength of the X-ray source, Cu Kα radiation = 1.5406 Å

β = Full width at half maximum (FWHM) of the diffraction peak in radian 2θ

θ = Bragg angle of diffraction in radians

Value of FWHM of the diffraction peak was determined using Equation 3.4.

$$\beta = \frac{FWHM\ in\ 2\theta\ x\ \pi}{180°}$$ ---------Equation 3.4

Figure 3.14: Shimadzu XRD 6000 model of X-ray Diffractometer.

CHAPTER 4

RESULTS AND DISCUSSION

4.1 Green Synthesis of CuO NPs

In this study, different calcination temperatures were employed as a key parameter to investigate their effect on structural, morphological, and physicochemical properties of the synthesized CuO NPs by using *A. muricata* bark extract and $Cu(NO_3)_2{\cdot}3H_2O$ as precursor salt. The purpose of choosing $Cu(NO_3)_2{\cdot}3H_2O$ was due to its ready dissociation to release Cu^{2+} ions into the reaction medium, which is essential for effective interaction with the phytochemicals present in the *A. muricata* bark extract. It also has good solubility and clean decomposition to CuO NPs with minimal impurities, facilitating the formation of uniform NPs with good crystallinity compared with other precursor salts, such as $CuCl_2$ and $Cu(CH_3COO)_2$ (Phiwdang et al., 2013; Abdullah, Guerrero, and Romero, 2024). Moreover, *A. muricata* was selected for the synthesis of CuO NPs primarily due to its rich content of bioactive phytochemicals such as alkaloids, flavonoids, tannins, and others, which serve as natural reducing, stabilizing, and capping agents (Selvanathan et al., 2022). *A. muricata* is also widely available in Malaysia.

During the preparation process, the collected *A. muricata* barks were washed with deionized water primarily to remove dirt, dust, microorganisms, and other surface impurities that could interfere with the extraction of bioactive

phytochemicals and affect the purity of the resulting NPs. The cleaned barks were then dried in an oven at a controlled low temperature of 40°C, which serves to gently remove moisture and prevent microbial growth while preserving the integrity and activity of the sensitive bioactive compounds. Next, the barks were ground into fine powder. In addition, the extraction solvent for phytochemicals from *A. muricata* bark used in this study is deionized water because it efficiently extracts a broad range of bioactive compounds in an eco-friendly and non-toxic manner. Deionized water is a polar solvent that facilitates the solubilization of these hydrophilic phytochemicals without introducing harmful chemicals. The extraction efficiency is also enhanced by increasing the extraction temperature to 80 - 90°C. This moderate heating accelerates the breakdown of cell walls and increases the diffusion rate of phytochemicals from the plant matrix.

The synthesis of CuO NPs by adding $Cu(NO_3)_2{\cdot}3H_2O$ solution dropwise into the preheated bark extract proceeds through nucleation and growth processes. Initially, as the $Cu(NO_3)_2$ solution is introduced gradually into the preheated bark extract containing reducing and stabilizing phytochemicals, the dissociated Cu^{2+} ions interact with these bioactive compounds, which serve to chelate the ions and reduce them to a lower oxidation state. This initiates nucleation, where small copper or copper oxide nuclei form as seeds for NPs development (Thanh, Maclean, and Mahiddine, 2014). The system at this stage has a high energy state due to the presence of these tiny particles dispersed in the solution. As the synthesis continues, the NPs grow mainly through Ostwald ripening, a process where smaller, less stable particles dissolve and redeposit onto larger, more stable nuclei (Zhang et al., 2015). This growth reduces the total surface energy

of the system, progressively driving the reaction toward thermodynamic equilibrium (Bastús, Comenge and Puntes, 2011). The transformation of color of the solution from light blue to dark green hues as nucleation progresses. Next, the mixture was heated until a paste was formed, and the paste was calcinated at various temperatures. The equation for each mechanism step in the synthesis of CuO NPs is depicted in Table 4.1. The schematic diagram for the mechanism for the synthesis of CuO NPs is also shown in Figure 4.1.

Table 4.1: Equation for each mechanism step in the synthesis of CuO NPs (Merkel et al., 2010).

Reaction step	Chemical equation
Chelation of Cu^{2+} by plant extract compounds	Cu^{2+} + phytochemicals → Cu-phytochemical complex
Reduction of Cu^{2+} by plant extract compounds	Cu^{2+} + phytochemicals → Cu^{0} + oxidized phytochemicals
Oxidation of Cu^{0} in the presence of oxygen	$Cu^{0} + \frac{1}{2} O_2 \rightarrow CuO$
Thermal decomposition (Calcination)	Cu-phytochemical complex → CuO NPs + $CO_2 + H_2O$

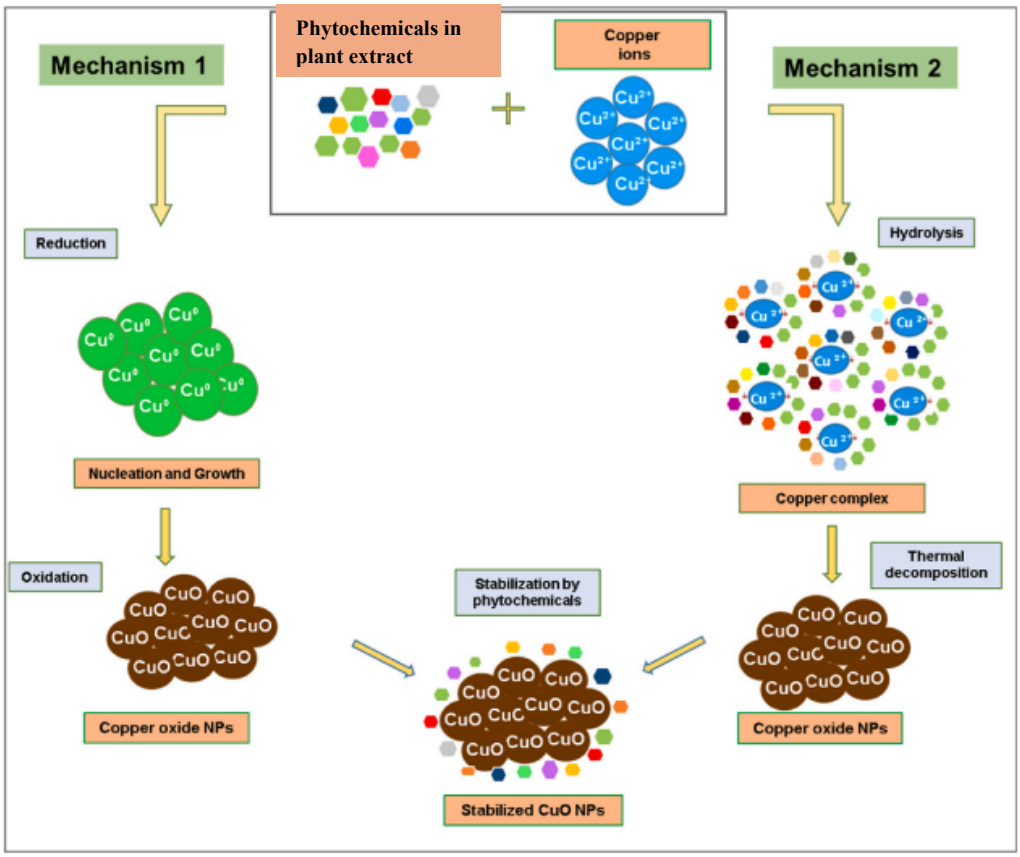

Figure 4.1: Two proposed mechanisms for the synthesis of CuO NPs by using plant extract (Jebali, Gómez-Merino, and Colangelo, 2024).

4.2 Qualitative phytochemical test of *A. muricata* bark extract

The qualitative phytochemical screening results are summarized in Table 4.2. In the ammonium test, the formation of a reddish-brown color results from the presence of other phytochemicals, such as tannins or oxidized phenolic compounds, which may visually overpower or obscure the lighter yellow color that indicates the presence of flavonoids in the *A. muricata* bark extract. As a result, an aluminium chloride test was performed to confirm the presence of flavonoids in the bark extract.

The extract tested positive for the presence of alkaloids, flavonoids, saponins, tannins, and cardiac glycosides. The positive identification of these bioactive molecules in this study aligns well with the established studies by Sudhashini et al. (2023) and Kazaure et al. (2025). The presence of these phytochemicals suggests that the *A. muricata* bark extract contains compounds capable of acting as natural reducing and stabilizing agents, which is beneficial for the green synthesis of CuO NPs. These bioactive components are known to facilitate the reduction of Cu^{2+} ions and stabilize the formed CuO NPs, thereby enhancing the synthesis process.

Furthermore, this study demonstrated that the *A. muricata* bark extract lacked detectable terpenoids. This absence was primarily due to the lower concentration of terpenoids in woody tissues such as barks compared to leaves, fruits, and other plant parts.

Table 4.2: Qualitative phytochemical results of *A. muricata* bark extract.

Phytochemical compound	Test used	Pictures (Left: Plant extract, Right: After addition of reagent)	Observation	Result
Alkaloids	Wagner's test		Reddish-brown precipitate was observed.	(+)
	Dragendorff's test		An orange coloration was observed.	(+)
Flavonoids	Ammonium test	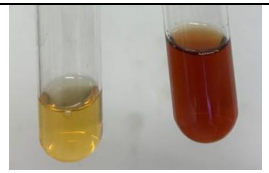	A reddish-brown coloration was observed.	(-)

Table 4.2 (continued): Qualitative phytochemical results of *A. muricata* bark extract.

Flavonoids	Aluminium chloride test		A yellow coloration was observed.	(+)
Terpenoids	Salkowski's test	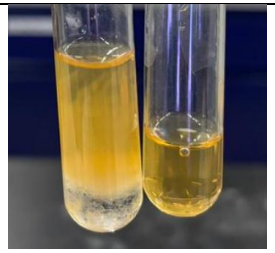	2 layers were separated, and no reddish-brown precipitate formed.	(-)
Saponins	Froth test		An emulsion was observed.	(+)

Table 4.2 (continued): Qualitative phytochemical results of *A. muricata* bark extract.

Tannins	Iron(III) chloride test	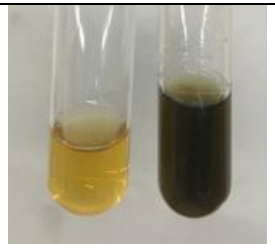	Greenish-black precipitate was observed.	(+)
	Lead(II) acetate test		Cream-colored precipitate was observed.	(+)
Cardiac glycosides	Keller-Killiani test	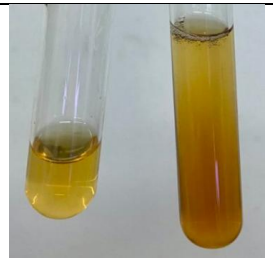	As the reagent was added too quickly and the two layers did not form, the characteristic brown ring at the interface could not be observed. However, a brown coloration was observed.	(+)

(+): Positive results (Present), (-): Negative results (Absent)

4.3 Characterization of synthesized CuO NPs

The synthesized black CuO NPs, which were calcinated at different temperatures, were characterized using Ultraviolet-Visible Spectroscopy (UV-Vis), Fourier Transform-Infrared Spectroscopy (FT-IR), Field Emission Scanning Electron Microscopy (FESEM), Energy Dispersive X-ray Spectroscopy (EDX), and X-ray Diffraction (XRD).

4.3.1 Ultraviolet-Visible Spectroscopy (UV-Vis)

The UV-Vis results indicate distinct absorption peaks for both the *A. muricata* bark extract and the CuO NPs synthesized at different calcination temperatures, which can be interpreted in terms of electronic transitions and NPs properties such as band gap and particle size.

Based on Figure 4.2, the *A. muricata* bark extract exhibited characteristic absorption peaks at 221 and 279 nm, which are typically associated with $\pi \rightarrow \pi^*$ and $n \rightarrow \pi^*$ electronic transitions in aromatic and conjugated phytochemical compounds, respectively. These peaks confirm the presence of phytochemicals such as flavonoids, phenolics, and other bioactive molecules that play a crucial role as reducing and stabilizing agents in the green synthesis of CuO NPs (Sudhashini et al., 2023).

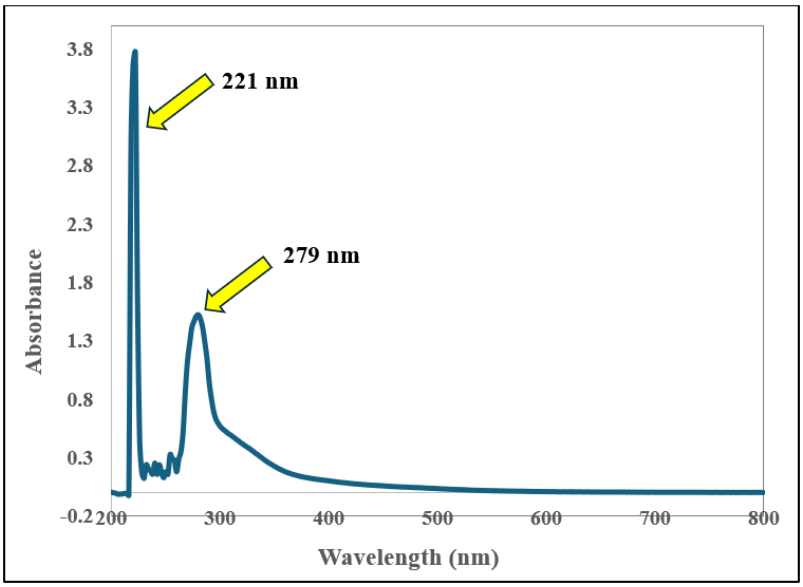

Figure 4.2: Absorption spectrum of *A. muricata* bark extract.

For the UV-Vis analysis of CuO NPs as depicted in Figure 4.3, the absorption maxima appeared at 368 nm for the CuO-300 and CuO-500 NPs, and at 370 nm for the CuO-400 NPs. The slight redshift to 370 nm in CuO-400 NPs suggests a subtle change in NPs characteristics, such as increased particle size and enhanced crystallinity, potentially reflecting an optimum calcination temperature for better crystallite growth and reduced defects. These absorption peaks are generally attributed to charge transfer transitions from the valence band to the conduction band within the CuO and correspond to the semiconductor band gap energy of NPs. The calculated E_g was 3.37 eV for both CuO-300 and CuO-500 NPs, and slightly lower at 3.35 eV for CuO-400 NPs. The slight reduction in E_g of CuO-400 NPs suggests improved crystallinity, which reduces quantum confinement compared to CuO-300 and CuO-500 NPs.

The E_g critically influences the semiconductor properties of CuO NPs. A larger E_g value typically results in higher energy required to excite electrons from the valence band to the conduction band, affecting both the optical absorption and electronic conductivity of the material. The higher E_g values observed in CuO-300 and CuO-500 NPs indicate strong quantum confinement that can enhance photocatalytic activity and photoresponse by tuning of electronic transitions (Dhineshbabu et al., 2015). Conversely, the slight decrease in E_g values in CuO-400 NPs implies better crystallinity and fewer surface defects, which can improve charge carrier mobility and reduce recombination rates, thus enhancing the semiconductor performance for applications such as sensors, photovoltaics, and photocatalysis (Dhineshbabu et al., 2015).

(a)

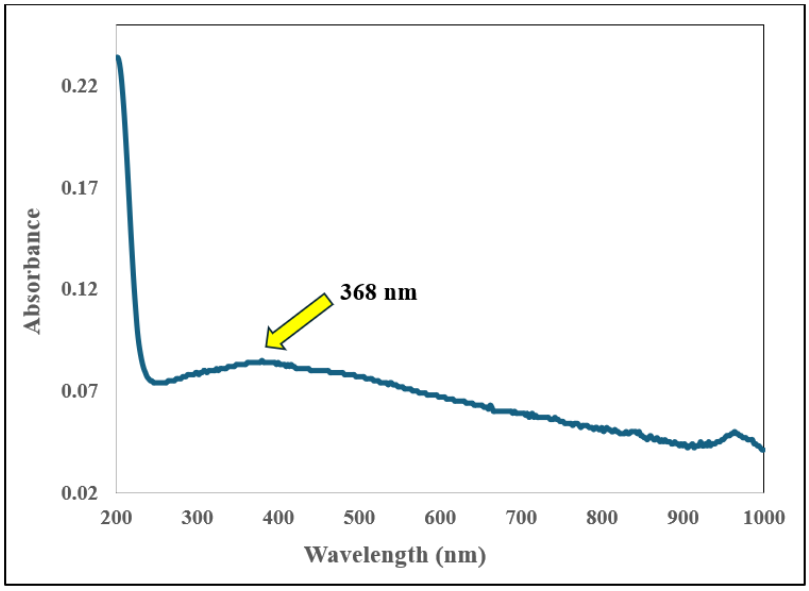

(b)

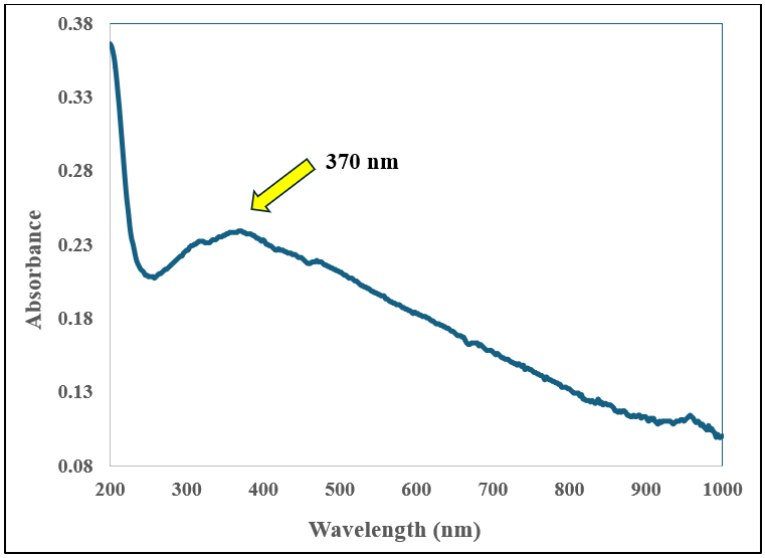

(c)

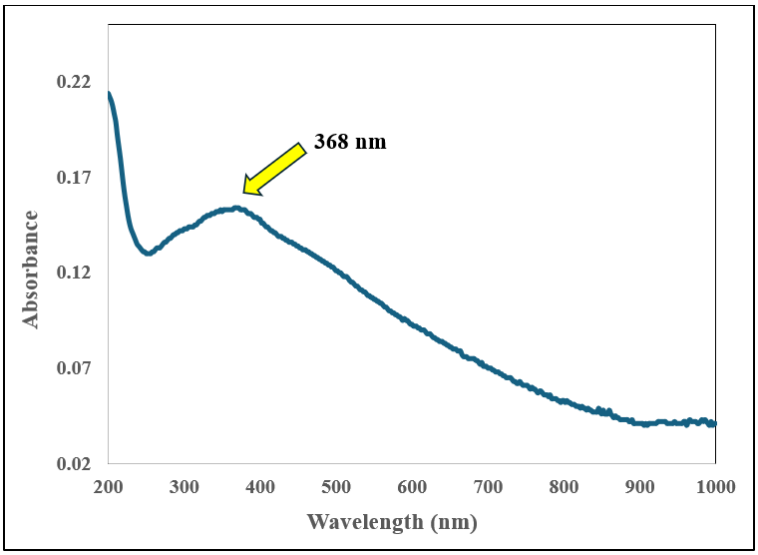

Figure 4.3: Absorption spectra of the synthesized (a) CuO-300, (b) CuO-400, and (c) CuO-500 NPs.

4.3.2 Fourier Transform-Infrared Spectroscopy (FT-IR)

The FT-IR analytical technique was used to characterize the functional groups present in the *A. muricata* bark extract, precursor salt, and the synthesized CuO-

300, CuO-400, and CuO-500 NPs. It was conducted over a wavenumber range of 4000 – 400 cm^{-1}.

According to the FT-IR spectra for the three CuO NPs samples as illustrated in Figure 4.4, the broad absorption bands at 3468, 3460, and 3439 cm^{-1} correspond to O-H stretching vibrations, due to the hygroscopic nature of KBr, which easily absorbs water vapor from the atmosphere during pellet preparation (Gordon et al., 2010). The small bands at 2360 and 2359 cm^{-1} are attributed to the stretching vibrations of CO_2 from the atmosphere trapped or absorbed on the sample surface. The absorption bands at 1636 and 1635 cm^{-1} are due to O-H bending vibrations from water molecules (El-Kemary, Nagy, and El-Mehasseb, 2013). The bands at 1111, 1110, and 1109 cm^{-1} can be assigned to C-N stretching vibrations, which are due to the phytochemicals that are involved in stabilizing the CuO NPs by capping their surfaces. Lastly, the distinct bands at 568, 552, and 545 cm^{-1} correspond to Cu-O stretching and confirm the formation of CuO NPs. Table 4.3 summarizes the FT-IR spectra of CuO NPs.

Based on the FT-IR spectrum of $Cu(NO_3)_2{\cdot}3H_2O$, as illustrated in Figure 4.5, the broad band at 3448 cm^{-1} represents the O-H stretching vibrations of the water molecules of trihydrate. This broadness typically arises from hydrogen bonding between the water molecules. The absorption bands at 1763 and 1384 cm^{-1} indicate C=O stretching and symmetric stretching vibrations of the nitrate ions, respectively (Padmaningrum et al., 2022). The band at 1616 cm^{-1} corresponds to the O-H bending vibrations of water molecules coordinated in the structure. The

band at 825 cm^{-1} represents the nitrate bending modes, while bands at 677 and 533 cm^{-1} represent the Cu-O vibrations. Table 4.3 summarizes the FT-IR spectrum of this precursor salt.

According to the FT-IR spectrum of *A. muricata* bark extract, as illustrated in Figure 4.6, the broad and strong band at 3419 cm^{-1} represents the O-H stretching vibrations, signifying the presence of phenols and alcohols. This is supported by the chemical structures of kaempferol, a flavonoid and tannin, depicted in Figure 4.7(a) and (b), which contain multiple hydroxyl groups responsible for this absorption band. The bands at 2940 cm^{-1} are attributed to C-H stretching vibrations of aliphatic groups, reflecting the presence of hydrocarbon chains. A weak band at 2083 cm^{-1} is related to alkyne groups. The prominent band at 1618 cm^{-1} corresponds to C=O stretching, likely from flavonoids, tannins, and other polyphenolic compounds. The absorption band at 1384 cm^{-1} is assigned to the asymmetric stretching of nitrate ions, possibly due to residual nitrates from environmental sources. The band at 1248 cm^{-1} is indicative of C-O stretching vibrations typical of glycosides, as exemplified by the chemical structure of a typical cardiac glycoside shown in Figure 4.7(c). Additionally, the absorption band at 1067 cm^{-1} suggests C-N stretching associated with an alkaloid, as depicted in Figure 4.7(d). In addition, the bands at 817, 772, and 617 cm^{-1} correspond to aromatic C-H bending vibrations, providing evidence of substituted aromatic rings characteristic of many secondary metabolites.

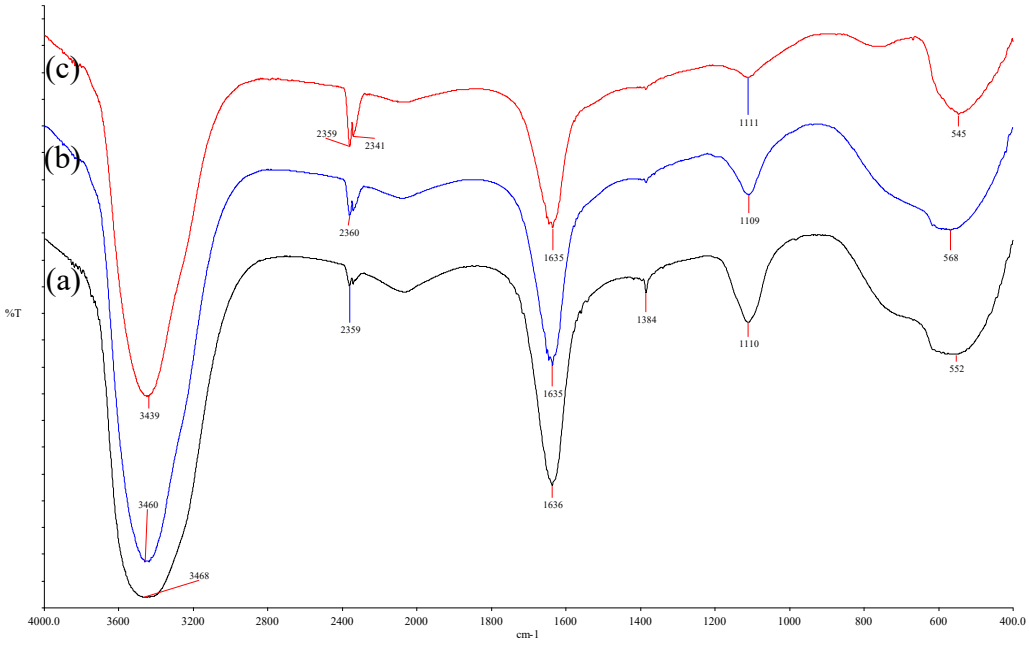

Figure 4.4: FT-IR spectra for the (a) CuO-300, (b) CuO-400, and (c) CuO-500 NPs.

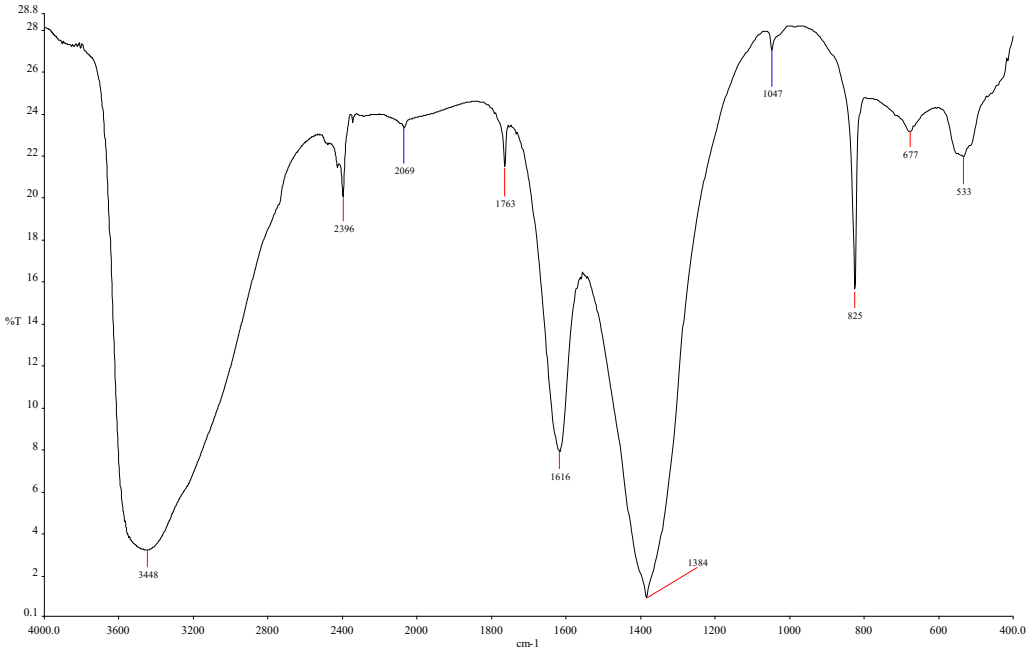

Figure 4.5: FT-IR spectrum for the $Cu(NO_3)_2{\cdot}3H_2O$.

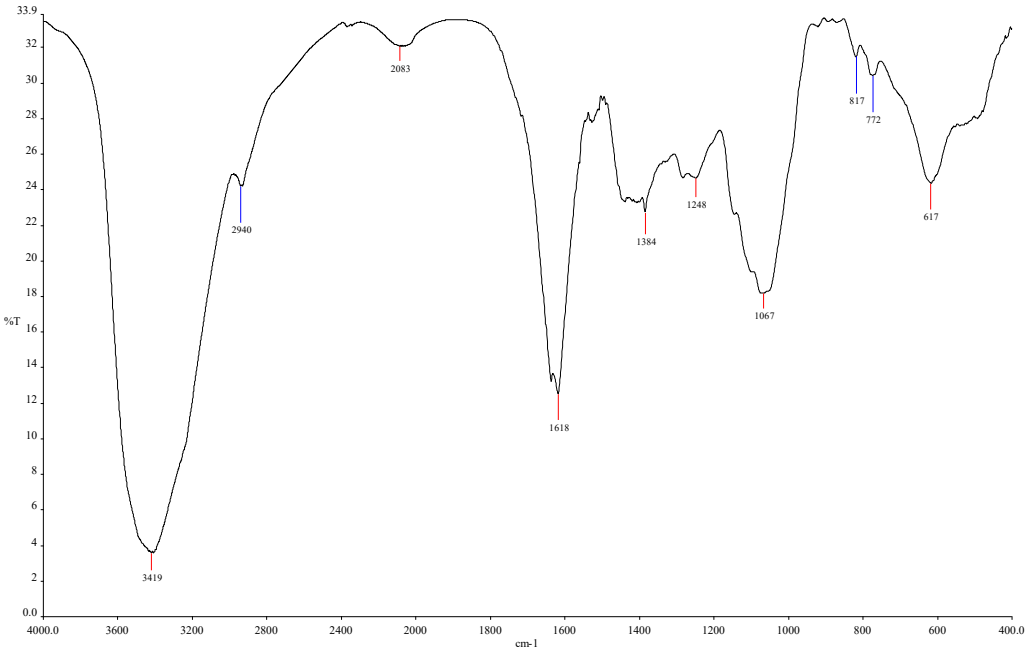

Figure 4.6: FT-IR spectrum for the *A. muricata* bark extract.

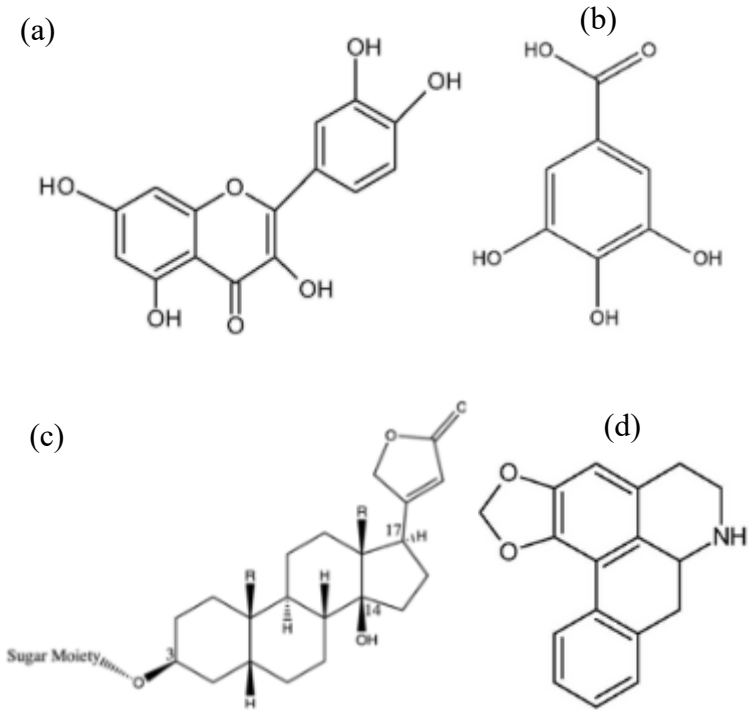

Figure 4.7: Structures of (a) flavonoid, (b) tannin, (c) cardiac glycosides, and (d) alkaloid (Coria-Téllez et al., 2018).

Table 4.3: Summary of FT-IR spectra of *A. muricata* bark extract, $Cu(NO_3)_2{\cdot}3H_2O$, CuO-300, CuO-400, and CuO-500 NPs.

	Wavenumber (cm^{-1})				
	Bark extract	**[$Cu(NO_3)_2{\cdot}3H_2O$]**	**CuO-300**	**CuO-400**	**CuO-500**
***ν*(O-H)**	3419	3448	3468	3460	3439
***ν*(C-H)**	2940	-	-	-	-
***ν*(CO_2)**	-	2396 2069	2359	2360	2359 2341
***ν*(C≡C)**	2083	-	-	-	-
***ν*(C=O)**	1618	1763	-	-	-
δ(O-H)	-	1616	1636	1635	1635
***ν*(NO_3^-)**	1384 (as)	1384 (as)	1384 (as)	-	-

Table 4.3 (continued): Summary of FT-IR spectra of *A. muricata* bark extract, $Cu(NO_3)_2 \cdot 3H_2O$, CuO-300, CuO-400, and CuO-500 NPs.

***v*(C-O)**	1248	-	-	-	-
***v*(C-N)**	1067	-	1110	1109	1111
δ(NO_3^-)	-	825	-	-	-
δ(C-H)	817 772 617	-	-	-	-
***v*(Cu-O)**	-	1047 677 533	552	568	545

4.3.3 Field Emission Scanning Electron Microscopy (FESEM)

FESEM operates by directing a focused beam of electrons onto the surface of CuO NPs, which are synthesized at various calcination temperatures. The electron beam interacts with the atoms to produce various signals, such as secondary and backscattered electrons. These signals will be collected by the detector and generate detailed, three-dimensional-like images that reveal shape, degree of agglomeration, dimension, and particle size.

According to Figures 4.8 - 4.10, the synthesized CuO NPs at various calcination temperatures exhibit an irregular but more defined spherical morphology, and the range of particle size obtained for CuO-300, CuO-400, and CuO-500 NPs were 28.1 – 36.4 nm, 27.7 – 33.5 nm, and 27.3 – 34.5 nm, respectively. The range of particle size of CuO-400 NPs is slightly narrower compared to CuO-300 and CuO-500 NPs, indicating a more uniform and controlled NPs growth. In addition, the synthesized CuO NPs also show noticeable moderate agglomeration instead of being fully discrete particles. Agglomeration appears because NPs possess a very high surface energy due to their large surface-to-volume ratio, and to minimize this energy, particles tend to cluster together, thus leading to agglomeration (Chan et al., 2022). Agglomeration can be reduced by modifying the pH environment during the synthesis process to enhance the electrostatic repulsion, which is supported by the study from Valan et al. (2022). In addition, the large, irregular, square-shaped particles observed in Figure 4.5 are likely unreacted copper(II) nitrate precursors.

(a)

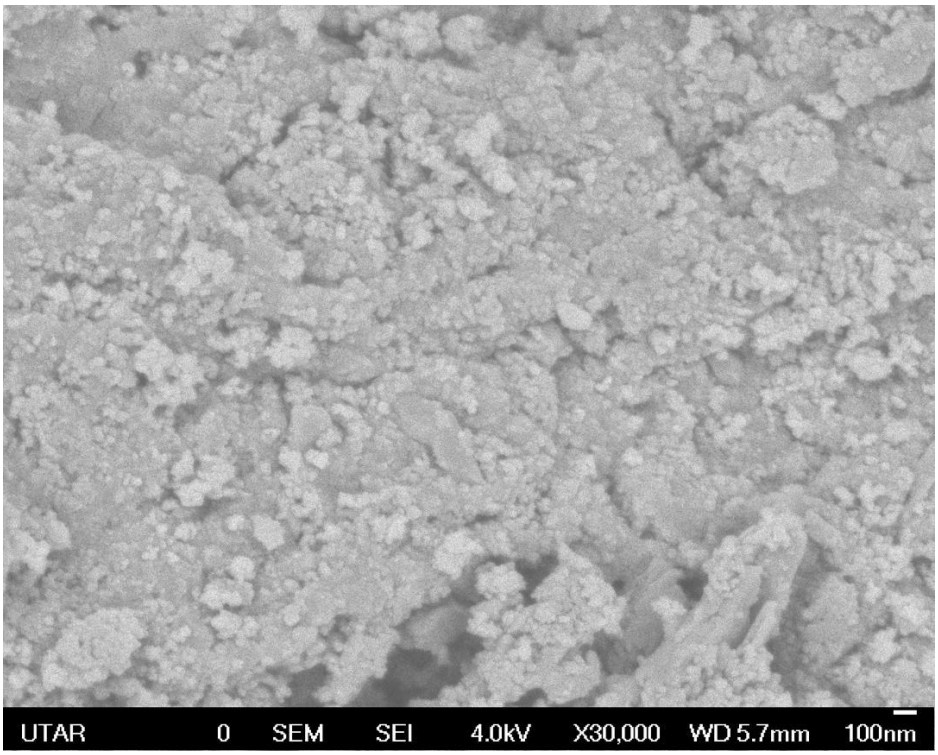

(b)

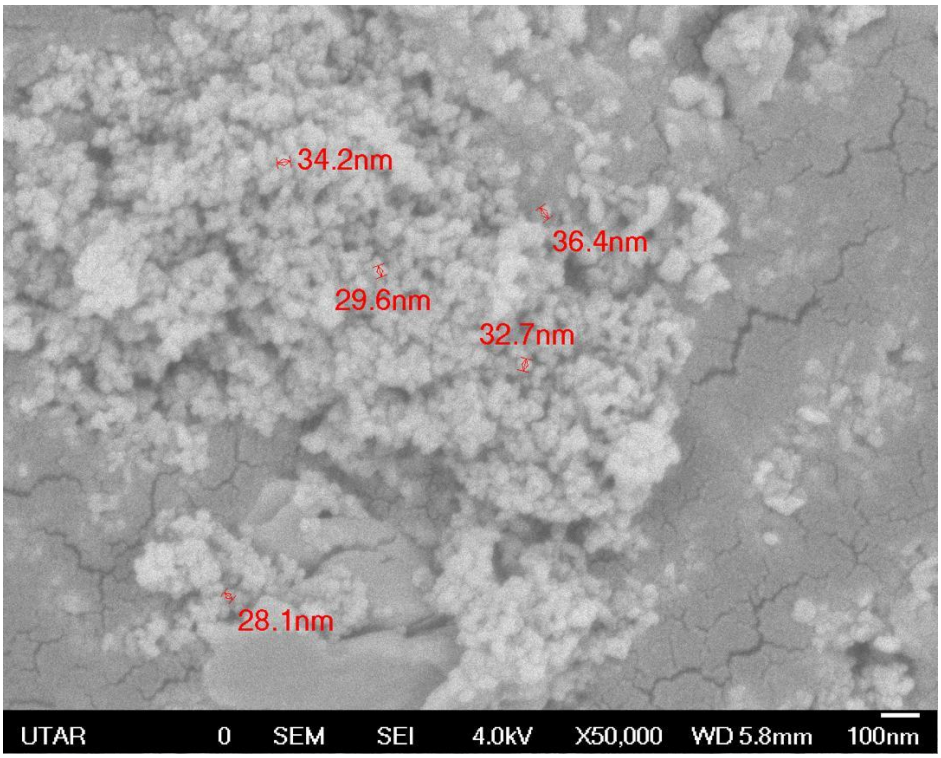

Figure 4.8: FESEM images of CuO-300 NPs at magnification of (a) 30000×, and (b) 50000×

(a)

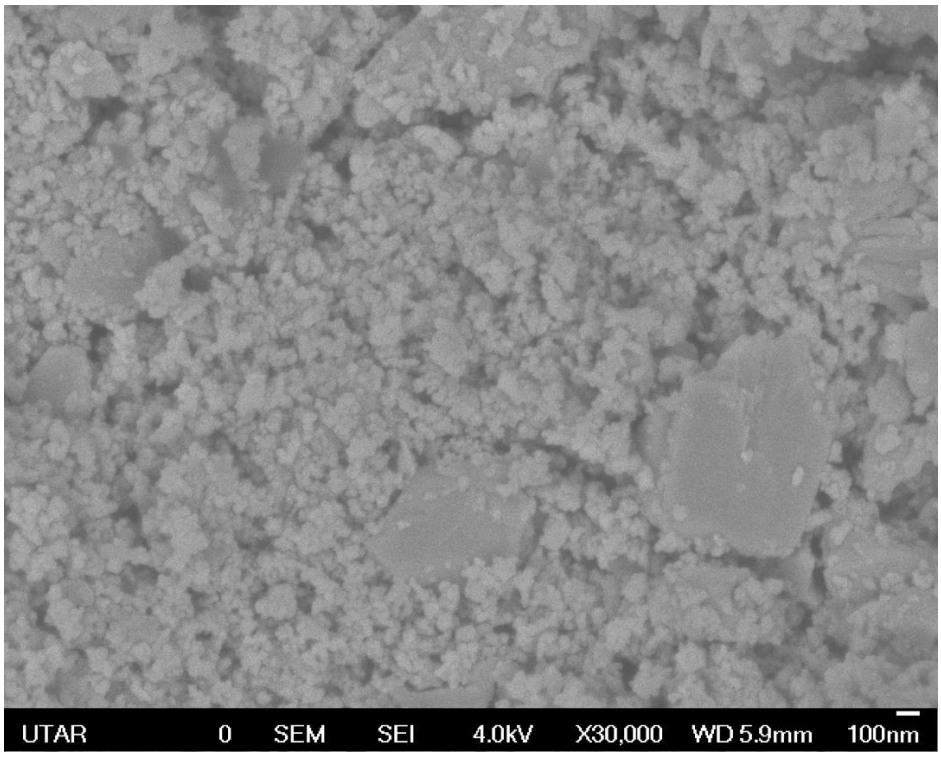

(b)

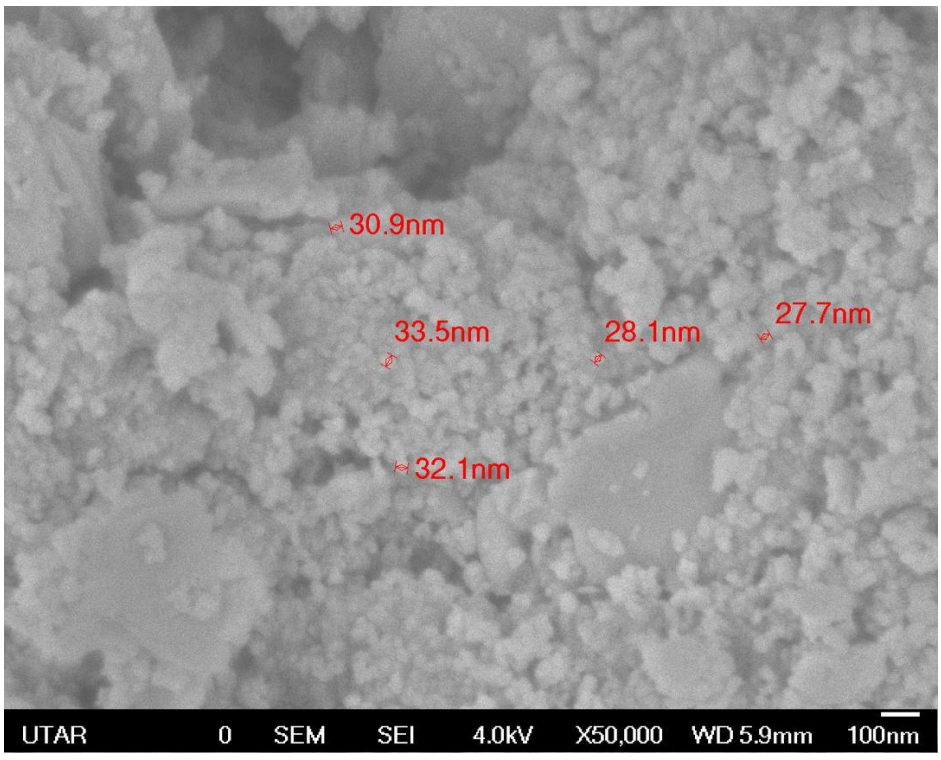

Figure 4.9: FESEM images of CuO-400 NPs at magnification of (a) 30000×, and (b) 50000×

(a)

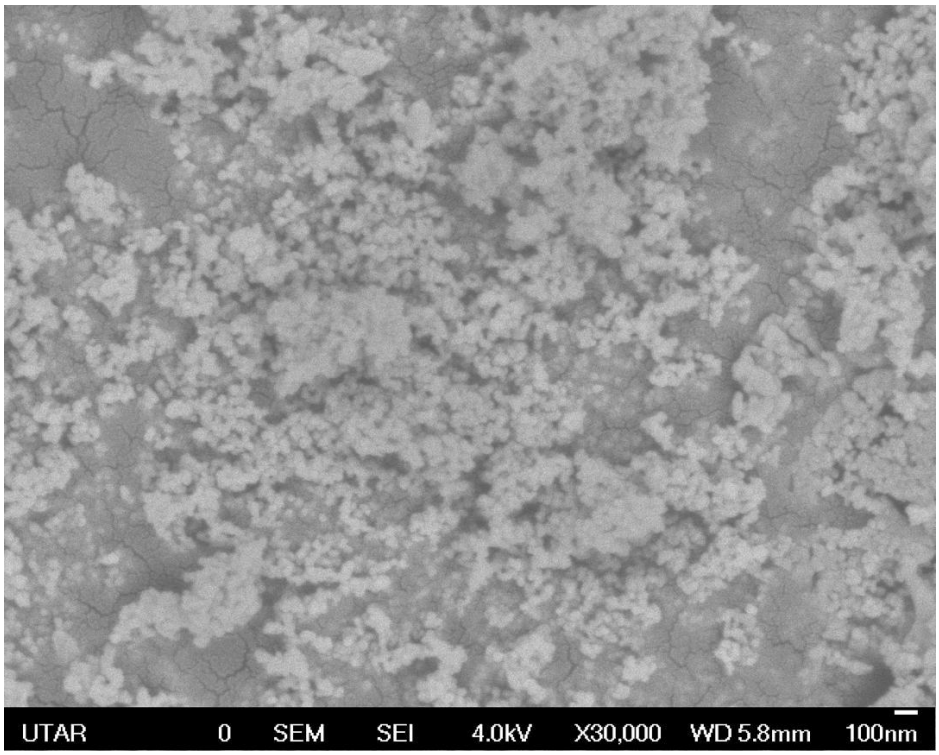

(b)

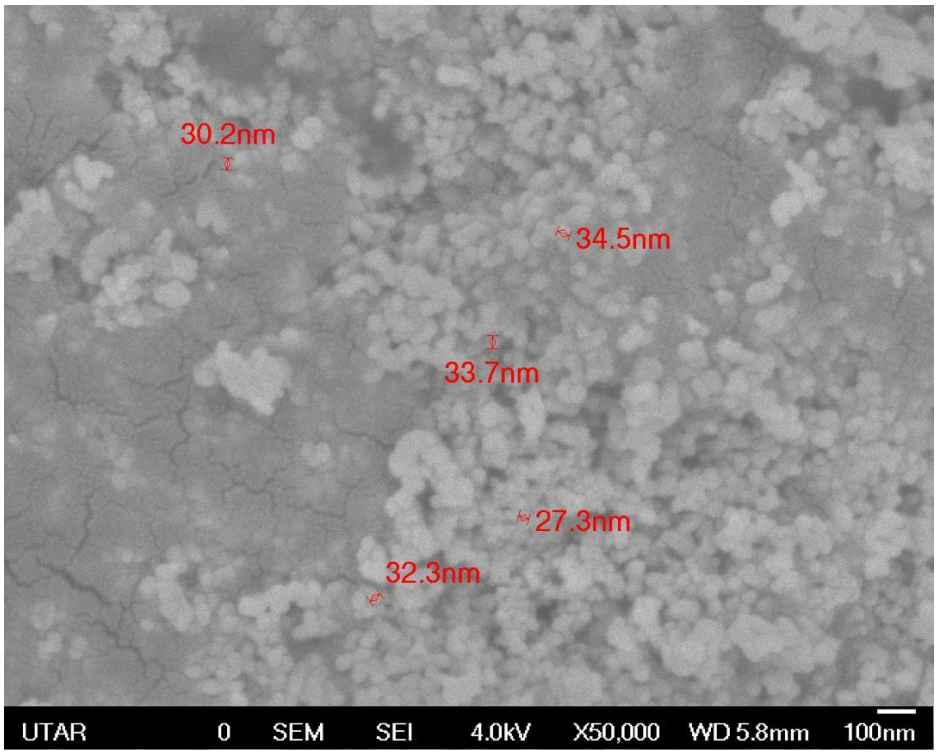

Figure 4.10: FESEM images of CuO-500 NPs at magnification of (a) 30000×, and (b) 50000×

4.3.4 Energy Dispersive X-ray Spectroscopy (EDX)

EDX typically works together with FESEM as a complementary technique. The same electron beam interacts with the atoms, knocking out inner-shell electrons (Nanakoudis, 2019). This creates vacancies in the inner electron shells and causes the electrons from outer shells to drop down to fill these vacancies (Nanakoudis, 2019). The energy will then be released in the form of X-rays. The detector will measure the energy and intensity of the X-rays, and the relative abundance of elements present in the sample will be identified.

Based on the EDX images (Figure 4.11), confirm that all the synthesized CuO NPs consist solely of Cu and O elements, with no impurities detected. For the CuO-300 NPs, the weight percentages of Cu and O elements were found to be 69.93% and 30.07%, respectively. Similarly, the CuO-400 NPs exhibited weight percentages of Cu and O elements at 70.20% and 29.80%, respectively. Lastly, for CuO-500 NPs, the weight percentages of Cu and O elements were found to be 78.68% and 21.32%, respectively. The information was summarized in Table 4.4.

Table 4.4: Weight and atomic percentages of the elements present in the synthesized CuO NPs from EDX analysis.

Sample	Element	Weight percent (%)	Atomic percent (%)
CuO-300	**Cu**	69.93	36.93
	O	30.07	63.07
	Total	100.00	100.00
CuO-400	**Cu**	70.20	37.23
	O	29.80	62.77
	Total	100.00	100.00
CuO-500	**Cu**	78.68	48.16
	O	21.32	51.84
	Total	100.00	100.00

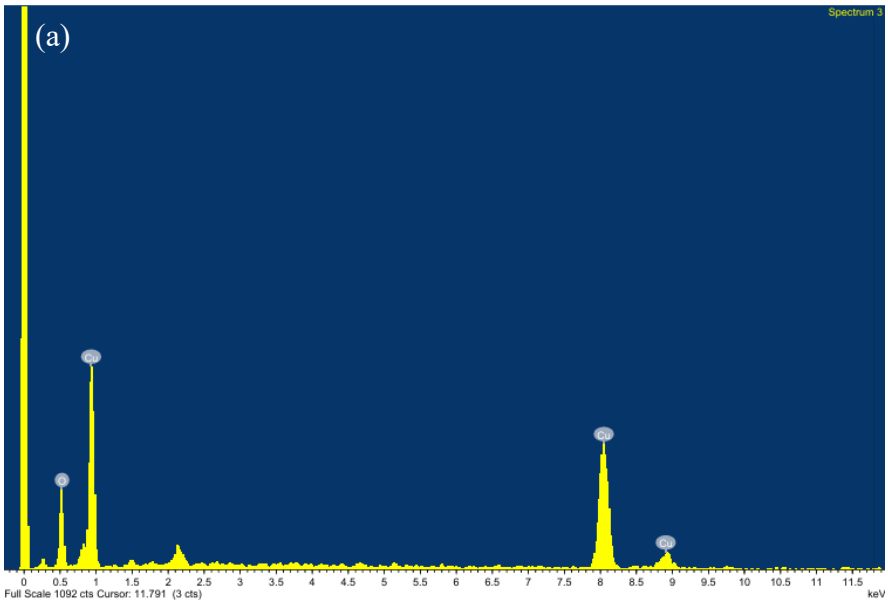

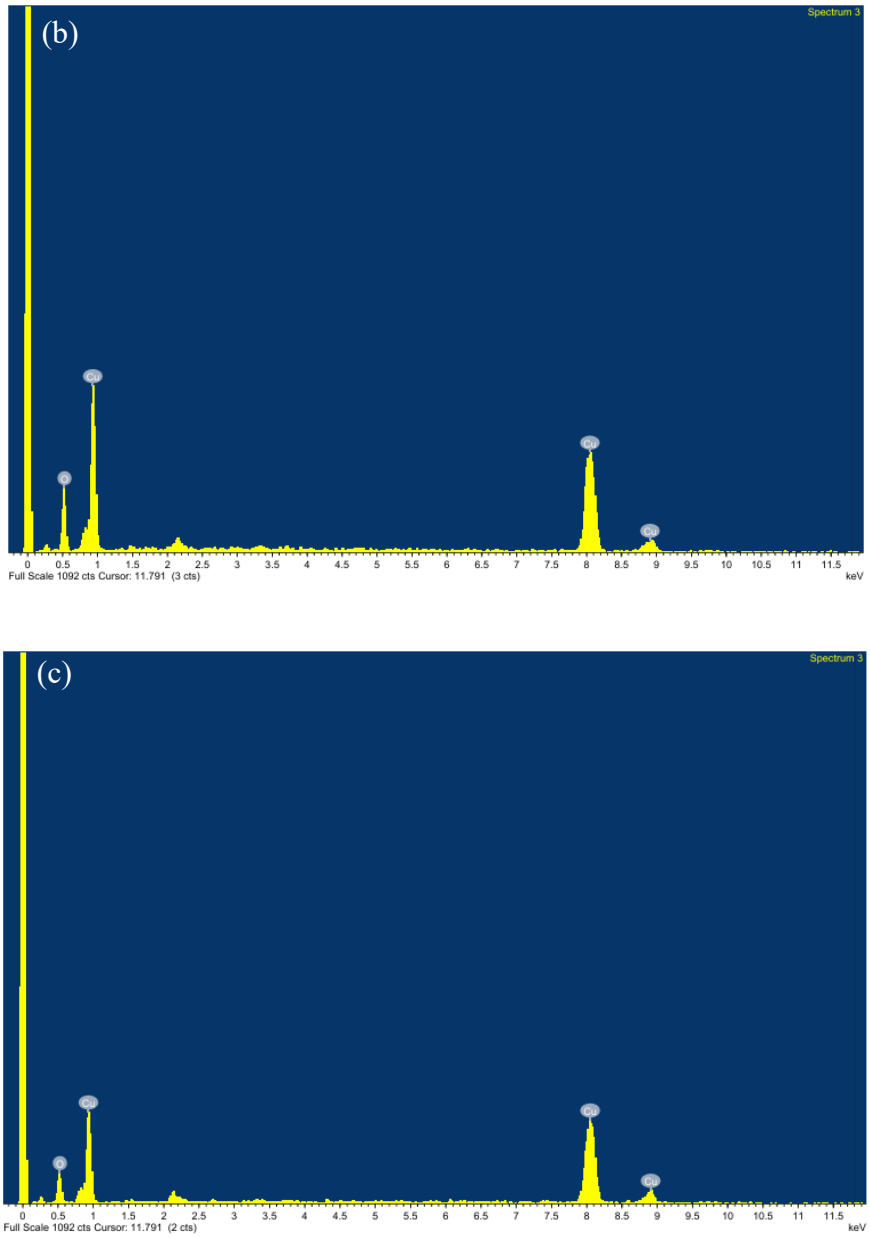

Figure 4.11: EDX spectra of (a) CuO-300, (b) CuO-400, and (c) CuO-500 NPs.

4.3.5 X-ray Diffraction (XRD)

XRD is a powerful, non-destructive technique extensively employed to analyze crystallographic structure and phase composition of NPs. This method relies on the diffraction of X-rays by the periodic atomic planes within crystalline NPs,

following Bragg's law, where constructive interference occurs at specific angles characteristic of the crystal lattice spacings (Chhantyal, 2022). By measuring the intensity of diffracted X-rays as a function of diffraction angle 2θ, an XRD pattern is produced that acts as a unique fingerprint for identifying crystalline phases present in the NPs. XRD not only confirms the formation and purity of crystalline phases but also provides quantitative estimates of crystallite size by evaluating the broadening of diffraction peaks through the Scherrer equation (Suhail, 2025). The peak positions are compared with standard diffraction data from recognized databases such as the ICDD Card to verify the phases present (Suhail, 2025).

Based on Figure 4.12, diffraction peaks observed at 2θ values of 32.51°, 35.53°, 38.72°, 48.74°, 53.40°, 58.28°, 61.52°, 65.85°, 66.26°, 67.88°, 72.41°, 75.03°, and 75.25° correspond to the crystal planes indexed as (1 1 0), (0 0 2), (2 0 0), (2 0 2), (0 2 0), (2 0 2), (1 1 3), (3 1 0), (3 1 1), (1 1 3), (3 1 1), (0 0 4), and (0 0 4), respectively. The diffraction peaks were 93.3% consistent with the ICDD Card No. 00-045-0937 as depicted in Appendix C. The synthesized CuO NPs exhibited a monoclinic crystal structure with lattice parameters of a = 4.6853 Å, b = 3.4257 Å, c = 5.1303 Å, and a unique interaxial angle β = 99.549°, consistent with the reported monoclinic CuO phase (space group C2/c). In addition, degree of crystallinity exhibited by CuO-300 NPs was 18.51% and 81.49% of amorphous content.

Figure 4.13 illustrates the XRD pattern of the synthesized CuO-400 NPs, showing prominent diffraction peaks at 2θ values of 32.37°, 35.40°, 38.58°, 46.17°, 48.67°, 53.32°, 58.13°, 61.38°, 65.66°, 66.14°, 67.74°, 72.26°, 74.88°, and 75.09°, which are indexed to the crystalline planes (1 1 0), (0 0 2), (2 0 0), (1 1 2), (2 0 2), (0 2 0), (2 0 2), (1 1 3), (3 1 0), (3 1 1), (1 1 3), (3 1 1), (0 0 4), and (0 0 4). These peak positions and corresponding planes show a 94.4% match with the ICDD Card No. 01-077-7717, confirming the monoclinic phase of CuO, as detailed in Appendix D. The refined lattice parameters of the synthesized CuO-400 NPs were determined as a = 4.6863 Å, b = 3.4276 Å, c = 5.1333 Å, and a unique interaxial angle β = 99.520°, consistent with the monoclinic crystal system (space group C2/c). Furthermore, degree of crystallinity assessed for CuO-400 NPs was 18.63%, with remaining 81.37% attributed to amorphous content.

Based on Figure 4.14, revealing distinct diffraction peaks at 2θ values of 32.53°, 35.55°, 38.73°, 46.27°, 48.84°, 53.41°, 58.28°, 61.53°, 66.27°, 68.13°, 72.40°, and 75.08°. These peaks correspond to crystal planes of (1 1 0), (0 0 2), (2 0 0), (1 1 2), (2 0 2), (0 2 0), (2 0 2), (1 1 3), (3 1 1), (1 1 3), (3 1 1), and (0 0 4), respectively. The diffraction data exhibited a 95.1% correlation with the monoclinic CuO phase as referenced in ICDD Card No. 00-005-0661 (refer to Appendix E). The refined lattice constants for the CuO NPs were found to be a = 4.6840 Å, b = 3.4250 Å, c = 5.1290 Å, and a unique interaxial angle β = 99.470°, agreeing with the monoclinic crystal symmetry of space group C2/c. Additionally, crystalline fraction of the CuO-500 NPs was evaluated at 18.90%, with remaining 81.10% comprising amorphous content.

The crystalline size of the synthesized CuO NPs was estimated from the XRD data using the Debye-Scherrer equation, as shown in Appendix B, which relates the broadening of diffraction peaks to the size of crystalline domains. The calculated crystalline sizes are shown in detail in Appendix B. The results revealed that the synthesized CuO-300, CuO-400, and CuO-500 NPs had crystalline sizes typically ranging between 15.81 – 51.77 nm, 16.94 – 43.19 nm, and 16.95 – 43.20 nm, respectively. The average crystalline sizes were also found to be 27.09 nm for CuO-300 NPs, 25.22 nm for CuO-400 NPs, and 25.14 nm for CuO-500 NPs.

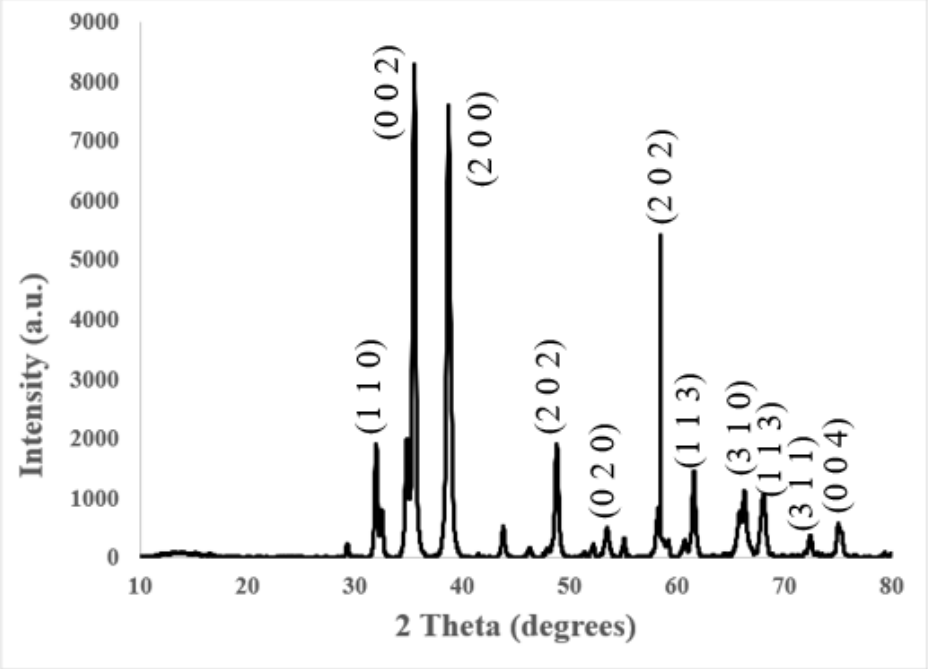

Figure 4.12: XRD diffractogram of the synthesized CuO-300 NPs.

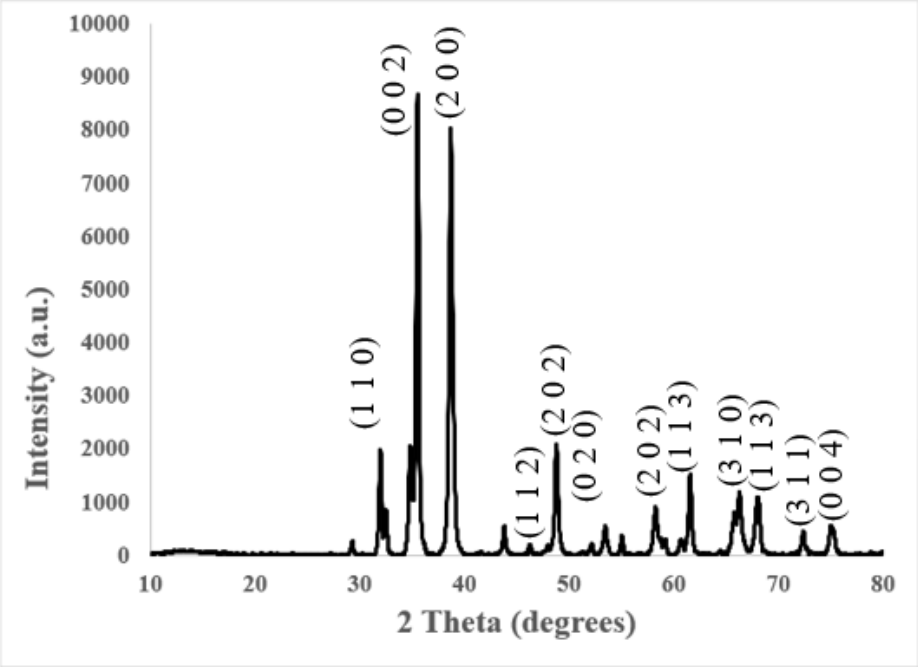

Figure 4.13: XRD diffractogram of the synthesized CuO-400 NPs.

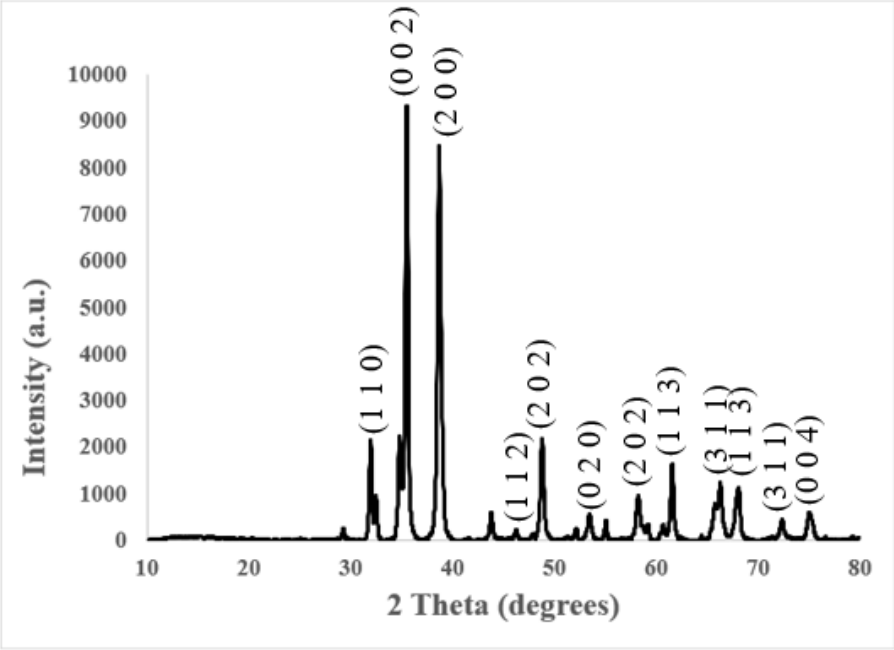

Figure 4.14: XRD diffractogram of the synthesized CuO-500 NPs.

CHAPTER 5

CONCLUSION

5.1 Conclusion

In this study, CuO NPs were successfully synthesized through a green synthesis approach using *A. muricata* bark extract. The biosynthesis leveraged natural phytochemicals as reducing and stabilizing agents, eliminating the need for hazardous chemicals. However, much research has focused only on CuO NPs synthesis; this work provides novel insights into the effects of the synthesis parameter of calcination temperatures on structural and optical properties. The synthesized CuO NPs were thoroughly characterized using techniques such as UV-Vis, FT-IR, FESEM, EDX, and XRD.

The CuO NPs synthesized at a calcination temperature of 300°C showed a maximum absorption peak at 368 nm, corresponding to a band gap energy of 3.37 eV. The FT-IR spectrum revealed prominent absorption bands at 552 cm^{-1}, characteristic of Cu-O stretching vibrations, confirming the formation of CuO NPs. In addition, it exhibited a spherical morphology with particle sizes ranging from 28.1 - 36.4 nm. It also exhibited a monoclinic structure and an average crystallite size of 27.09 nm.

The CuO NPs synthesized at a calcination temperature of 400°C revealed a maximum absorption peak at 370 nm, corresponding to a band gap energy of

3.35 eV. FT-IR analysis exhibited prominent absorption bands at 568 cm^{-1}, which are indicative of Cu-O bond stretching vibrations, further corroborating the successful formation of CuO NPs. Furthermore, it displayed a predominantly spherical morphology with particle sizes ranging from 27.7 - 33.5 nm. XRD analysis confirmed a monoclinic crystal structure, with the average crystallite size of 25.22 nm.

At a calcination temperature of 500°C, the synthesized CuO NPs revealed an absorption peak at 368 nm, corresponding to a band gap energy of 3.37 eV. The FT-IR spectrum exhibited a notable absorption band at 545 cm^{-1}, characteristic of Cu-O stretching vibrations, thus confirming the successful formation of CuO NPs. Additionally, it demonstrated a spherical morphology, with particle sizes ranging from 27.3 - 34.5 nm. XRD analysis confirmed the presence of a monoclinic crystal structure, and the average crystallite size was determined to be 25.14 nm.

5.2 Further studies

Further characterization of the CuO NPs can be performed using Raman spectroscopy, which provides valuable insights into the vibrational modes and crystal quality of the product. Transmission electron microscopy (TEM) is another essential technique that allows direct visualization of NPs morphology, size distribution, shape, and dispersion. TEM images offer high-resolution information that complements XRD data by revealing detailed surface structures and particle aggregation. Regarding potential applications, CuO NPs have

garnered interest for their photocatalytic properties, particularly in the degradation of organic dyes. Their high surface area and enhanced charge separation mechanisms make them effective catalysts for breaking down pollutants under light irradiation, demonstrating promising capabilities for environmental remediation.

REFERENCES

Abdullah, J.A.A., Guerrero, A. and Romero, A. (2024). Efficient and Sustainable Synthesis of Zinc Salt-Dependent Polycrystal Zinc Oxide Nanoparticles: Comprehensive Assessment of Physicochemical and Functional Properties. *Applied Sciences*, [online] 14(5), p.1815. doi:https://doi.org/10.3390/app14051815.

Adil, M., Deeba, F., Mumtaz, B., Abbas, M., Nimra Jabeen, S., Raza, H., Ali, R., Imtiaz, S., Saifuddin and Naseer, M. (2024). Synthesis Techniques and Applications of Diverse Nanoparticles. *International Journal of Veterinary Science*, (Nanotechnology-II), pp.254–260. doi:https://doi.org/10.47278/book.cam/2024.237.

Altammar, K.A. (2023). A review on nanoparticles: characteristics, synthesis, applications, and challenges. *Frontiers in Microbiology*, 14(1155622). doi:https://doi.org/10.3389/fmicb.2023.1155622.

Amin, F., Fozia, Khattak, B., Alotaibi, A., Qasim, M., Ahmad, I., Ullah, R., Bourhia, M., Gul, A., Zahoor, S. and Ahmad, R. (2021). Green Synthesis of Copper Oxide Nanoparticles Using Aerva javanica Leaf Extract and Their Characterization and Investigation of In Vitro Antimicrobial Potential and Cytotoxic Activities. *Evidence-Based Complementary and Alternative Medicine*, 2021, pp.1–12. doi:https://doi.org/10.1155/2021/5589703.

Anarado, C.E., Chukwubueze, F.M., Anarado, C.J.O., Umedum, N.L. and Nwanya, C.B. (2020). Comparative Phytochemical and in vitro Antioxidant Screening of the Root and Stem Bark of Annona muricata Linn. *International Research Journal of Pure and Applied Chemistry*, 21(8), pp.48–61. doi:https://doi.org/10.9734/irjpac/2020/v21i830189.

Ashish Avasthi, Caro, C., Pozo-Torres, E., Manuel Pernía Leal and María Luisa García-Martín (2020). Magnetic Nanoparticles as MRI Contrast Agents. *Topics in current chemistry collections*, pp.49–91. doi:https://doi.org/10.1007/978-3-030-55502-3_3.

BastúsN.G., Comenge, J. and PuntesV. (2011). Kinetically Controlled Seeded Growth Synthesis of Citrate-Stabilized Gold Nanoparticles of up to 200 nm: Size Focusing versus Ostwald Ripening. *Langmuir*, 27(17), pp.11098–11105. doi:https://doi.org/10.1021/la201938u.

Bayda, S., Adeel, M., Tuccinardi, T., Cordani, M. and Rizzolio, F. (2019). The History of Nanoscience and Nanotechnology: From Chemical–Physical Applications to Nanomedicine. *Molecules*, [online] 25(1), p.112. doi:https://doi.org/10.3390/molecules25010112.

Bhardwaj, A.K., Sundaram, S., Yadav, K.K. and Srivastav, A.L. (2021). An overview of silver nano-particles as promising materials for water disinfection. *Environmental Technology & Innovation*, 23, p.101721. doi:https://doi.org/10.1016/j.eti.2021.101721.

Carlos De Queiroz Pinto, A. (2025). *Annona muricata L.* [online] Available at: https://www.ipipotash.org/uploads/udocs/11_Soursop.pdf [Accessed 18 Jun. 2025].

Chan, Y., Selvanathan, V., Tey, L.-H., Akhtaruzzaman, Md., Anur, F., Djearamane, S., Watanabe, A. and Aminuzzaman, M. (2022). Effect of Calcination Temperature on Structural, Morphological and Optical Properties of Copper Oxide Nanostructures Derived from Garcinia mangostana L. Leaf Extract. *Nanomaterials*, 12(20), p.3589. doi:https://doi.org/10.3390/nano12203589.

Chauhan, M. (2025). *Garlic (Allium sativum): Health Benefits, Ayurvedic Uses, Dosage*. [online] Planet Ayurveda. Available at: https://www.planetayurveda.com/library/garlic-allium-sativum-health-benefits-ayurvedic-uses-dosage/ [Accessed 24 Jun. 2025].

Coria-Téllez, A.V., Montalvo-Gónzalez, E., Yahia, E.M. and Obledo-Vázquez, E.N. (2018). Annona muricata: A comprehensive review on its traditional medicinal uses, phytochemicals, pharmacological activities, mechanisms of action and toxicity. *Arabian Journal of Chemistry*, [online] 11(5), pp.662–691. doi:https://doi.org/10.1016/j.arabjc.2016.01.004.

Cuong, H.N., Pansambal, S., Ghotekar, S., Oza, R., Thanh Hai, N.T., Viet, N.M. and Nguyen, V.-H. (2022). New frontiers in the plant extract mediated biosynthesis of copper oxide (CuO) nanoparticles and their potential applications: A review. *Environmental Research*, 203, p.111858. doi:https://doi.org/10.1016/j.envres.2021.111858.

Ecosostenibile (2024). *Muntingia calabura: Systematics, Etymology, Habitat, Cultivation*. [online] An Eco-sustainable World. Available at: https://antropocene.it/en/2024/01/06/muntingia-calabura-2/ [Accessed 22 Jun. 2025].

Eker, F., Duman, H., Akdaşçi, E., Bolat, E., Sarıtaş, S., Karav, S. and Witkowska, A.M. (2024). A Comprehensive Review of Nanoparticles: From Classification to Application and Toxicity. *Molecules*, [online] 29(15), p.3482. doi:https://doi.org/10.3390/molecules29153482.

El-Kemary, M., Nagy, N. and El-Mehasseb, I. (2013). Nickel oxide nanoparticles: Synthesis and spectral studies of interactions with glucose. *Materials Science in Semiconductor Processing*, [online] 16(6), pp.1747–1752. doi:https://doi.org/10.1016/j.mssp.2013.05.018.

Fytianos, G., Rahdar, A. and Kyzas, G.Z. (2020). Nanomaterials in Cosmetics: Recent Updates. *Nanomaterials*, 10(5), p.979. doi:https://doi.org/10.3390/nano10050979.

Gavamukulya, Y., Wamunyokoli, F. and El-Shemy, H.A. (2017). Annona muricata: Is the natural therapy to most disease conditions including cancer growing in our backyard? A systematic review of its research history and future prospects. *Asian Pacific Journal of Tropical Medicine*, [online] 10(9), pp.835–848. doi:https://doi.org/10.1016/j.apjtm.2017.08.009.

Gordon, S.H., Mohamed, A.A., Harry-O'kuru, R.E. and Imam, S.H. (2010). A Chemometric Method for Correcting Fourier Transform Infrared Spectra of Biomaterials for Interference from Water in KBr Discs. *Applied Spectroscopy*, 64(4), pp.448–457. doi:https://doi.org/10.1366/000370210791114301.

Hafeezul, M. (2025). *Annona muricata*. [online] Malaysia Biodiversity Information System (MyBIS). Available at: https://www.mybis.gov.my/art/877 [Accessed 21 Jun. 2025].

Huston, M., DeBella, M., DiBella, M. and Gupta, A. (2021). Green Synthesis of Nanomaterials. *Nanomaterials*, 11(8), p.2130. doi:https://doi.org/10.3390/nano11082130.

Jebali, M., Gómez-Merino, A.I. and Colangelo, G. (2024). Influence of the lemon (Citrus Limon L.) juice amount on the green synthesis of CuO nanoparticles: Characterization, stability and thermal conductivity. *Ceramics International*. [online] doi:https://doi.org/10.1016/j.ceramint.2024.10.330.

Joudeh, N. and Linke, D. (2022). Nanoparticle classification, physicochemical properties, characterization, and applications: a comprehensive review for biologists. *Journal of Nanobiotechnology*, [online] 20(1). doi:https://doi.org/10.1186/s12951-022-01477-8.

Kazaure, A.A., Sani, A.M., Dan, V.M.Y. and Zahara (2025). Phytochemicals and antibacterial efficacy of *Annona muricata* (soursop) stem bark and leaf extracts against some clinical bacterial isolates. *Science World Journal*, [online] 20(1), pp.214–222. doi:https://doi.org/10.4314/swj.v20i1.28.

Khan, I., Saeed, K. and Khan, I. (2017). Nanoparticles: Properties, Applications and Toxicities. *Arabian Journal of Chemistry*, [online] 12(7), pp.908–931. doi:https://doi.org/10.1016/j.arabjc.2017.05.011.

Kiran, K. (2014). Gold nanoparticles for mercury determination in environmental water and vegetable samples. *Applied Nanoscience*, 5(3), pp.361–366. doi:https://doi.org/10.1007/s13204-014-0325-2.

Kumari, S. and Sarkar, L. (2021). A Review on Nanoparticles: Structure, Classification, Synthesis & Applications. *JOURNAL OF SCIENTIFIC RESEARCH*, 65(08), pp.42–46. doi:https://doi.org/10.37398/jsr.2021.650809.

Lu, P.-J., Huang, S.-C., Chen, Y.-P., Chiueh, L.-C. and Shih, D.Y.-C. (2015). Analysis of titanium dioxide and zinc oxide nanoparticles in cosmetics. *Journal of Food and Drug Analysis*, 23(3), pp.587–594. doi:https://doi.org/10.1016/j.jfda.2015.02.009.

Madeshwaran, K. and Venkatachalam, R. (2024). Green synthesis of bimetallic ZnO–CuO nanoparticles using Annona muricata l. extract: Investigation of antimicrobial, antioxidant, and anticancer properties. *Journal of Industrial and Engineering Chemistry*, 140, pp.454–467. doi:https://doi.org/10.1016/j.jiec.2024.06.002.

Mekuye, B. and Abera, B. (2023). Nanomaterials: An overview of synthesis, classification, characterization, and applications. *Nano select*, [online] 4(8). doi:https://doi.org/10.1002/nano.202300038.

Merkel, T.J., Herlihy, K.P., Nunes, J., Orgel, R.M., Rolland, J.P. and DeSimone, J.M. (2010). Scalable, Shape-Specific, Top-Down Fabrication Methods for the Synthesis of Engineered Colloidal Particles. *Langmuir*, 26(16), pp.13086–13096. doi:https://doi.org/10.1021/la903890h.

Mobarak, M.B., Sikder, M.F., Khandakar Sidratul Muntaha, Islam, S., S M Fazle Rabbi and Chowdhury, F. (2025). Plant extract-mediated green synthesized CuO nanoparticles for environmental and microbial remediation: A review covering basic understandings to mechanistic study. *Nanoscale Advances*. doi:https://doi.org/10.1039/d5na00035a.

Namakka, M., Rahman, Md.R., Said, K.A.M.B., Abdul Mannan, M. and Patwary, A.M. (2023). A review of nanoparticle synthesis methods, classifications, applications, and characterization. *Environmental Nanotechnology, Monitoring & Management*, [online] 20, p.100900. doi:https://doi.org/10.1016/j.enmm.2023.100900.

Nanakoudis, A. (2019). *EDX Analysis with SEM: How Does it Work?* [online] Advancing Materials. Available at: https://www.thermofisher.com/blog/materials/edx-analysis-with-sem-how-does-it-work/ [Accessed 10 Aug. 2025].

National Parks Board (2025). *Annona muricata*. [online] Available at: https://www.nparks.gov.sg/florafaunaweb/flora/3/2/3258 [Accessed 21 Jun. 2025].

NC State Extension (2025). *Pyrus pyrifolia (Apple Pear, Asian Pear, Chinese Pear, Chinese Sand Pear) | North Carolina Extension Gardener Plant Toolbox*. [online] plants.ces.ncsu.edu. Available at: https://plants.ces.ncsu.edu/plants/pyrus-pyrifolia/ [Accessed 22 Jun. 2025].

Neme, K., Nafady, A., Uddin, S. and Tola, Y.B. (2021). Application of nanotechnology in agriculture, postharvest loss reduction and food processing: food security implication and challenges. *Heliyon*, 7(12), p.e08539. doi:https://doi.org/10.1016/j.heliyon.2021.e08539.

Padmaningrum, R.T., Louise, I.S.Y., Yunita, I. and Sugiyarto, K.H. (2022). Infrared Spectral and Magnetic Properties of Basic Copper(II) Nitrate Produced by Slow Titration Method. *Malaysian Journal of Science*, 41(1), pp.106–116. doi:https://doi.org/10.22452/mjs.vol41no1.7.

Phang, Y.-K., Aminuzzaman, M., Akhtaruzzaman, Md., Muhammad, G., Ogawa, S., Watanabe, A. and Tey, L.-H. (2021). Green Synthesis and Characterization of CuO Nanoparticles Derived from Papaya Peel Extract for the Photocatalytic Degradation of Palm Oil Mill Effluent (POME). *Sustainability*, 13(2), p.796. doi:https://doi.org/10.3390/su13020796.

Phiwdang, K., Suphankij, S., Mekprasart, W. and Pecharapa, W. (2013). Synthesis of CuO Nanoparticles by Precipitation Method Using Different Precursors. *Energy Procedia*, 34, pp.740–745. doi:https://doi.org/10.1016/j.egypro.2013.06.808.

Piyush (2023). *Basics of Nanotechnology, Application, Advantage, Challenges*. [online] Study IQ. Available at: https://www.studyiq.com/articles/basics-of-nanotechnology/ [Accessed 16 Jun. 2025].

Sachdev, P. (2022). *Health Benefits of Soursop*. [online] WebMD. Available at: https://www.webmd.com/food-recipes/health-benefits-soursop [Accessed 21 Jun. 2025].

ScienceDirect (2018). Plant extract mediated synthesis of nanoparticles. *Emerging Applications of Nanoparticles and Architecture Nanostructures*, [online] pp.411–446. doi:https://doi.org/10.1016/B978-0-323-51254-1.00014-2.

ScienceDirect (2019). *Annona muricata - an overview | ScienceDirect Topics*. [online] www.sciencedirect.com. Available at: https://www.sciencedirect.com/topics/agricultural-and-biological-sciences/annona-muricata [Accessed 18 Jun. 2025].

Seed, S. (2022). *What to Know About Nanomedicine*. [online] WebMD. Available at: https://www.webmd.com/a-to-z-guides/nanomedicine-what-to-know [Accessed 29 Mar. 2025].

Selvanathan, V., Aminuzzaman, M., Tan, L.X., Win, Y.F., Guan Cheah, E.S., Heng, M.H., Tey, L.-H., Arullappan, S., Algethami, N., Alharthi, S.S., Sultana, S., Shahiduzzaman, M., Abdullah, H. and Aktharuzzaman, M. (2022). Synthesis, characterization, and preliminary in vitro antibacterial evaluation of ZnO nanoparticles derived from soursop (Annona muricata L.) leaf extract as a green reducing agent. *Journal of Materials Research and Technology*, 20, pp.2931–2941. doi:https://doi.org/10.1016/j.jmrt.2022.08.028.

Selvanathan, V., Aminuzzaman, M., Tey, L.-H., Razali, S.A., Althubeiti, K., Alkhammash, H.I., Guha, S.K., Ogawa, S., Watanabe, A., Shahiduzzaman, M. and Akhtaruzzaman, M. (2021). Muntingia calabura Leaves Mediated Green Synthesis of CuO Nanorods: Exploiting Phytochemicals for Unique Morphology. *Materials (Basel, Switzerland)*, [online] 14(21), p.6379. doi:https://doi.org/10.3390/ma14216379.

Singh, D., Singh, S., Sahu, J., Srivastava, S. and Singh, M.R. (2014). Ceramic nanoparticles: Recompense, cellular uptake and toxicity concerns. *Artificial Cells, Nanomedicine, and Biotechnology*, 44(1), pp.401–409. doi:https://doi.org/10.3109/21691401.2014.955106.

Solanki, J., Mandaliya, V.B. and Georrge John. J (2020). *Medicinal properties of Annona muricata Extracts in various disease*. [online] ResearchGate. doi:https://doi.org/10.6084/m9.figshare.13491129.

Sudhashini, S., Amudha, P., Vidya, R., Rani, V. and Kumar, R. (2023). *Journal of Advanced Zoology Phytochemical Screening and Profiling of Secondary Metabolites of Annona Muricata Bark*. [online] Available at: https://pdfs.semanticscholar.org/f7f4/beff823445f4fb1e5d4ae15d15a5382ca57a.pdf [Accessed 9 Aug. 2025].

Sundaramurthy, N. and Parthiban, C. (2015). *Biosynthesis of Copper Oxide Nanoparticles using Pyrus Pyrifolia Leaf Extract and Evolve the Catalytic Activity*. [online] *International Research Journal of Engineering and Technology*. IRJET. Available at: https://www.irjet.net/archives/V2/i6/IRJET-V2I658.pdf [Accessed 22 Jun. 2025].

Teleanu, D., Chircov, C., Grumezescu, A., Volceanov, A. and Teleanu, R. (2018). Impact of Nanoparticles on Brain Health: An Up to Date Overview. *Journal of Clinical Medicine*, 7(12), p.490. doi:https://doi.org/10.3390/jcm7120490.

Thanh, N.T.K., Maclean, N. and Mahiddine, S. (2014). Mechanisms of Nucleation and Growth of Nanoparticles in Solution. *Chemical Reviews*, [online] 114(15), pp.7610–7630. doi:https://doi.org/10.1021/cr400544s.

Tongi, J. (2023). Nanotechnology Principles and Applications for Innovative Material
Development. *Journal of Basic and Clinical Pharmacy*, [online] 14(3). Available at: https://www.jbclinpharm.org/articles/nanotechnology-principles-and-applications-for-innovative-materialdevelopment-12308.html [Accessed 16 Jun. 2025].

Tran, T.H. and Nguyen, V.T. (2014). Copper Oxide Nanomaterials Prepared by Solution Methods, Some Properties, and Potential Applications: A Brief Review. *International Scholarly Research Notices*, [online] 2014. doi:https://doi.org/10.1155/2014/856592.

Valan, S.L., Cruz, A.E.D., Jacob, P.J. and Djearamane, S. (2022). Sustainable Synthesis of Copper Oxide Nanoparticles Using Aquilaria Malaccensis (Agarwood) Leaf Extract as Reducing Agent. *International Journal of Technology*, 13(5), p.1115. doi:https://doi.org/10.14716/ijtech.v13i5.5845.

Velsankar, K., R.M., A.K., R., P., V., M. and Sudhahar, S. (2020). Green synthesis of CuO nanoparticles via Allium sativum extract and its characterizations on antimicrobial, antioxidant, antilarvicidal activities. *Journal of Environmental Chemical Engineering*, 8(5), p.104123. doi:https://doi.org/10.1016/j.jece.2020.104123.

Whiteker, G.T. (2019). Applications of the 12 Principles of Green Chemistry in the Crop Protection Industry. *Organic Process Research & Development*, 23(10), pp.2109–2121. doi:https://doi.org/10.1021/acs.oprd.9b00305.

Yang, K., Feng, L., Shi, X. and Liu, Z. (2013). Nano-graphene in biomedicine: theranostic applications. *Chem. Soc. Rev.*, 42(2), pp.530–547. doi:https://doi.org/10.1039/c2cs35342c.

Zahrah Alhalili (2023). Metal Oxides Nanoparticles: General Structural Description, Chemical, Physical, and Biological Synthesis Methods, Role in Pesticides and Heavy Metal Removal through Wastewater Treatment. *National Library of Medicine*, [online] 28(7), pp.3086–3086. doi:https://doi.org/10.3390/molecules28073086.

Zhang, Z., Wang, Z., He, S., Wang, C., Jin, M. and Yin, Y. (2015). Redox reaction induced Ostwald ripening for size- and shape-focusing of palladium nanocrystals. *Chemical Science*, 6(9), pp.5197–5203. doi:https://doi.org/10.1039/c5sc01787d.

Zubaidi, S.N., Mohd Nani, H., Ahmad Kamal, M.S., Abdul Qayyum, T., Maarof, S., Afzan, A., Mohmad Misnan, N., Hamezah, H.S., Baharum, S.N. and Mediani, A. (2023). Annona muricata: Comprehensive Review on the Ethnomedicinal, Phytochemistry, and Pharmacological Aspects Focusing on Antidiabetic Properties. *Life*, 13(2), p.353. doi:https://doi.org/10.3390/life13020353.

APPENDICES

Appendix A

Calculation for band gap energy, E_g:

Band gap energy, $E_g = \frac{hc}{\lambda}$

Where,

h = Planck's constant (6.626×10^{-34} Js)

c = Speed of light (3.00×10^{8} ms^{-1})

λ = Maximum absorption wavelength (368 and 370 nm)

Appendix B

Calculation for β for CuO-300 NPs:

$$\beta = \frac{FWHM\ in\ 2\theta\ x\ \pi}{180°}$$

$$= \frac{0.16\ x\ \pi}{180°}$$

$$= 2.79 \times 10^{-3} \text{ radians}$$

Calculation for crystalline size by using the Debye-Scherrer equation for CuO-300 NPs:

$$D = \frac{K\lambda}{\beta\ cos\theta}$$

$$= \frac{(0.9)(1.5406\ x\ 10^{-10} m)}{(2.79\ x\ 10^{-3}\ radians)(\cos 16.255°)}$$

$$= 5.177 \times 10^{-8} \text{ m}$$

$$= 51.77 \text{ nm}$$

A similar approach was applied to the rest of the matched peaks for CuO-300, CuO-400, and CuO-500 NPs to calculate their average crystallite sizes, which are summarizes in the table below:

Tables: Calculation of the average crystalline size for synthesized CuO-300, CuO-400, and CuO-500 NPs.

CuO-300 NPs					CuO-400 NPs				
2θ	**Miller's index**	**FWHM (°)**	**β (radians)**	**D (nm)**	**2θ**	**Miller's index**	**FWHM (°)**	**β (radians)**	**D (nm)**
32.51	(1 1 0)	0.16	0.00279	51.77	32.37	(1 1 0)	0.32	0.00559	25.83
35.53	(0 0 2)	0.32	0.00559	26.05	35.40	(0 0 2)	0.32	0.00559	26.05
38.72	(2 0 0)	0.36	0.00628	23.40	38.58	(2 0 0)	0.36	0.00628	23.39
48.74	(2 0 2)	0.36	0.00628	24.24	46.17	(1 1 2)	0.20	0.00349	43.19
53.40	(0 2 0)	0.28	0.00489	31.74	48.67	(2 0 2)	0.36	0.00628	24.23
58.28	(2 0 2)	0.40	0.00698	22.74	53.32	(0 2 0)	0.32	0.00559	27.75
61.52	(1 1 3)	0.28	0.00489	33.00	58.13	(2 0 2)	0.52	0.00908	17.47
65.85	(3 1 0)	0.48	0.00838	19.71	61.38	(1 1 3)	0.32	0.00559	28.84
66.26	(3 1 1)	0.60	0.01047	15.81	65.66	(3 1 0)	0.52	0.00908	18.17
67.88	(1 1 3)	0.32	0.00559	29.90	66.14	(3 1 1)	0.56	0.00977	16.94

72.41	(3 1 1)	0.40	0.00698	24.62	67.74	(1 1 3)	0.36	0.00628	26.59
75.03	(0 0 4)	0.32	0.00559	31.27	72.26	(3 1 1)	0.40	0.00698	24.59
75.25	(0 0 4)	0.56	0.00977	17.92	74.88	(0 0 4)	0.40	0.00698	25.02
-	-	-	-	-	75.09	(0 0 4)	0.40	0.00698	25.05
			Average	27.09				Average	25.22

CuO-500 NPs				
2θ	**Miller's index**	**FWHM (°)**	**β (radians)**	**D (nm)**
32.53	(1 1 0)	0.28	0.00489	29.54
35.55	(0 0 2)	0.32	0.00559	26.05
38.73	(2 0 0)	0.36	0.00628	23.40
46.27	(1 1 2)	0.20	0.00349	43.20
48.84	(2 0 2)	0.40	0.00698	21.82
53.41	(0 2 0)	0.32	0.00559	27.77
58.28	(2 0 2)	0.48	0.00838	18.94
61.53	(1 1 3)	0.32	0.00559	28.87
66.27	(3 1 1)	0.56	0.00977	16.95
68.13	(1 1 3)	0.48	0.00838	19.97
72.40	(3 1 1)	0.44	0.00768	22.37

75.08	(0 0 4)	0.44	0.00768	22.77
			Average	25.14

Appendix C

*** Basic Data Process ***

Group : Standard
Data : YLJE_CuO_300

Strongest 3 peaks

no.	peak no.	2Theta (deg)	d (A)	I/I1	FWHM (deg)	Intensity (Counts)	Integrated Int (Counts)
1	4	35.5350	2.52429	100	0.32130	8286	140756
2	7	38.7395	2.32254	92	0.37560	7604	170391
3	3	34.8807	2.57013	24	0.39700	2004	44130

Peak Data List

peak no.	2Theta (deg)	d (A)	I/I1	FWHM (deg)	Intensity (Counts)	Integrated Int (Counts)
1	31.9921	2.79529	23	0.29520	1919	30369
2	32.4908	2.75351	10	0.33300	815	15186
3	34.8807	2.57013	24	0.39700	2004	44130
4	35.5350	2.52429	100	0.32130	8286	140756
5	36.1000	2.48607	3	0.26660	255	9736
6	38.1000	2.36004	3	0.23520	263	8083
7	38.7395	2.32254	92	0.37560	7604	170391
8	43.8243	2.06413	6	0.31040	525	10195
9	48.8080	1.86437	23	0.36360	1919	44935
10	53.4851	1.71185	6	0.42820	507	13717
11	55.0812	1.66596	4	0.28960	332	5661
12	58.2650	1.58227	10	0.42800	848	22049
13	58.7000	1.57158	4	0.00000	299	0
14	59.1800	1.55997	4	0.31840	299	8715
15	60.7243	1.52395	4	0.42430	293	8018
16	61.5811	1.50478	18	0.33870	1451	30014
17	65.8400	1.41738	9	0.49140	780	20883
18	66.3000	1.40866	14	0.40420	1122	26056
19	68.0239	1.37710	13	0.53110	1065	34137
20	72.4006	1.30425	5	0.41610	377	11447
21	75.0200	1.26507	7	0.32560	572	11576
22	75.4000	1.25963	4	0.25540	369	6880

Figure: XRD information of synthesized CuO-300 NPs with 93.3% matching with ICDD Card No. 00-045-0937 (Part I).

```
          ***  Basic Data Process  ***

# Data Infomation
          Group               : Standard
          Data                : YLJE_CuO_300
          Sample Nmae         : CuO_300
          Comment             :
          Date & Time         : 08-25-25 11:23:40

# Measurement Condition
    X-ray tube
          target              : Cu
          voltage             : 40.0 (kV)
          current             : 30.0 (mA)
    Slits
          Auto Slit           : not Used
          divergence slit     :   1.00000 (deg)
          scatter slit        :   1.00000 (deg)
          receiving slit      :   0.30000(mm)
    Scanning
          drive axis          : Theta-2Theta
          scan range          :   10.0000 - 80.0000 (deg)
          scan mode           : Continuous Scan
          scan speed          :    2.0000 (deg/min)
          sampling pitch      :    0.0200 (deg)
          preset time         :    0.60 (sec)

# Data Process Condition
    Smoothing                 [ AUTO ]
          smoothing points    : 19
    B.G.Subtruction           [ AUTO ]
          sampling points     : 19
          repeat times        : 30
    Ka1-a2 Separate           [ MANUAL ]
          Ka1 a2 ratio        : 50 (%)
    Peak Search               [ AUTO ]
          differential points : 17
          FWHM threhold       : 0.050 (deg)
          intensity threhold  : 30 (par mil)
          FWHM ratio  (n-1)/n : 2
    System error Correction   [ NO ]
    Precise peak Correction   [ NO ]
```

Figure: XRD information of synthesized CuO-300 NPs with 93.3% matching with ICDD Card No. 00-045-0937 (Part II).

< Group: Standard Data: YLJE_CuO_300 >

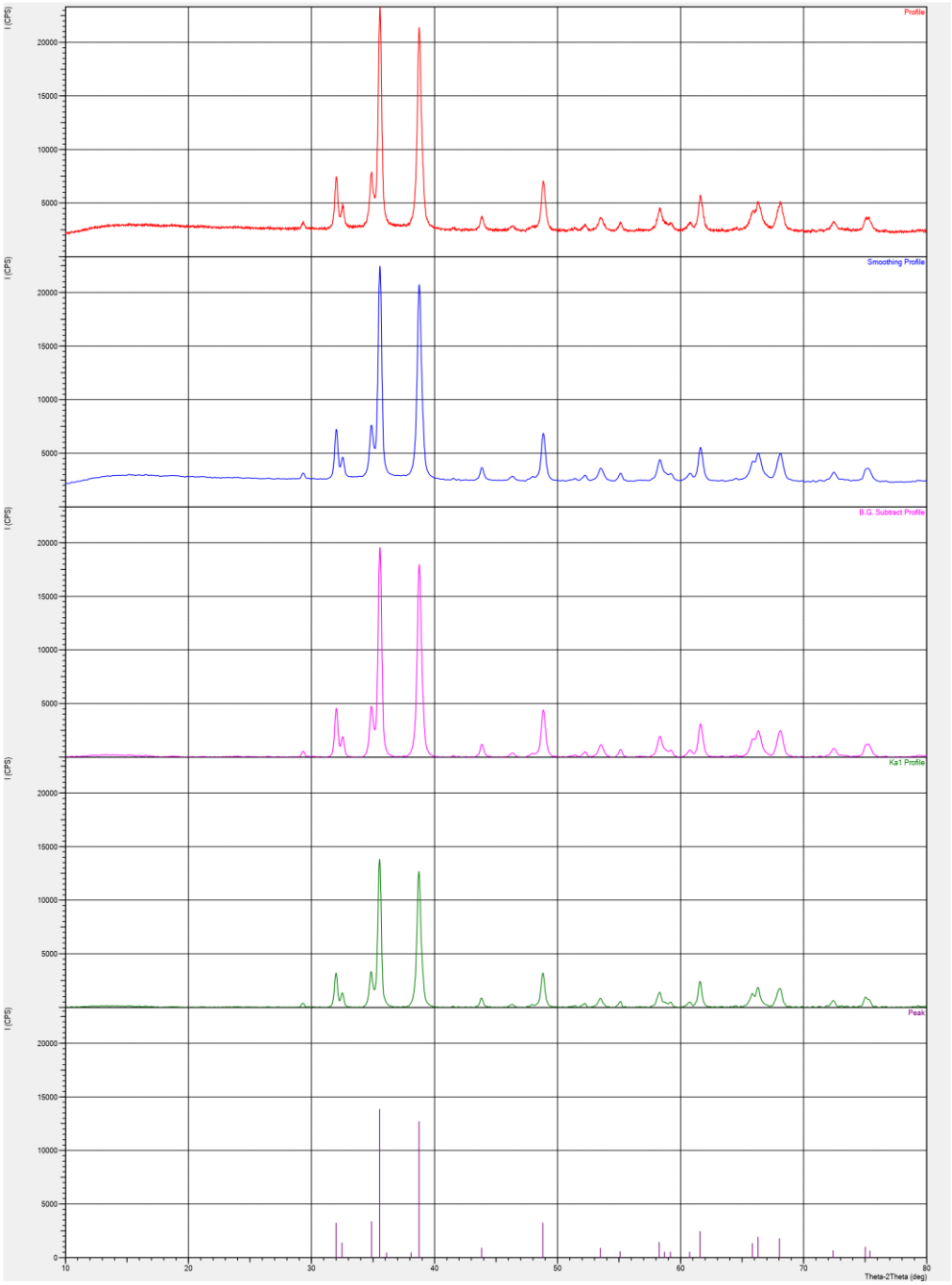

Figure: XRD information of synthesized CuO-300 NPs with 93.3% matching with ICDD Card No. 00-045-0937 (Part III).

Match! Phase Analysis Report

Universiti Tunku Abdul Rahman, Faculty of Science

Sample: CuO_300 ()

Sample Data

File name	YLJE_CuO_300.RAW
File path	C:/xddat/Standard/YLJE_CuO_300
Data collected	Aug 25, 2025 12:00:34
Data range	9.960° - 79.960°
Original data range	10.000° - 80.000°
Number of points	3501
Step size	0.020
Rietveld refinement converged	No
Alpha2 subtracted	No
Background subtr.	No
Data smoothed	No
2theta correction	-0.04°
Radiation	X-rays
Wavelength	1.540600 Å

Matched Phases

Index	*Amount (%)*	*Name*	*Formula sum*
A	93.3	Copper Oxide Tenorite, syn	Cu O
	6.7	*Unidentified peak area*	

A: Copper Oxide Tenorite, syn (93.3 %)

Formula sum	Cu O
Entry number	00-045-0937
Figure-of-Merit (FoM)	0.927846
Total number of peaks	38
Peaks in range	18
Peaks matched	16
Intensity scale factor	0.58
Space group	C2/c
Crystal system	monoclinic
Unit cell	a= 4.6853 Å b= 3.4257 Å c= 5.1303 Å β= 99.549 °
I/Ic	2.50
Meas. density	6.450 g/cm³
Calc. density	6.507 g/cm³
Color	Black
Reference	Martin, K., McCarthy, G., North Dakota State Univ., Fargo, ND, USA., ICDD Grant-in-Aid (1991)

Candidates

Name	*Formula*	*Entry No.*	*FoM*
Silver Copper Oxide	Ag2 Cu2 O3	01-089-6378	0.7278
Copper Strontium Yttrium Oxide	Cu4 Sr4 Y3 O14	00-048-0658	0.7265
Copper Strontium Yttrium Oxide	Cu2 Sr2 Y1.5 O7	00-048-0752	0.7265
Strontium Praseodymium Copper Oxide	(Sr0.83 Pr0.17) Cu O2.02	01-070-7219	0.7197
Silver Copper Oxide	Ag2 Cu2 O3	01-073-6753	0.7082
Silver Copper Oxide	Ag2 Cu2 O3	01-078-3854	0.7082
Strontium Neodymium Copper Oxide	(Sr0.83 Nd0.17) Cu O2.00	01-070-7222	0.7013
Silver Copper Oxide	Ag2 Cu2 O3	01-073-6723	0.6913
Strontium Neodymium Copper Oxide	(Sr0.86 Nd0.14) Cu O2.00	01-070-7223	0.6911
Lead Lanthanum Strontium Copper Oxide	(Pb0.4 Sr0.6) (Pb0.1 La1.4 Sr0.5) Cu2 O5.26	01-086-0504	0.6859
Copper Strontium Neodymium Oxide	(Sr0.85 Nd0.15) Cu O2	01-082-1744	0.6829
Copper Strontium Neodymium Oxide	Cu Nd0.15 Sr0.85 O2	00-049-1745	0.6810
Copper Strontium Gallium Lanthanum Oxide	La Sr2 Ga Cu2 O7	00-045-0302	0.6798
Strontium Lanthanum Copper Oxide	(Sr0.9 La0.1) Cu O2	01-088-2251	0.6768
Strontium Lanthanum Copper Oxide	(Sr0.9 La0.1) Cu O2	01-079-0119	0.6767
Strontium Neodymium Copper Oxide	(Sr0.83 Nd0.17) Cu O2.00	01-070-7221	0.6737
Copper Strontium Cerium Gadolinium Ruthenium Oxide	Gd1.4 Ce0.6 Sr2 Ru Cu2 O10	00-055-0989	0.6736
Copper Strontium Iron Yttrium Cerium Oxide	(Y , Ce)2 Sr Cu Fe O7	00-042-0508	0.6662
Gallium Cadmium Copper Oxide	Ga2 Cd.75 Cu.25 O4	01-086-2254	0.6634
Copper Strontium Ruthenium Oxide	Sr3 (Ru , Cu)2 O7	00-051-0307	0.6629
Copper Strontium Ruthenium Oxide	Sr (Ru0.8 Cu0.2) O3	01-077-8646	0.6614
Strontium Lanthanum Copper Oxide	(Sr0.94 La0.06) Cu O1.89	01-070-7220	0.6595
Barium Copper Yttrium Oxide	Ba2 Y Cu3 O6	01-079-0498	0.6582
Yttrium Strontium Copper Iron Oxide	Y2 Sr Cu Fe O6.5	01-080-1937	0.6561
Lanthanum Strontium Copper Titanium Oxide	La2 Sr4 Cu2 Ti2 O13.4	01-087-1180	0.6555
Strontium Neodymium Mercury Vanadium Copper Oxide	Sr2 (Nd0.53 Sr0.47) ((Hg O2)0.6 (V O4)0.4) (Cu O2)2 O0.14	01-074-3271	0.6541
Mercury Vanadium Strontium Neodymium Copper Oxide	(Hg0.6 V0.4) Sr2 (Nd0.53 Sr0.47) Cu2 O6.94	01-075-2965	0.6541

Figure: XRD information of synthesized CuO-300 NPs with 93.3% matching with ICDD Card No. 00-045-0937 (Part IV).

Copper Strontium Samarium Cerium Ruthenium Niobium Oxide	Ru0.5 Nb0.5 Sr2 Sm1.2 Ce0.8 Cu2 O10-x	00-048-1037	0.6532
Strontium Calcium Copper Oxide	(Sr0.7 Ca0.3) Cu O2	01-079-0190	0.6526
Barium Copper Strontium Cerium Gadolinium Lanthanum Oxide	(Ba0.33 Sr0.33 La0.34)2 (Gd0.67 Ce0.33)2 Cu3 O9.15	00-042-0489	0.6522
Copper Strontium Neodymium Oxide	Sr0.86 Nd0.14 Cu O2	00-049-0637	0.6508
Copper Strontium Cerium Gallium Neodymium Oxide	Ga Sr2 Nd1.3 Ce0.7 Cu2 O9	00-045-0303	0.6500
Mercury Molybdenum Strontium Lanthanum Copper Oxide	(Hg0.62 Mo0.38) Sr2 (Sr0.45 La0.55) Cu2 O6.93	01-089-8210	0.6493
Copper Manganese Iron Oxide	Cu0.5 Mn1.5 Fe O4	01-074-2160	0.6488
Barium Copper Strontium Praseodymium Thallium Oxide	Tl (Ba0.4 Sr1.6) Pr Cu2 O7-x	00-049-0880	0.6487
Cadmium Copper Chromium Oxide	(Cd0.9 Cu0.1) (Cr2 O4)	01-077-8285	0.6486
Barium Copper Strontium Cerium Neodymium Ruthenium Oxide	(Ru0.5 Cu0.5) (Sr1.47 Ba0.2 Nd0.33) (Nd1.34 Ce0.66) Cu2 O12	01-084-3654	0.6480
Barium Copper Cerium Gadolinium Titanium Oxide	Ti2 Ba2 Gd2.25 Ce0.75 Cu2 O13	00-050-0463	0.6479
Mercury Lead Strontium Lanthanum Copper Oxide	(Hg0.28 Pb0.5 Cu0.22) (Sr1.7 La0.3) (Sr0.44 La0.56) Cu2 O6.56	01-087-2339	0.6470
Samarium Cerium Barium Copper Oxide	(Sm0.667 Ce0.333)4 (Sm0.333 Ba0.667)4 Cu5.88 O17.8	01-079-1792	0.6465
Barium Copper Yttrium Oxide	Ba2 Y Cu3 O6	01-079-0499	0.6461
Strontium Copper Oxide	Sr1.01 Cu O2	01-086-0071	0.6452
Lanthanum Strontium Copper Gallium Oxide	La Sr2 Cu2 Ga O7	01-080-2387	0.6449
Copper Strontium Cerium Gadolinium Manganese Ruthenium Oxide	Gd1.4 Ce0.6 Sr2 Ru0.7 Mn0.3 Cu2 O10	00-055-0990	0.6446
Copper Palladium Oxide	Cu Pd O2	00-044-0185	0.6434
Barium Copper Lead Iron Oxide Bromide	Pb2 Ba Cu Fe O5 Br	00-048-0426	0.6419
Calcium Copper Strontium Rhenium Oxide	Sr2 Cu (Re0.69 Ca0.31) O6	01-075-8492	0.6417
Lanthanum Strontium Copper Gallium Oxide	La Sr Cu Ga O5	01-076-0438	0.6412
Thallium Barium Strontium Praseodymium Copper Oxide	Tl0.899 (Ba0.4 Sr1.6) Pr Cu2 O6.87	01-082-1655	0.6409
Ruthenium Copper Strontium Neodymium Cerium Oxide	(Ru0.97 Cu0.03) (Sr1.88 Nd0.12) (Nd0.7 Ce0.3)2 Cu2 O9.82	01-074-7267	0.6390
Lanthanum Strontium Copper Oxide	La2 Sr Cu2 O6.03	01-088-1601	0.6384
Lanthanum Barium Strontium Copper Oxide	(La1.9 Ba0.1 Sr) Cu2 O6.09	01-080-1367	0.6379
and 110 others...			

Search-Match

Settings

Reference database used	PDF-2 Release 2016 RDB
Automatic zeropoint adaptation	Yes
Minimum figure-of-merit (FoM)	0.60
2theta window for peak corr.	0.30 deg.
Minimum rel. int. for peak corr.	1
Parameter/influence 2theta	0.50
Parameter/influence intensities	0.50
Parameter multiple/single phase(s)	0.50

Selection Criteria

Elements:

Elements that must be present:	O, Cu
Elements that may be present:	All elements not mentioned above

Peak List

No.	*2theta [°]*	*d [Å]*	*I/I0*	*FWHM*	*Matched*
1	29.30	3.0462	29.70	0.2000	
2	31.99	2.7959	232.48	0.2800	
3	32.51	2.7517	96.07	0.1600	A
4	34.83	2.5734	241.68	0.4000	
5	35.53	2.5245	1000.00	0.3200	A
6	38.72	2.3239	916.47	0.3600	A
7	43.72	2.0688	45.43	0.2400	
8	48.74	1.8668	200.51	0.3600	A
9	52.23	1.7500	22.62	0.1600	
10	53.40	1.7144	53.00	0.2800	A
11	55.04	1.6671	35.79	0.2800	
12	58.28	1.5818	97.28	0.4000	A
13	60.75	1.5234	32.92	0.3200	
14	61.52	1.5061	143.65	0.2800	A
15	65.85	1.4173	75.95	0.4800	A
16	66.26	1.4093	113.52	0.6000	A
17	67.88	1.3797	86.06	0.3200	A
18	72.41	1.3041	38.58	0.4000	A
19	75.03	1.2649	55.78	0.3200	A
20	75.25	1.2618	59.83	0.5600	A

Rietveld Refinement using FullProf

Figure: XRD information of synthesized CuO-300 NPs with 93.3% matching with ICDD Card No. 00-045-0937 (Part V).

Calculation was not run or did not converge.

Crystallite Size Estimation using Scherrer Formula

Calculation was not run.

Degree of crystallinity analysis

Profile area	*Counts*	*Amount*
Total area	6436128	100.00%
Diffraction peaks	1026400	15.95%
Background	5409728	84.05%
Instrumental background	892103	13.86%
Amorphous phases	4517625	70.19%

Degree of crystallinity (DOC) = 18.51%
Amorphous content (weight %) =81.49%

Integrated Profile Areas

Based on calculated profile

Profile area	*Counts*	*Amount*
Overall diffraction profile	6436128	100.00%
Background radiation	5409728	84.05%
Diffraction peaks	1026400	15.95%
Peak area belonging to selected phases	592748	9.21%
Peak area of phase A (Copper Oxide Tenorite, syn)	*592748*	*9.21%*
Unidentified peak area	433652	6.74%

Peak Residuals

Peak data	*Counts*	*Amount*
Overall peak intensity	19475	100.00%
Peak intensity belonging to selected phases	16560	85.03%
Unidentified peak intensity	2915	14.97%

Diffraction Pattern Graphics

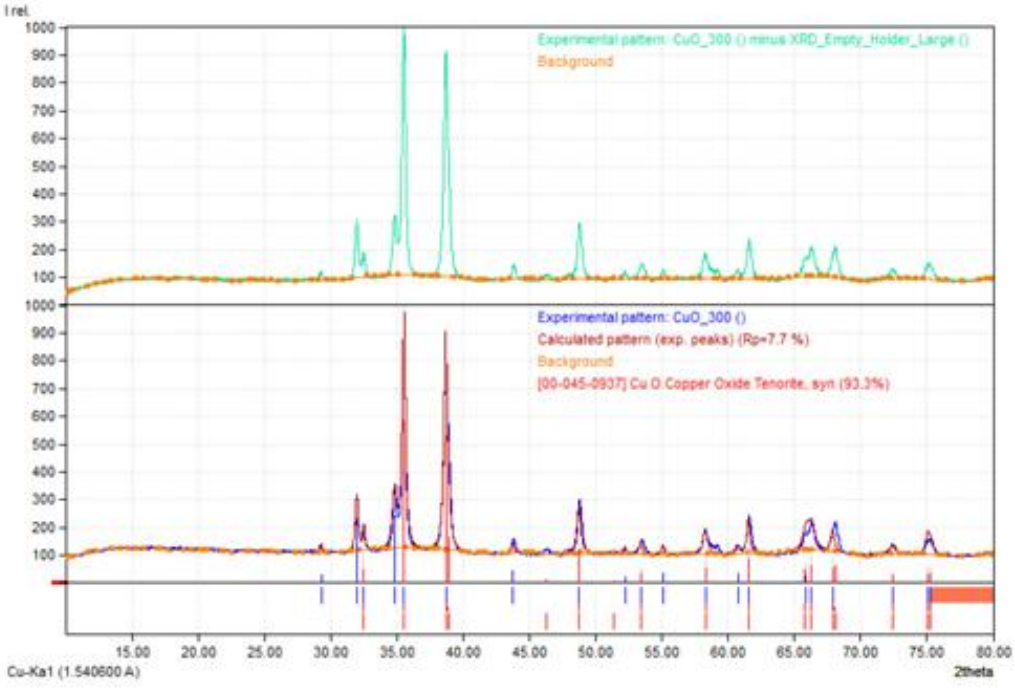

Figure: XRD information of synthesized CuO-300 NPs with 93.3% matching with ICDD Card No. 00-045-0937 (Part VI).

Appendix D

*** Basic Data Process ***

Group : Standard
Data : YLJE_CuO_400

Strongest 3 peaks

no.	peak no.	2Theta (deg)	d (A)	I/I1	FWHM (deg)	Intensity (Counts)	Integrated Int (Counts)
1	5	35.5199	2.52533	100	0.31800	8663	152693
2	6	38.7224	2.32352	93	0.36720	8024	184191
3	8	48.8042	1.86451	24	0.34470	2079	47294

Peak Data List

peak no.	2Theta (deg)	d (A)	I/I1	FWHM (deg)	Intensity (Counts)	Integrated Int (Counts)
1	29.2829	3.04744	3	0.23160	267	4393
2	31.9778	2.79650	23	0.29350	1993	32051
3	32.4827	2.75418	10	0.30280	874	15255
4	34.8697	2.57091	24	0.41410	2072	48266
5	35.5199	2.52533	100	0.31800	8663	152693
6	38.7224	2.32352	93	0.36720	8024	184191
7	43.8112	2.06471	6	0.28330	557	10879
8	48.8042	1.86451	24	0.34470	2079	47294
9	53.4674	1.71237	6	0.38060	553	13598
10	55.0577	1.66661	4	0.28160	368	6007
11	58.2652	1.58227	11	0.43680	916	21078
12	58.7400	1.57061	4	0.35120	310	5432
13	59.1292	1.56119	4	0.41850	305	5971
14	60.7124	1.52422	3	0.42710	298	8405
15	61.5732	1.50496	18	0.33470	1517	30459
16	65.8200	1.41776	9	0.54060	807	21547
17	66.2763	1.40910	14	0.47270	1200	28579
18	68.0231	1.37711	13	0.54350	1085	35341
19	72.3776	1.30460	5	0.33860	444	11517
20	75.1318	1.26346	7	0.58770	564	20089

Figure: XRD information of synthesized CuO-400 NPs with 94.4% matching with ICDD Card No. 01-077-7717 (Part I).

```
         ***  Basic Data Process  ***

# Data Infomation
          Group               : Standard
          Data                : YLJE_CuO_400
          Sample Nmae         : CuO_400
          Comment             :
          Date & Time         : 08-25-25 12:02:29

# Measurement Condition
    X-ray tube
          target              : Cu
          voltage             : 40.0 (kV)
          current             : 30.0 (mA)
    Slits
          Auto Slit           : not Used
          divergence slit     :   1.00000 (deg)
          scatter slit        :   1.00000 (deg)
          receiving slit      :   0.30000(mm)
    Scanning
          drive axis          : Theta-2Theta
          scan range          :   10.0000 - 80.0000 (deg)
          scan mode           : Continuous Scan
          scan speed          :    2.0000 (deg/min)
          sampling pitch      :    0.0200 (deg)
          preset time         :    0.60 (sec)

# Data Process Condition
    Smoothing                 [ AUTO ]
          smoothing points    : 17
    B.G.Subtruction           [ AUTO ]
          sampling points     : 19
          repeat times        : 30
    Ka1-a2 Separate           [ MANUAL ]
          Ka1 a2 ratio        : 50 (%)
    Peak Search               [ AUTO ]
          differential points : 17
          FWHM threhold       : 0.050 (deg)
          intensity threhold  : 30 (par mil)
          FWHM ratio  (n-1)/n : 2
    System error Correction   [ NO ]
    Precise peak Correction   [ NO ]
```

Figure: XRD information of synthesized CuO-400 NPs with 94.4% matching with ICDD Card No. 01-077-7717 (Part II).

< Group: Standard Data: YLJE_CuO_400 >

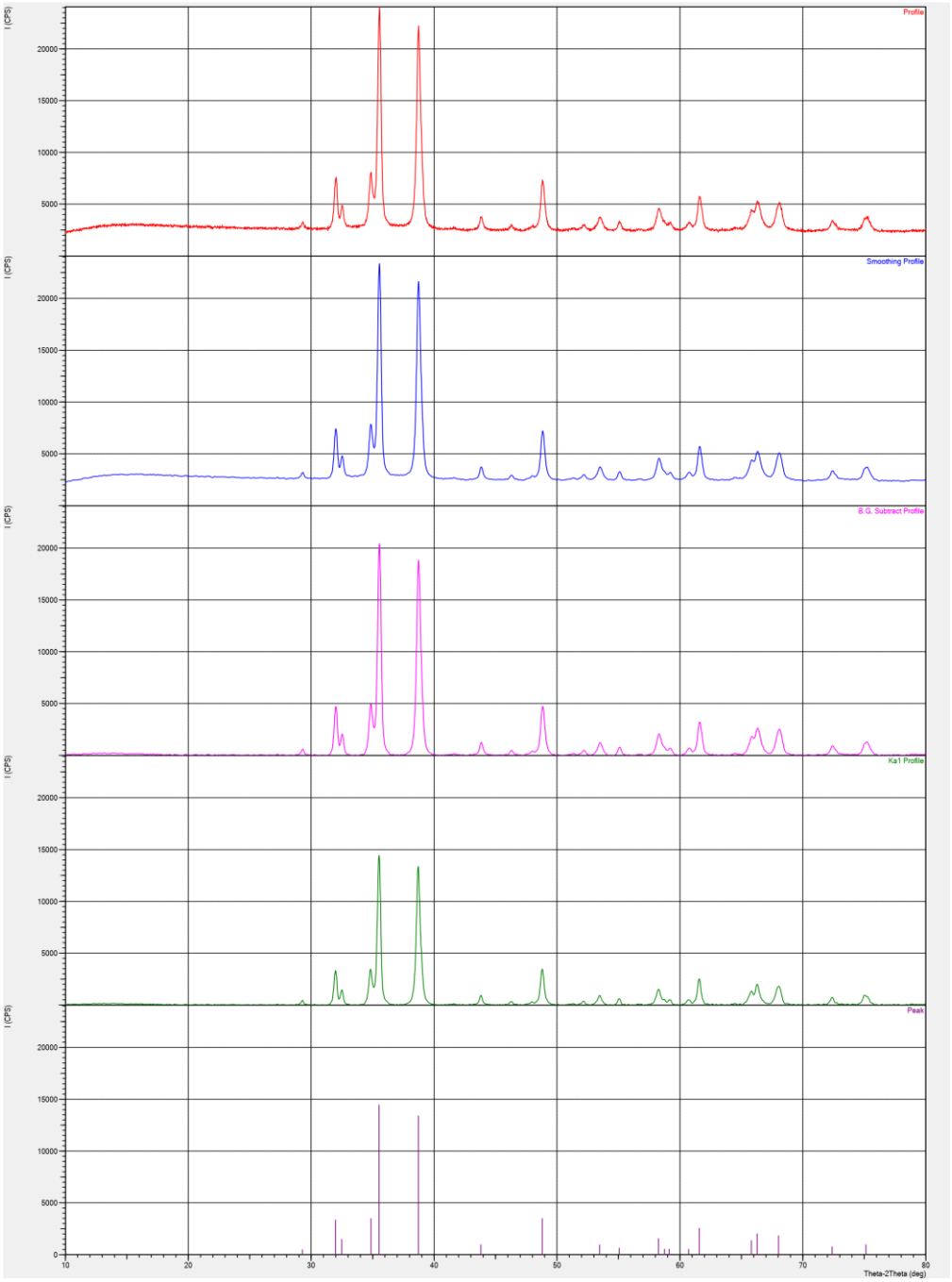

Figure: XRD information of synthesized CuO-400 NPs with 94.4% matching with ICDD Card No. 01-077-7717 (Part III).

Match! Phase Analysis Report

Universiti Tunku Abdul Rahman, Faculty of Science

Sample: CuO_400 ()

Sample Data

File name	YLJE_CuO_400.RAW
File path	C:/xddat/Standard/YLJE_CuO_400
Data collected	Aug 25, 2025 12:39:24
Data range	9.840° - 79.840°
Original data range	10.000° - 80.000°
Number of points	3501
Step size	0.020
Rietveld refinement converged	No
Alpha2 subtracted	No
Background subtr.	No
Data smoothed	No
2theta correction	-0.16°
Radiation	X-rays
Wavelength	1.540600 Å

Matched Phases

Index	Amount (%)	Name	Formula sum
A	94.4	Copper oxide	Cu O
	5.6	*Unidentified peak area*	

A: Copper oxide (94.4 %)

Formula sum	Cu O
Entry number	01-077-7717
Figure-of-Merit (FoM)	0.917656
Total number of peaks	74
Peaks in range	22
Peaks matched	14
Intensity scale factor	1.06
Space group	C2/c
Crystal system	monoclinic
Unit cell	a= 4.6863 Å b= 3.4276 Å c= 5.1333 Å β= 99.520 °
I/Ic	3.73
Calc. density	6.497 g/cm³
Reference	Forsyth, J.B., Hull, S., J. Phys.: Condens. Matter **3**, 5257 (1991)

Candidates

Name	Formula	Entry No.	FoM
Strontium Lanthanum Copper Oxide	(Sr0.94 La0.06) Cu O1.89	01-070-7220	0.7926
Strontium Europium Copper Oxide	(Sr0.98 Eu0.02) Cu O1.96	01-070-7224	0.7870
Strontium Copper Oxide	Sr1.01 Cu O2	01-086-0071	0.7859
Strontium Neodymium Copper Oxide	(Sr0.96 Nd0.04) Cu O2.02	01-082-1745	0.7821
Strontium Lanthanum Copper Oxide	(Sr0.92 La0.08) Cu O1.89	01-070-7217	0.7768
Copper Strontium Oxide	Cu Sr O2	00-046-0022	0.7425
Copper Strontium Oxide	Sr Cu O2.08	01-082-1743	0.7421
Strontium Neodymium Copper Oxide	(Sr0.88 Nd0.12) Cu O2	01-087-1314	0.7412
Strontium Neodymium Copper Oxide	(Sr0.82 Nd0.18) Cu O2	01-087-1316	0.7396
Strontium Europium Copper Oxide	(Sr0.92 Eu0.08) Cu O2.03	01-074-2760	0.7268
Strontium Lanthanum Copper Oxide	(Sr0.86 La0.14) Cu O1.98	01-070-7218	0.7231
Strontium Calcium Copper Oxide	(Sr0.7 Ca0.3) Cu O2	01-079-0190	0.7154
Copper Strontium Ruthenium Oxide	Sr3 (Ru , Cu)2 O7	00-051-0307	0.7072
Copper Strontium Yttrium Oxide	Cu4 Sr4 Y3 O14	00-048-0658	0.7067
Copper Strontium Yttrium Oxide	Cu2 Sr2 Y1.5 O7	00-048-0752	0.7067
Copper Strontium Lanthanum Oxide	Sr0.92 La0.08 Cu O1.89	00-051-0309	0.7035
Silver Copper Oxide	Ag2 Cu2 O3	01-073-6723	0.7015
Silver Copper Oxide	Ag2 Cu2 O3	01-089-6378	0.6984
Strontium Praseodymium Copper Oxide	(Sr0.9 Pr0.1) Cu O2	01-087-1315	0.6926
Neodymium Barium Copper Oxide	(Nd0.925 Ba0.075)2 Cu O4-x	00-038-0342	0.6892
Copper Strontium Ruthenium Oxide	Sr (Ru0.8 Cu0.2) O3	01-077-8646	0.6879
Silver Copper Oxide	Ag2 Cu2 O3	01-073-6753	0.6878
Silver Copper Oxide	Ag2 Cu2 O3	01-078-3854	0.6878
Strontium Lanthanum Copper Oxide	(Sr0.9 La0.1) Cu O2	01-088-2251	0.6748
Barium Copper Neodymium Tin Titanium Oxide	Ba2 Cu2 Nd2 Sn Ti O11	00-048-0994	0.6726
Strontium Lanthanum Copper Oxide	(Sr0.9 La0.1) Cu O2	01-079-0119	0.6710
Strontium Neodymium Copper Oxide	(Sr0.83 Nd0.17) Cu O2.00	01-070-7222	0.6694
Strontium Neodymium Copper Oxide	(Sr0.83 Nd0.17) Cu O2.00	01-070-7221	0.6686
Copper Strontium Neodymium Oxide	Sr0.86 Nd0.14 Cu O2	00-049-0637	0.6683
Strontium Europium Copper Oxide	(Sr0.79 Eu0.21) Cu O1.94	01-070-7225	0.6674
Strontium Neodymium Copper Oxide	(Sr0.86 Nd0.14) Cu O2.00	01-070-7223	0.6665

Figure: XRD information of synthesized CuO-400 NPs with 94.4% matching with ICDD Card No. 01-077-7717 (Part IV).

Strontium Neodymium Copper Oxide	(Sr0.86 Nd0.14) Cu O2	01-085-1946	0.6663
Strontium Praseodymium Copper Oxide	(Sr0.83 Pr0.17) Cu O2.02	01-070-7219	0.6627
Barium Copper Strontium Cerium Gadolinium Titanium Oxide	Ti3 Ba2 Sr Gd2.25 Ce0.75 Cu2 O16	00-050-0431	0.6618
Lithium Copper Strontium Tungsten Oxide	Li0.5 Cu0.5 Sr2 W O6-x	00-049-0695	0.6602
Copper Strontium Neodymium Oxide	(Sr0.83 Nd0.17) Cu O2	00-051-0308	0.6563
Copper Strontium Neodymium Oxide	Cu Nd0.15 Sr0.85 O2	00-049-1745	0.6554
Copper Strontium Neodymium Oxide	(Sr0.85 Nd0.15) Cu O2	01-082-1744	0.6538
Neodymium Copper Oxide	Nd1.888 Cu O3.78	01-083-0845	0.6528
Copper Manganese Selenite	(Cu0.25 Mn0.75) (Se O3)	01-072-7831	0.6502
Neodymium Copper Oxide	Nd2 Cu O4	01-084-2178	0.6485
Neodymium Copper Oxide	Nd2 Cu O4	01-082-1734	0.6477
Copper Copper Oxide (Paramelaconite)	Cu4 O3	01-083-1665	0.6474
Neodymium Cerium Copper Oxide	(Nd1.83 Ce0.17) Cu O4	01-080-1649	0.6442
Neodymium Copper Oxide	Nd2 Cu O3.97	01-082-2077	0.6442
Neodymium Copper Oxide	Nd2 Cu O4	01-080-2031	0.6426
Neodymium Cerium Copper Oxide	(Nd1.83 Ce0.17) Cu O4	01-080-1648	0.6425
Neodymium Cerium Copper Oxide	(Nd1.835 Ce0.165) Cu O4	01-082-1740	0.6417
Copper Neodymium Oxide	Nd2 Cu O4	01-076-7799	0.6409
Neodymium Cerium Copper Oxide	Nd1.85 Ce.15 Cu O3.946	01-079-1844	0.6399
Neodymium Cerium Copper Oxide	Nd1.85 Ce.15 Cu O3.962	01-079-1842	0.6394
Neodymium Cerium Copper Oxide	Nd1.85 Ce.15 Cu O4	01-079-1918	0.6394
and 78 others...			

Search-Match

Settings

Reference database used	PDF-2 Release 2016 RDB
Automatic zeropoint adaptation	Yes
Minimum figure-of-merit (FoM)	0.60
2theta window for peak corr.	0.30 deg.
Minimum rel. int. for peak corr.	1
Parameter/influence 2theta	0.50
Parameter/influence intensities	0.50
Parameter multiple/single phase(s)	0.50

Selection Criteria

Elements:

Elements that must be present:	O, Cu
Elements that may be present:	All elements not mentioned above

Peak List

No.	*2theta [°]*	*d [Å]*	*I/I0*	*FWHM*	*Matched*
1	29.16	3.0602	33.62	0.2000	
2	31.76	2.8152	180.91	0.3200	
3	32.37	2.7638	98.14	0.3200	A
4	34.70	2.5831	237.48	0.3600	
5	35.40	2.5337	1000.00	0.3200	A
6	38.58	2.3319	921.10	0.3600	A
7	43.69	2.0701	57.26	0.2800	
8	46.17	1.9645	25.40	0.2000	A
9	48.67	1.8693	225.99	0.3600	A
10	52.06	1.7554	21.70	0.2400	
11	53.32	1.7166	57.35	0.3200	A
12	54.94	1.6700	39.76	0.3200	
13	58.13	1.5856	91.94	0.5200	A
14	59.07	1.5626	28.31	0.2800	
15	60.61	1.5267	28.96	0.2400	
16	61.38	1.5092	140.88	0.3200	A
17	65.66	1.4208	82.67	0.5200	A
18	66.14	1.4117	120.85	0.5600	A
19	67.74	1.3822	87.32	0.3600	A
20	72.26	1.3064	40.22	0.4000	A
21	74.88	1.2670	50.98	0.4000	A
22	75.09	1.2641	56.50	0.4000	A

Rietveld Refinement using FullProf

Calculation was not run or did not converge.

Crystallite Size Estimation using Scherrer Formula

Calculation was not run.

Degree of crystallinity analysis

Figure: XRD information of synthesized CuO-400 NPs with 94.4% matching with ICDD Card No. 01-077-7717 (Part V).

Profile area	*Counts*	*Amount*
Total area	6576302	100.00%
Diffraction peaks	1058917	16.10%
Background	5517385	83.90%
Instrumental background	892103	13.57%
Amorphous phases	4625282	70.33%

Degree of crystallinity (DOC) = 18.63%
Amorphous content (weight %) =81.37%

Integrated Profile Areas

Based on calculated profile

Profile area	*Counts*	*Amount*
Overall diffraction profile	6576302	100.00%
Background radiation	5517385	83.90%
Diffraction peaks	1058917	16.10%
Peak area belonging to selected phases	692605	10.53%
Peak area of phase A (Copper oxide)	*692605*	*10.53%*
Unidentified peak area	366311	5.57%

Peak Residuals

Peak data	*Counts*	*Amount*
Overall peak intensity	20937	100.00%
Peak intensity belonging to selected phases	19185	91.63%
Unidentified peak intensity	1753	8.37%

Diffraction Pattern Graphics

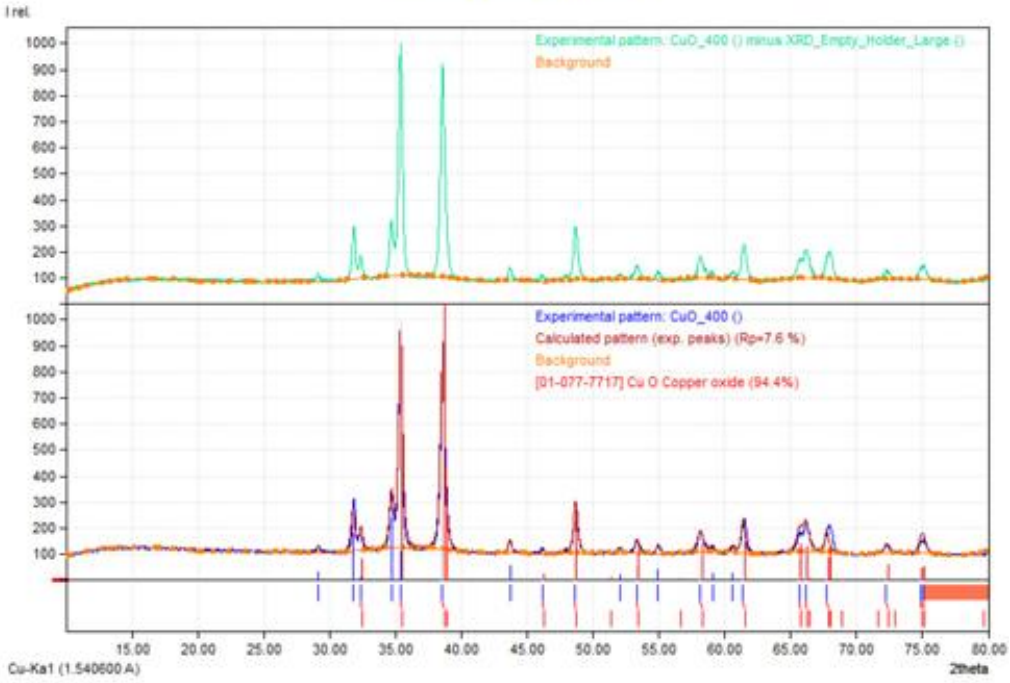

Figure: XRD information of synthesized CuO-400 NPs with 94.4% matching with ICDD Card No. 01-077-7717 (Part VI).

Appendix E

*** Basic Data Process ***

Group : Standard
Data : YLJE_CuO_500

Strongest 3 peaks

no.	peak no.	2Theta (deg)	d (A)	I/I1	FWHM (deg)	Intensity (Counts)	Integrated Int (Counts)
1	4	35.5026	2.52652	100	0.32230	9318	167164
2	5	38.7022	2.32469	91	0.37810	8470	197624
3	3	34.8400	2.57304	24	0.37490	2243	49197

Peak Data List

peak no.	2Theta (deg)	d (A)	I/I1	FWHM (deg)	Intensity (Counts)	Integrated Int (Counts)
1	31.9637	2.79770	23	0.29560	2155	34609
2	32.4705	2.75519	10	0.29820	951	15774
3	34.8400	2.57304	24	0.37490	2243	49197
4	35.5026	2.52652	100	0.32230	9318	167164
5	38.7022	2.32469	91	0.37810	8470	197624
6	43.8069	2.06491	6	0.31070	593	12406
7	48.4200	1.87840	3	0.21580	306	7086
8	48.7986	1.86471	23	0.34970	2184	42752
9	53.4583	1.71264	6	0.40670	566	14365
10	55.0441	1.66699	4	0.25530	417	6472
11	58.2235	1.58330	10	0.44840	949	25302
12	58.6800	1.57207	3	0.00000	307	0
13	59.1629	1.56038	4	0.33730	340	8890
14	60.6723	1.52513	3	0.37230	321	7857
15	61.5590	1.50527	17	0.33300	1626	33000
16	65.7600	1.41891	8	0.43000	775	20683
17	66.3000	1.40866	13	0.39160	1228	28781
18	68.0006	1.37751	12	0.55180	1138	36434
19	72.3507	1.30502	5	0.43200	439	14024
20	75.1119	1.26375	6	0.61440	602	21580

Figure: XRD information of synthesized CuO-500 NPs with 95.1% matching with ICDD Card No. 00-005-0661 (Part I).

```
         ***  Basic Data Process  ***

# Data Infomation
          Group                : Standard
          Data                 : YLJE CuO_500
          Sample Nmae          : CuO_500
          Comment              :
          Date & Time          : 08-25-25 14:02:05

# Measurement Condition
    X-ray tube
          target               : Cu
          voltage              : 40.0 (kV)
          current              : 30.0 (mA)
    Slits
          Auto Slit            : not Used
          divergence slit      :   1.00000 (deg)
          scatter slit         :   1.00000 (deg)
          receiving slit       :   0.30000(mm)
    Scanning
          drive axis           : Theta-2Theta
          scan range           :   10.0000 - 80.0000 (deg)
          scan mode            : Continuous Scan
          scan speed           :    2.0000 (deg/min)
          sampling pitch       :    0.0200 (deg)
          preset time          :    0.60 (sec)

# Data Process Condition
    Smoothing                  [ AUTO ]
          smoothing points     : 17
    B.G.Subtruction            [ AUTO ]
          sampling points      : 19
          repeat times         : 30
    Ka1-a2 Separate            [ MANUAL ]
          Ka1 a2 ratio         : 50 (%)
    Peak Search                [ AUTO ]
          differential points  : 17
          FWHM threhold        : 0.050 (deg)
          intensity threhold   : 30 (par mil)
          FWHM ratio  (n-1)/n  : 2
    System error Correction    [ NO ]
    Precise peak Correction    [ NO ]
```

Figure: XRD information of synthesized CuO-500 NPs with 95.1% matching with ICDD Card No. 00-005-0661 (Part II).

< Group: Standard Data: YLJE_CuO_500 >

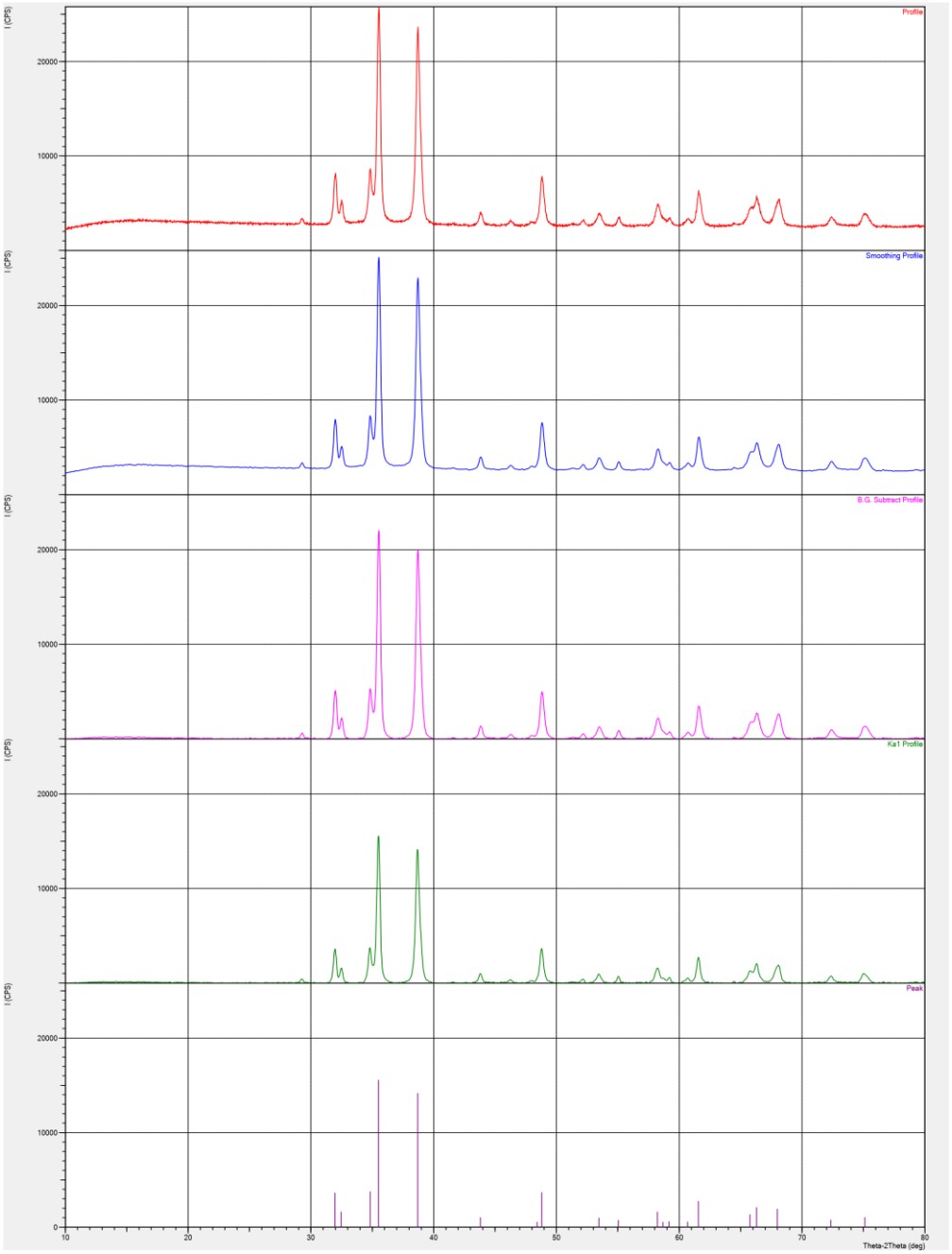

Figure: XRD information of synthesized CuO-500 NPs with 95.1% matching with ICDD Card No. 00-005-0661 (Part III).

Match! Phase Analysis Report

Universiti Tunku Abdul Rahman, Faculty of Science

Sample: CuO_500 ()

Sample Data

File name	YLJE_CuO_500.RAW
File path	C:/xddat/Standard/YLJE_CuO_500
Data collected	Aug 25, 2025 14:39:02
Data range	10.010° - 80.010°
Original data range	10.000° - 80.000°
Number of points	3501
Step size	0.020
Rietveld refinement converged	No
Alpha2 subtracted	No
Background subtr.	No
Data smoothed	No
2theta correction	0.01°
Radiation	X-rays
Wavelength	1.540600 Å

Matched Phases

Index	*Amount (%)*	*Name*	*Formula sum*
A	95.1	Copper Oxide Tenorite, syn	Cu O
	4.9	*Unidentified peak area*	

A: Copper Oxide Tenorite, syn (95.1 %)

Formula sum	Cu O
Entry number	00-005-0661
Figure-of-Merit (FoM)	0.911298
Total number of peaks	37
Peaks in range	17
Peaks matched	15
Intensity scale factor	0.73
Space group	C2/c
Crystal system	monoclinic
Unit cell	a= 4.6840 Å b= 3.4250 Å c= 5.1290 Å β= 99.470 °
I/Ic	1.90
Calc. density	6.510 g/cm³
Color	Black
Reference	Swanson, Tatge., Natl. Bur. Stand. (U. S.), Circ. 539 I, 49 (1953)

Candidates

Name	*Formula*	*Entry No.*	*FoM*
Copper Strontium Neodymium Oxide	(Sr0.85 Nd0.15) Cu O2	01-082-1744	0.7290
Copper Strontium Yttrium Oxide	Cu4 Sr4 Y3 O14	00-048-0658	0.7236
Copper Strontium Yttrium Oxide	Cu2 Sr2 Y1.5 O7	00-048-0752	0.7236
Strontium Neodymium Copper Oxide	(Sr0.83 Nd0.17) Cu O2.00	01-070-7222	0.7006
Silver Copper Oxide	Ag2 Cu2 O3	01-089-6378	0.6989
Strontium Neodymium Copper Oxide	(Sr0.86 Nd0.14) Cu O2.00	01-070-7223	0.6951
Silver Copper Oxide	Ag2 Cu2 O3	01-073-6723	0.6943
Strontium Neodymium Copper Oxide	(Sr0.82 Nd0.18) Cu O2	01-087-1316	0.6903
Silver Copper Oxide	Ag2 Cu2 O3	01-073-6753	0.6866
Silver Copper Oxide	Ag2 Cu2 O3	01-078-3854	0.6866
Strontium Calcium Copper Oxide	(Sr0.7 Ca0.3) Cu O2	01-079-0190	0.6856
Copper Strontium Neodymium Oxide	Sr0.86 Nd0.14 Cu O2	00-049-0637	0.6819
Strontium Copper Oxide	Sr1.01 Cu O2	01-086-0071	0.6814
Strontium Praseodymium Copper Oxide	(Sr0.83 Pr0.17) Cu O2.02	01-070-7219	0.6811
Strontium Lanthanum Copper Oxide	(Sr0.94 La0.06) Cu O1.89	01-070-7220	0.6768
Strontium Neodymium Copper Oxide	(Sr0.83 Nd0.17) Cu O2.00	01-070-7221	0.6752
Strontium Lanthanum Copper Oxide	(Sr0.9 La0.1) Cu O2	01-079-0119	0.6745
Strontium Neodymium Copper Oxide	(Sr0.86 Nd0.14) Cu O2	01-085-1946	0.6738
Strontium Praseodymium Copper Oxide	(Sr0.9 Pr0.1) Cu O2	01-087-1315	0.6731
Strontium Lanthanum Copper Oxide	(Sr0.9 La0.1) Cu O2	01-088-2251	0.6717
Strontium Neodymium Copper Oxide	(Sr0.88 Nd0.12) Cu O2	01-087-1314	0.6716
Strontium Europium Copper Oxide	(Sr0.98 Eu0.02) Cu O1.96	01-070-7224	0.6661
Strontium Lanthanum Copper Oxide	(Sr0.92 La0.08) Cu O1.89	01-070-7217	0.6613
Strontium Neodymium Copper Oxide	(Sr0.96 Nd0.04) Cu O2.02	01-082-1745	0.6609
Copper Strontium Neodymium Oxide	(Sr0.83 Nd0.17) Cu O2	00-051-0308	0.6590
Copper Strontium Ruthenium Oxide	Sr (Ru0.8 Cu0.2) O3	01-077-8646	0.6590
Copper Strontium Neodymium Oxide	Cu Nd0.15 Sr0.85 O2	00-049-1745	0.6576
Copper Manganese Selenite	(Cu0.25 Mn0.75) (Se O3)	01-072-7831	0.6511
Strontium Europium Copper Oxide	(Sr0.92 Eu0.08) Cu O2.03	01-074-2760	0.6510

Figure: XRD information of synthesized CuO-500 NPs with 95.1% matching with ICDD Card No. 00-005-0661 (Part IV).

Strontium Europium Copper Oxide	(Sr0.79 Eu0.21) Cu O1.94	01-070-7225	0.6459
Strontium Lanthanum Copper Oxide	(Sr0.86 La0.14) Cu O1.98	01-070-7218	0.6425
Barium Copper Strontium Cerium Gadolinium Titanium Oxide	Ti3 Ba2 Sr Gd2.25 Ce0.75 Cu2 O16	00-050-0431	0.6381
Barium Copper Yttrium Oxide	Ba2 Y Cu3 O6	01-079-0498	0.6335
Calcium Magnesium Copper Vanadium Oxide	Ca10 Mg5 Cu3 V12 O48	01-072-1418	0.6297
Yttrium Barium Copper Oxide	Y Ba2 Cu3 O6.34	01-082-0245	0.6277
Copper Strontium Lanthanum Oxide	Sr0.92 La0.08 Cu O1.89	00-051-0309	0.6261
Yttrium Barium Copper Oxide	Y Ba2 Cu3 O6.4	01-082-0244	0.6261
Gadolinium Copper Oxide	Gd2 Cu O4	01-081-0880	0.6237
Europium Copper Oxide	Eu2 (Cu O4)	01-080-2366	0.6236
Europium Copper Oxide	Eu2 Cu O4	01-081-0879	0.6236
Barium Copper Yttrium Oxide	Ba2 Y Cu3 O6	01-079-0499	0.6218
Gadolinium Copper Oxide	Gd2 (Cu O4)	01-086-1152	0.6211
Copper Europium Oxide	Eu2 Cu O4	00-052-1719	0.6209
Gadolinium Copper Oxide	Gd2 (Cu O4)	01-080-2367	0.6205
Gadolinium Copper Oxide	Gd1.726 Cu O4	01-087-1448	0.6192
Gadolinium Copper Oxide	Gd1.728 Cu O4	01-087-1449	0.6192
Mercury Molybdenum Strontium Lanthanum Copper Oxide	(Hg0.62 Mo0.38) Sr2 (Sr0.45 La0.55) Cu2 O6.93	01-089-8210	0.6187
Barium Copper Strontium Praseodymium Thallium Oxide	Tl (Ba0.4 Sr1.6) Pr Cu2 O7-x	00-049-0880	0.6176
Yttrium Barium Copper Oxide	Y Ba2 Cu3 O6.35	01-082-0255	0.6173
Lanthanum Barium Calcium Copper Oxide	(La0.5 Ba1.5) (La0.5 Ca0.5) Cu3 O6.46	01-089-8890	0.6161
Copper Vanadium Oxide	Cu V2 O5	00-043-0080	0.6159
Gadolinium Copper Oxide	Gd2 Cu O4	01-079-0102	0.6159
and 26 others...			

Search-Match

Settings

Reference database used	PDF-2 Release 2016 RDB
Automatic zeropoint adaptation	Yes
Minimum figure-of-merit (FoM)	0.60
2theta window for peak corr.	0.30 deg.
Minimum rel. int. for peak corr.	1
Parameter/Influence 2theta	0.50
Parameter/Influence intensities	0.50
Parameter multiple/single phase(s)	0.50

Selection Criteria

Elements:

Elements that must be present:	O, Cu
Elements that may be present:	All elements not mentioned above

Peak List

No.	*2theta [°]*	*d [Å]*	*I/I0*	*FWHM*	*Matched*
1	29.28	3.0480	29.83	0.2000	
2	32.01	2.7940	229.34	0.2400	
3	32.53	2.7504	98.73	0.2800	A
4	34.85	2.5726	238.79	0.3600	
5	35.55	2.5231	1000.00	0.3200	A
6	38.73	2.3233	905.54	0.3600	A
7	43.84	2.0633	58.34	0.3200	
8	46.27	1.9605	20.54	0.2000	A
9	48.84	1.8634	220.22	0.4000	A
10	52.20	1.7508	24.48	0.2400	
11	53.41	1.7141	50.37	0.3200	A
12	55.03	1.6674	35.48	0.2400	
13	58.28	1.5820	95.47	0.4800	A
14	59.24	1.5586	32.11	0.2400	
15	60.73	1.5238	28.64	0.4000	
16	61.53	1.5059	134.67	0.3200	A
17	66.27	1.4092	110.64	0.5600	A
18	68.13	1.3752	115.07	0.4800	A
19	72.40	1.3043	40.15	0.4400	A
20	75.08	1.2642	54.52	0.4400	A

Rietveld Refinement using FullProf

Calculation was not run or did not converge.

Crystallite Size Estimation using Scherrer Formula

Calculation was not run.

Degree of crystallinity analysis

Figure: XRD information of synthesized CuO-500 NPs with 95.1% matching with ICDD Card No. 00-005-0661 (Part V).

Profile area	*Counts*	*Amount*
Total area	6915964	100.00%
Diffraction peaks	1138797	16.47%
Background	5777167	83.53%
Instrumental background	892103	12.90%
Amorphous phases	4885064	70.63%

Degree of crystallinity (DOC) = 18.90%
Amorphous content (weight %) =81.10%

Integrated Profile Areas

Based on calculated profile

Profile area	*Counts*	*Amount*
Overall diffraction profile	6915964	100.00%
Background radiation	5777167	83.53%
Diffraction peaks	1138797	16.47%
Peak area belonging to selected phases	801339	11.59%
Peak area of phase A (Copper Oxide Tenorite, syn)	*801339*	*11.59%*
Unidentified peak area	337458	4.88%

Peak Residuals

Peak data	*Counts*	*Amount*
Overall peak intensity	21593	100.00%
Peak intensity belonging to selected phases	19956	92.42%
Unidentified peak intensity	1637	7.58%

Diffraction Pattern Graphics

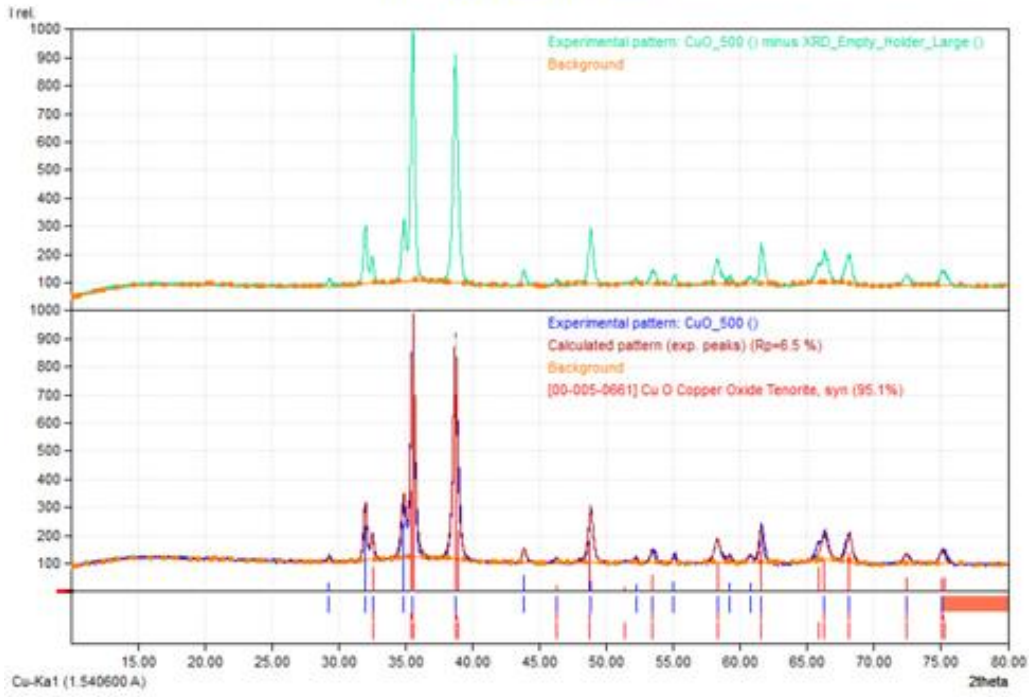

Figure: XRD information of synthesized CuO-500 NPs with 95.1% matching with ICDD Card No. 00-005-0661 (Part VI).